NUREG/CR-1179
UCRL-52733

# Application of the Coupled Fluid-Structure Code PELE-IC to Pressure-Suppression Analysis—Annual Report to NRC for 1979

W. H. McMaster, D. F. Quiñones, C. S. Landram,
D. M. Norris, Jr., E. Y. Gong, N. A. Macken, R. E. Nickell

Lawrence Livermore Laboratory

**Prepared for**
**U.S. Nuclear Regulatory**
**Commission**

NOTICE



This work was supported by the United States Nuclear Regulatory Commission under a Memorandum of Understanding with the United States Department of Energy.

Available from
GPO Sales Program
Division of Technical Information and Document Control
U.S. Nuclear Regulatory Commission
Washington, D.C. 20555

and

National Technical Information Service
Springfield, Virginia 22161

NUREG/CR-1179
UCRL-52733
R4

# Application of the Coupled Fluid-Structure Code PELE-IC to Pressure-Suppression Analysis—Annual Report to NRC for 1979

Manuscript Completed: November 1979
Date Published: May 1980

Prepared by
W. H. McMaster, D. F. Quiñones, C. S. Landram,
D. M. Norris, Jr., E. Y. Gong, N. A. Macken, R. E. Nickell

**Lawrence Livermore Laboratory**
**7000 East Avenue**
**Livermore, CA 94550**

**Prepared for**
**Nuclear Regulatory Division**
**of Reactor Safety Research**
**Washington, D.C. 20555**
**NRC FIN No. A-0116**

# APPLICATION OF THE COUPLED FLUID-STRUCTURE CODE PELE-IC TO PRESSURE-SUPPRESSION ANAYLSIS--ANNUAL REPORT TO NRC FOR 1979

## ABSTRACT

This report concludes a developmental effort to obtain a two-dimensional or axisymmetric computer code that calculates fluid-structure interaction problems in boiling-water-reactor (BWR) pressure-suppression systems. In this report several verification problems are concluded and applications to the Mark I and Mark II pressure-suppression systems are presented.

CONTENTS

Appendix F

## LIST OF ILLUSTRATIONS

## LIST OF TABLES

# FOREWORD

This work was supported by the United States Nuclear Regulatory Commission under a Memorandum of Understanding with the United States Department of Energy and is designated Task 189:A0116.

N. A. Macken, Department of Engineering, Swarthmore College and R. E. Nickell of Applied Science and Technology, La Jolla, Calif., were consultants on this project. D. M. Norris, Jr. is currently with the Electric Power Research Institute, Menlo Park, Calif.

The authors wish to acknowledge helpful discussions with G. L. Goudreau and R. L. Cudlin throughout the course of this work.

## LIST OF SYMBOLS

| | |
|---|---|
| $\vec{A}$ | generalized initial condition vector in shell algorithm |
| b | outer-fluid-boundary radius |
| c | sound speed |
| C | damping matrix |
| d | pipe diameter |
| D | tank diameter |
| $D_i$ | cell divergence |
| f | void fraction, natural frequency |
| g | gravitational constant |
| i,j | Eulerian cell row and column numbers |
| K | effective stiffness matrix |
| L | submerged vent pipe length |
| M | shell mass matrix |
| n | cycle number, vibrational mode number |
| p | ratio of fluid pressure to constant fluid density |
| P | pressure |
| $\vec{P}$ | effective load vector |
| $\underset{\sim}{q},\dot{\underset{\sim}{q}},\ddot{\underset{\sim}{q}}$ | generalized displacement, velocity, and acceleration |
| r | radial distance |
| R | cylindrical shell radius |
| t | time |
| T | temperature |
| $\tilde{u}$ | trial velocity |
| $u_i$ | cell velocity |
| $u_r$ | radial fluid velocity |
| $u_s$ | shell velocity on axis |
| $\alpha$ | advection constant in momentum equation |
| $\delta P_i$ | cell pressure increment |
| $\delta x,\delta y$ | cell sizes |
| $\delta t$ | time step size |
| $\varepsilon$ | divergence error units of $t^{-1}$ |
| $\rho$ | fluid density |
| $\nu$ | kinetic viscosity |
| $\omega$ | circular frequency |

## EXECUTIVE SUMMARY

A coupled fluid-structure computer program, PELE-IC, has been written at Lawrence Livermore Laboratory (LLL) to analyze boiling-water-reactor (BWR) pressure-suppression systems. The code has been thoroughly verified both against existing exact solutions as well as against experimental data. Applications have revealed development areas which must be pursued if PELE-IC is to be a sufficiently general code. In particular the following code efforts are recommended for future work: (1) coupling PELE-IC to the thermodynamics of the condensation events, and (2) including three-dimensional effects to accommodate multiple downcomers.

In November 1979, the PELE-IC code was released to the National Energy Software Center at Brookhaven National Laboratory, Upton, New York. A code release document* and PELE-IC user's manual† have been published.

This report presents additional PELE-IC verification and simulation problems that were not reported in our 1978 report. New code features have been added and are described in this report. We again present the PELE-IC code physics. The verification problem reported here is that of a vibrating submerged cylinder which tests fluid-structure coupling for curved shells. The PELE-IC code applications include simulations of the LLL 1/5-scale torus experiments, a harmonically-driven water-filled tank experiment, and the General Electric (GE4T) chugging experiments.

---

*E. Y. Gong, E. E. Alexander, W. M. McMaster, and D. F. Quiñones, PELE-IC Test Problems, Lawrence Livermore Laboratory, Livermore, Calif., UCRL 52835 (1979).

†W. H. McMaster and E. Y. Gong, User's Manual for PELE-IC: A Computer Code for Eulerian Hydrodynamics, Lawrence Livermore Laboratory, Livermore, Calif., UCRL-52609 (1979).

# 1.0 INTRODUCTION

The discharge of safety relief valves or a severe loss-of-coolant event in a boiling-water-cooled reactor steam-supply system triggers a complex pressure suppression system that is based upon sub-surface steam condensation in large pools of water. Figure 1 shows three typical geometries for pressure suppression designs--the Mark I, Mark II, and Mark III systems.[2] The Mark I is characterized by a partially water-filled toroidal shell. Steam is fed into the toroidal shell (wetwell) by a series of large vent pipes that connect the reactor cavity (drywell) to a manifold (or ring header) with pairs of pipes (downcomers) that extend below the water surface. Additional features of the Mark I and Mark II designs will be discussed later in the report.

From Fig. 1, we observe that the design of the Mark II system is considerably different from that of the Mark I because of its vertical downcomer vents and somewhat larger drywell volume. Here the vents extend downward from the bottom of the drywell into a wetwell cavity of rectangular torodial cross section. The Mark III system is characterized by horizontal vents and a much larger wetwell airspace than either the Mark I or Mark II system.

The physical problems associated with these designs fall into two categories. The first category is referred to as vent clearing, the process of expelling noncondensables from the system prior to steam flow. When these noncondensables--principally air--are expelled they create a subsurface bubble of substantial size which moves the water surface upward. The impact of this water surface on exposed structures, such as the ring header on the Mark I system, can produce consequential loading. The second category covers a variety of phenomena related to the transient overexpansion of a condensable volume and the subsequent inertially-driven volume decrease. Under some conditions the dynamics of the process are stable, and condensation oscillation results. Under other conditions, the dynamics are unstable, and chugging takes place. The dynamic loading of either event, depending upon fluid-structural design parameters, can be of concern in safety analysis. Further discussion of condensation events may be found in Appendix A.

This report is the second in a series[3] that describes the development of a method for calculating the loads and the structural response in pressure-suppression systems. The method is embedded in a computer code, called PELE-IC, that couples a two-dimensional Eulerian fluid algorithm to a finite element shell algorithm. The fluid physics equations are solved by use of the SOLA finite difference algorithm,[4] which uses a Newton Rhapson iteration technique to solve the Navier-Stokes and continuity equations. The iteration is continual until the continuity, fluid-structure interface compatibility, and free and rigid surface boundary conditions are satisfied. These fluid and fluid-structure algorithms have been extensively verified through calculations of known solutions from the classical literature, and by comparison to air- and steam-blowdown experiments. One verification example is based upon mechanically-driven fluid-structure vibration experiments.

The verification exercises indicated the need for a more rational methodology for supplying the loading functions that drive the vent clearing, condensation oscillation, and chugging processes. As a result, a vent flow model has been developed that couples the drywell pressure history to the pool by treating compressibility effects (e.g., choked flow) in noncondensable gases. This model has been used to improve the comparisons with air-blowdown experiments in both rigid and flexible water-filled containers. Similar development efforts have not been undertaken with repect to computing local pressure perturbations associated with stable and unstable condensation events. Instead, artificial pressure-time histories were prescribed to precleared* steam bubbles, with no attempt made to examine the heat transfer process at the bubble surface or the inertial overexpansion of the bubble into the water pool. A modification to this model, which takes compressibility of the steam column in the downcomer into account, reproduced the same structural frequencies observed in steam-blowdown experiments.†

Early in the fiscal year, two-and-a-half and three-dimensional extensions of the PELE-IC code were studied. We considered rather modest code extensions, such as a generalized circumferential harmonic dependence, as well as

---

*The pressure is applied to a portion of the surface of the water--that portion coincident with the exit plane of the downcomer.

†Experimental chugging results are proprietary information and are not presented in this report.

significant development efforts, such as a three-dimensional finite element fluid and shell modeling code patterned after the LLL NIKE-3D[5] package. Since the manpower estimates for the various options ranged from a low of one man-year to a high of four man-years, it was decided that an attempt should be made to explore the limitations of the existing two-dimensional code, as applied to three-dimensional problems, before recommending further development.

The vehicle chosen for these applications was the Mark I LLL one-fifth-scale PSE geometery and experimental results.[6] The object of the study, in addition to two-dimensional simulation of three-dimensional events, was to investigate the sensitivity of response measurements, such as vent-clearing time and peak-bottom pressure, to variations in downcomer submergence, drywell pressurization rate, torus pool level, downcomer fill level, and initial wetwell pressure. Selected downcomer pressure-time histories were used. The results of this study are discussed in detail in Sec. 5.

The major finding relative to two-dimensional simulation of three-dimensional events was that, up to the time of vent clearing, an axisymmetric model provides a good estimate of bottom center-pressure history. This is, early time axisymmetric calculations model three-dimensional vent exit pressure relief as water emerges from the end of the downcomer (a plane-strain model would tend to overpredict the bottom center-pressure because the fluid particles are constrained to move in the plane).

In the sections that follow, the general development of the PELE-IC code is described. Then, the verification exercises are discussed in such a way that the strengths and shortcomings of the code are demonstrated. Finally, we present a set of problems applicable to present-day safety issues with respect to existing or planned BWR pressure-suppression systems.

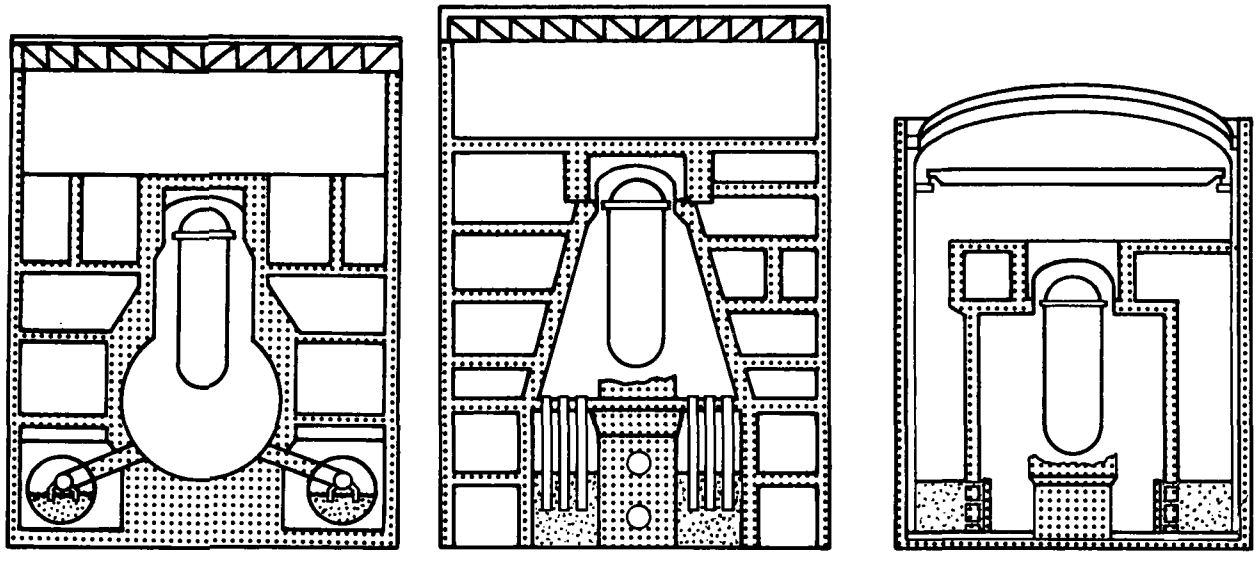


FIG. 1. Three types of BWR pressure-suppression containment.[2]

# 2.0 DESCRIPTION OF THE PELE-IC COMPUTER CODE

## 2.1 INTRODUCTION

The PELE-IC code couples a two-dimensional, semi-implicity, Eulerian fluid-dynamics (SOLA) algorithm to a Lagrangian finite element shell algorithm for the analysis of fluid-structure interactions. The PELE-IC code is quasi-two phase since we can couple to either a one-dimensional or a lumped parameter description of compressible gases. The code is written in both plane and cylindrical coordinates in order to handle a variety of geometrical configurations and is capable of following large interface motions through the calculational grid. By the use of a variable time step we are able to accommodate varying flow conditions and maintain computational stability.

The basic semi-implicit solution algorithm contained in the SOLA code[3] was used as a foundation for the development of the PELE-IC code. We track the movement of free surfaces using a full donor cell treatment based on a combination of void fractions and interface orientation. This gives us great versatility in following fluid-gas interfaces for bubble definition and water surface motion without the use of marker particles.

The structural motion is computed by a finite element code[7] from the applied fluid pressure at the fluid structure interface. The finite element shell structure algorithm used conventional thin-shell theory with transverse shear. The spacial discretization employs piecewise-linear interpolation functions and one-point quadrature applied to conical frustra. We use the Newark implicit time integration method implemented as a one step module. The fluid code then used the structure's resultant position and velocity as boundary conditions. The fluid pressure field and the structure's response are corrected iteratively until the normal velocities of the fluid and structure are equal. This results in a strong coupling between the two algorithms.

## 2.2 GENERAL DESCRIPTION OF THE SOLUTION ALGORITHMS

The underlying approach used by PELE-IC for the solution of general flow fields is the use of the semi-implicit SOLA algorithm. The basic assumption

of this approach is that all flow variables within the computational grid satisfy the continuity equation for each cell, regardless of whether or not the computational cell contains a free surface or a moving structure. For imcompressible fluids this means that all cells are divergence free. (The code also has a compressible fluid option based upon the acoustic wave equation.) This assumption permits freedom of motion for all surfaces throughout the grid. Superimposed on this basic algorithm we have applied the boundary conditions for free surfaces, compressible gases, and moving structures.

In this section we give a brief description of the solution algorithms. A more detailed coverage is given by McMaster, et al.[3,8]

## 2.3 SOLA SOLUTION ALGORITHM

The SOLA algorithm uses a Newton-Raphson iteration on the pressure field to solve the mass conservation equation. At each iterative step the pressure in each fluid cell is adjusted to satisfy the divergence criteria. In this algorithm the pressure is a cell centered varible and the velocity components are specified on cell sides.

The algorithm is solved by first writing the conservative form of the Navier-Stokes equation for the fluid velocity ($\underset{\sim}{u}$) in terms of time level:

$$\partial \underset{\sim}{u}/\partial t = (-\nabla * \underset{\sim}{uu} + g\ \nu\nabla^2 \underset{\sim}{u})^n - \nabla p^{n+1} \quad ,$$

where the superscript n indicates the time level and $p = P/\rho$ is the ratio of the pressure to the density of the fluid. The body acceleration is given by g and the kinematic viscosity is specified by the constant $\nu$.

Setting

$$p^{n+1} = p^n + \delta p$$

gives

$$\underset{\sim}{u}^{n+1} = \left[\underset{\sim}{u} + \delta t(-\nabla * \underset{\sim}{uu} - \nabla p + g + \nu\nabla^2 \underset{\sim}{u})\right]^n + \delta t(\delta \nabla p) \quad .$$

If we define the term inside the brackets as $\tilde{u}$, then the equation to be solved is

$$\underset{\sim}{u}^{n+1} = \tilde{u} + \delta t(\delta \nabla p) \quad ,$$

where $\tilde{u}$ is found using the finite difference formulation of Hirt, et al.[4] This equation is solved iteratively where we define the divergence error ($D_i$) for each cell at the $i$th iteration as

$$\nabla^* \underset{\sim}{u}_i = D_i \quad ,$$

and $\tilde{u}$ is used as the first trial velocity to start the iteration process. The pressure increment necessary to update the velocity field is given by

$$\delta p_i = \frac{-(1 + \phi) D_{i-1}}{\partial D / \partial p} \quad ,$$

where $\phi$ is a correction term ($0 < \phi < 1$) dependent upon adjacent cells in the direction of the sweep through the grid, and $\partial D/\partial p$ is a constant dependent only upon the cell size, the time step, and the presence of a structural boundary. We update the velocity field in each cell with the pressure increment, using

$$\delta u_{zi} = \pm \delta p_i \delta t / \delta z \quad ,$$

where $\delta z$ is the cell side in the direction of the velocity component ($u_z$), and the sign is chosen dependent upon which side centered velocity component is being adjusted. Satisfaction of the continuity equation in any particular cell perturbs the velocity field of its neighbors. Hence the method is applied in sweeps throughout the grid until the divergence error satisfies

$$\nabla^* \underset{\sim}{u}_i = D_i \leq \varepsilon$$

where $\varepsilon$ is a preset convergence tolerance which should be set according to the minimum flow field of interest expected in the solution. The final velocity and pressure field are then

$$\underset{\sim}{u}^{n+1} = \tilde{u} + \sum_i \delta u_i \qquad \text{and} \qquad p^{n+1} = p^n + \sum_i \delta P_i \quad .$$

Since the solution procedure is a Newton Raphson iteration, the rate of convergence is dependent upon the magnitude of $\partial D/\partial p$ which has the form

$$\frac{\partial D}{\partial p} = 2\delta t \left[ \frac{F_x}{\delta x^2} + \frac{F_y}{\delta y^2} \right] ,$$

where $F_x$ and $F_y$ are dependent upon structural interfaces coupled to the fluid cell. If there is no structure, then $F_x = F_y = 1$. From the formula for $\delta D/\delta p$ we see that convergence is accelerated by the use of large time steps and small cell sizes. However, the user is limited in his choice by the physics of the problem. In general, we require that

$$\frac{u_z \delta t}{\delta z} < 0.4 ,$$

where $\delta z$ is the component $\delta x$ or $\delta y$ in the direction of the maximum velocity $u_z$.

### 2.3.1 Thin Shell Algorithm

The finite element module used simple shell theory with transverse shear (see Kraus[9]). The element formulation was described by Hughes and Taylor[10] for beams and plates and was extended to axisymmetric and plane shells by Goudreau.[11] (Similar results were obtained by Zienkiewicz, et al.[12] at about the same time.) The element is a two-node, conical frustrum with three degrees of freedom per node. Shape functions are piecewise-linear for displacements and rotations. The shear locking associated with low-order interpolation functions is removed by one-point quadrature. Large deformation (here two to three shell thicknesses) is accounted for in an approximate way by reformulating the stiffness matrix at every time step. By the use of Lagrangian equations, it may be shown that the behavior of the structure is described by

$$\underset{\sim}{M}\ddot{\underset{\sim}{q}} + \underset{\sim}{C}\dot{\underset{\sim}{q}} + \underset{\sim}{K}\underset{\sim}{q} = \underset{\sim}{P}(t),$$

where M is the mass matrix, $\ddot{\underset{\sim}{q}}$ is the vector of generalized acceleration, C is the damping matrix, $\dot{\underset{\sim}{q}}$ is the vector of generalized velocity, K is the stiffness matrix, $\underset{\sim}{q}$ is the vector of generalized displacement, and $\underset{\sim}{P}$ is the fluid and other loads on the structure.

The Newmark implicit time integration scheme (see Goudreau and Taylor[11]) is used at each time step to move the shell. The algorithm has the form

$$(K + 4M/(\delta t)^2)\underset{\sim}{q}^{n+1} = \underset{\sim}{p}^{n+1} - 4M\,\underset{\sim}{A}^{n}/(\delta t)^2 \quad ,$$

where

$$\underset{\sim}{A}^{n} \equiv \underset{\sim}{q}^{n} + \dot{\underset{\sim}{q}}^{n}\delta t + \ddot{\underset{\sim}{q}}^{n}(\delta t)^2/4 \quad .$$

Goudreau[2] gives the derivation of effective stiffness matrix K and a FORTRAN listing of the one-step module.

The thin-shell algorithm has been made more general by the addition of the following four features:

1. Each element may have its own thickness.

2. Each node can be specified to have its own separate restraints and prescribed initial displacement.

3. The code computes the static deflection of the structure as a result of the initial loading before beginning the dynamic solution.

4. The gas pressure in the ullage region as well as all fluid pressures are applied to the shell.

### 2.3.2 Fluid-Structure Interface Algorithm

This algorithm couples the fluid's motion to the structure's motion within the SOLA iteration loop. Normal velocity compatibility between the structure and fluid is required where the Lagrangian shell crosses either the I-line or J-line intercept which defines the centroid of the Eulerian cell. The choice depends on the angular orientation of the structure. The finite element module used the pressure field supplied by the fluid and provides the fluid code with the resultant position and velocity of the interface. Each change in the pressure field causes a different structural response, and each different response changes the flow field of the fluid. Therefore, the iteration proceeds until both conditions are satisfied. Within a single

iteration, all Eulerian fluid zones are adjusted one by one, using the latest values available, and then all the Lagrangian shell nodes are simultaneously adjusted by the implicit time-step solution.

The pressure applied to an element is determined by an interpolation along each intersecting I or J line to the neighboring full fluid cell. These interpolated values are weighted by the liquid content of the cell so that the proper pressure is applied when a free surface is in the same cell. The interpolation procedure provides a smooth pressure history whenever the structure crosses a grid line.

The solution strategy is to first set the normal fluid velocity equal to the normal structure velocity at the coupling point. The structure's normal velocity is found by an interpolation between nodal values and the intercept angle. The normal fluid velocity is found by an interpolation between all four of the cell side velocities. This determines the cell side velocity which is coupled to the structure. This first step of setting the coupled Eulerian cell velocity to satisfy the boundary conditions imposed by the structure causes the cell not to satisfy the divergence criteria; therefore, the second step is to adjust the cell pressure using the SOLA algorithm so that the cell is divergence free. This two-step process is repeated each iteration.

The coupled velocity is chosen to be on the cell side nearest the structure. In this way no discontinuities arise when the structure crosses a grid line.

### 2.3.3 The Free Surface Algorithm

Accurate free surface tracking is necessary to allow the application of velocity and pressure boundary conditions at fluid-gas interfaces. We track the free surface by a combination of void fraction and surface orientation in each cell. The void fraction provides for the conservation of mass and the surface orientation allows us to apply the proper boundary conditions and follow the flow from cell-to-cell.

The free surface algorithm performs four functions:

1. Determines the surface orientation within the calculational cell based upon its fluid content and that of neighboring cells. This orientation is specified by its intercepts on two sides of the cell. Within the cell, the

interface is considered to be a straight line segment. Thus, the surface is tracked by its intersection of grid lines.

2. Applies to the prescribed boundary pressure to the fluid surface. This is done by finding the appropriate cell centered pressure by an interpolation from the nearest fluid cell to the boundary pressure. Recent additions to the code also allow the application of a prescribed velocity boundary condition in lieu of a prescribed boundary pressure to the fluid surface. This option allows one to drive the surface with a moving piston. Both these options allow the boundary conditions to be a function of time.

3. Calculates the fluid advection based on surface orientation using the donor cell method where the amount of liquid advected is determined from the contents of the upstream cell, the orientation of the surface, and the velocity of the common liquid side. This method guarantees the conservation of mass during advection.

4. Uses velocity boundary conditions for the void sides of the cell to maintain continuity of the flow field. This assures the continuity of flow when a surface crosses grid lines.

## 2.4 SPECIAL FEATURES

### 2.4.1 Downcomer Pipes

Downcomer pipes are modeled by specifying the bounding grid lines as rigid. A special differencing algorithm has been added to the code to allow this option. In this manner, pipe wall thicknesses, small in comparison with a calculational cell, can be correctly modeled. For vent clearing problems, the specified driving pressure is applied as a boundary condition between the grid lines defining the pipe. The code has the capability of handling up to two rigid downcomer pipes in this manner.

### 2.4.2 Obstacles and Baffles

Obstacles and baffles which restrict the flow can be modeled by specifying portions of grid lines as rigid boundaries. The code will then apply the boundary condition of zero normal velocity at this boundary. The number of such obstacles that can be specified is unrestricted.

### 2.4.3 Coupling to Compressible Gas Flow

In many applications the downcomer is driven from a drywell with either variable or constant pressure. Sometimes this flow is further controlled by the use of an orifice. To provide for these situations a flow model coupled to the fluid dynamics was developed (see Appendix B). This model couples the adiabatic bubble pressure to the drywell and current bubble volume by the equation

$$P(t) = P_{u_i} \left(\frac{V_o}{V(t)}\right)^{\gamma} \left[1 + \frac{\gamma}{\rho_{u_i} V_o^{\gamma}} \int_0^t \dot{m}\, V^{\gamma-1}\, d\tau\right] ,$$

where

$\dot{m}$ = Mass flow rate through the orifice as specified in Vennard[13] (The formula used depends upon whether the flow is choked or unchoked.),

$V_o$ = Original downcomer volume from the orifice to the water level,

$V$ = Current volume including the bubble,

$P_{u_i}$ = Initial ullage pressure corresponding to density $\rho_{u_i}$.

The time of integration, t, covers vent clearing and subsequent adiabatic bubble formation and growth.

In application, we find that the mass flow is frequently initially choked and dependent upon only upon the drywell pressure and density. Subsequently, during vent clearing, the flow becomes unchoked and is dependent upon both the drywell pressure and the bubble pressure. Since the bubble pressure is dependent upon the bubble growth in the pool, there is a coupling between the suppression pool and the drywell.

### 2.4.4 Acoustic Pipe Boundary Conditions

During the steam flow phase through a downcomer, the steam vapor condenses and gives rise to the phenomenon called chugging. These chugs at the end of a downcomer pipe give rise to reflected pressure pulses characteristic of the

organ pipe frequencies of the downcomer. We have written a simple one-dimensional acoustic model code to calculate these pulses. These reflected pulses provide the driving source to investigate the chugging problem in the PELE-IC code (see Appendix C).

### 2.4.5 Variable Ullage Pressure

During a vent-clearing event the bubble growth causes a pool swelling in the confined ullage region. This compressed air region then provides an upload on the confining structure. We derive this pressure pulse from the perfect gas law using the ullage volume change as calculated from the rise of the water surface. In the MIT experimental configuration this ullage pressure is also applied to the bottom flexible plate. The code has been modified to simulate these experiments.

### 2.4.6 Collapsing Bubbles

In chugging studies of collapsing adiabatic bubbles (e.g. the G.E. belljar calculations) we apply a boundary pressure derived from the perfect gas law dependent upon the current bubble volume and the vapor pressure of the water. The use of the void fraction technique allows us to monitor the corresponding bubble volume accurately.

### 2.4.7 Frequency Analysis

We are interested in a frequency analysis of the resultant flexible structure vibrations when loaded by a vent clearing pulse or chugging pulses. To do this we have written a Fourier transform code using the method of Goertzel.[14] This code accepts the output fluid pressure or structure displacement time histories from the PELE-IC code and provides the frequency content (see Appendix D).

# 3.0 VERIFICATION OF COUPLING ALGORITHM FOR CURVED SURFACE: THE SUBMERGED CYLINDER

## 3.1 INTRODUCTION

Several previous verification problems have been calculated to test individual physical representations which PELE-IC must accommodate for general fluid-structure phenomenology.[3] These have included draining tanks, submerged disks, and spherically growing bubbles in an unconfined liquid. These respective problems, each having an exact solution, were chosen to verify the wetwell fluid dynamics, fluid-structure coupling for a simple surface, and void-liquid interface dynamics. Additionally, separate calculations were performed to check the accuracy of the finite element shell code alone. In these calculations (not reported here) the static deflection of various shell geometries (under various boundary supports for prescribed uniform static pressure loads) compare to theoretical solutions within 0.23%.

Previous cases[3] for verifying the fluid-structure coupling algorithm considered only flat structural surfaces adjacent to fluid flow fields. The following work verifies the PELE-IC coupling algorithm for a curved structural shell neighboring the flow field.

Figure 2a shows the indefinitely long (plane strain), thin, cylindrical steel sheel (r = R) encompassed on its outer surface by an annulus of liquid whose outer boundary (r = b) is a free surface (zero pressure). All gravitational and fluid viscous forces are ignored. Only the inextensible elliptical bending mode for the shell is considered (i.e., n = 2, see Appendix E). Only incompressible flow within the liquid annulus is permitted; that is, the fluid sound speed is taken to be infinite. Accommodation of fluid compressibility is not warranted for our purposes of verifying fluid-structure coupling for a curved surface.

Love[15] has presented the natural frequency solution for the structure alone in absence of the fluid, and Schroeder and Markus[16] and Nickell and Dunham[17] for the case of a compressible fluid surrounding the shell. References 16 and 17 give some numerical eigenvalue results for the implicit, exact solution to the compressible flow problem for various vibrational modes. The governing derivations are presented in Appendix E and are

specialized to the applicable incompressible solutions for natural frequencies as well as corresponding flow field, these having explicit solutions in the incompressible limit, $\omega_n \frac{b}{c} \to 0$, where $\omega_n$ is the circular frequency for the nth for the nth mode and c is the sound speed in the fluid.

## 3.2 MODEL

The system whose dimensions (shown in Fig. 2a) were chosen to conform to previous calculations (Refs. 14 and 15), was excited by the used of nodal forces applied to the shell to push inward at the minor axis and pull outward at the major axis.* These forces were chosen to be equal and temporally ramped for the first 2 ms of the transient after which they were released.

The $90^{\circ}$ segment formed by the intersection of the elliptical axes was composed of an 80 × 80 Eulerian fluid mesh and 8-shell finite elements (see Figs. 2a and 2b).

The 1.07-cm fluid grid size was chosen small enough to resolve the steep fluid velocity gradient near the shell surface. The 2-ms time step was chosen large enough to progress in reasonable computation times, yet small enough to resolve the period sought (27-28 ms). Preliminary calculations using a coarse fluid grid (4.29 cm), four times the dimension ultimately used (1.07 cm), with a small time step (0.2 ms) proved unsuccessful in spatially resolving the unsteady flow field near the shell surface. Care was taken to choose the nine shell nodal points so that sufficient J or I line fluid-to-structure coupling occurred (Fig. 2b). Also, geometric symmetry in shell nodal point placement was enforced (used as a test condition for the results) about the $45^{\circ}$ line dissecting the elliptical axes. Along this line the fluid motion must contain no radial components (not enforced), and at the intersection of the $45^{\circ}$ line with the shell, the shell must not be displaced (not enforced). A typical calculation using a 2-ms time step and $\varepsilon = 10^{-3}$ $ms^{-1}$ required 10.7 min of CDC 7600 CPU time to run to 70 ms.

The magnitude of the two nodal forcing functions was chosen to provide a maximum shell deflection of about 0.085 cm or 13% of the shell thickness. The

*In the n = 2 mode, the cylindrical shell is perturbed into an elliptical bending mode.

shell deflection owing to the two localized forces was found to be very nearly elliptical. The maximum fluid velocities occur at the elliptical axes of the shell where the shell and fluid velocities are identical and are about 0.085 cm/ms. For these maximum conditions, and for the aforementioned grid size and time step used, the advection parameter $\alpha = u_{max}(\Delta t/\Delta x) \simeq 0.16$. The magnitude of $\alpha$ emphasized the unstable center-spaced advection differencing ($\alpha \to 0$) rather than the stable donor cell differencing ($\alpha \to 1$). Consequently, our weighted advection differencing scheme[3] was updated in each time step by use of variable $\alpha$ computed from the flow field. Additionally, to assist in stabilizing the numerics a viscosity was prescribed but was small (0.001-to-0.0001 $cm^2/ms$ compared to the maximum allowable value, $(\Delta x)^2/(4\Delta t) = 0.14$ $cm^2/ms$ above which vorticity would diffuse between fluid cells.[18] Systematic changes in viscosity were not found to affect the computed flow field.

The flow field computations converge when the velocity $\vec{u}$ is such that the divergence constraint is tolerable; i.e., $|\text{div } \vec{u}| < \varepsilon$. In these calculations a value of $\varepsilon = 10^3$ $ms^{-1}$ was first used to obtain a solution; however, owing to the difficulty in resolving the very small velocities as the free surface was approached ($r = b$), this value of $\varepsilon$ was found to be too large. Consequently, a value of $\varepsilon = 10^{-4}$ $ms^{-1}$ proved to be satisfactory in computing the total flow field. It is this smaller value of $\varepsilon$ on which the results presented here were computed. At $\varepsilon = 10^{-4}$ $ms^{-1}$, the error in computed fluid pressure was about 0.3% near the shell surface where the velocities are large. The error in computed fluid pressure was found to be about 4% half-way through the liquid annulus (where the velocities are much less than near the shell surface) and about 9% at the free surface (where the velocities are two orders of magnitude less than at the shell surface). For the grid size used (80 × 80 Eulerian mesh), the computational time became very large for $\varepsilon$ smaller than $10^{-4}$ ($ms^{-1}$). We noted, however, that the shell response, and, therefore, the natural frequency sought, was insensitive to $\varepsilon$ for all $\varepsilon < 10^{-4}$ $ms^{-1}$. This conclusion agrees with physical reasoning that errors in the near quiescent velocity field far from the shell are unimportant with respect to the shell response.

## 3.3 COMPARISON WITH EXACT SOLUTION

A computed, two-dimensional flow field, which reverses direction in each oscillatory cycle of the shell, is shown in Fig. 3. In Fig. 4 the computed, normalized radial fluid velocity distributions along the elliptical axes are compared to the exact profile, derived in Appendix E

$$\frac{u}{u_s}(r) = \frac{r}{R} \frac{\left\{1 + \frac{1}{2}\left[\left(\frac{b}{r}\right)^4 - 1\right]\right\}}{\left\{1 + \frac{1}{2}\left[\left(\frac{b}{R}\right)^4 - 1\right]\right\}}, \quad n = 2, \quad 1 \leq \frac{r}{R} \leq \frac{b}{R},$$

where $u_s$ is the shell velocity at either axis. The computed velocity distributions approach the exact, quasi-steady distribution long after the initial excitation ends. Figure 5 shows that the amplitude of the computed, nodal-shell response at either elliptical axis likewise also approaches an asymptotic limit long after the initial excitation ends. These coincident results are a consequence of the adjustment of the potential energy of the shell and the kinetic energy of the liquid-to-portioned energy exchanges associated with periodic motion of the two. Because of the excitation used, a greater portion of the total energy is given initially to the shell than to the fluid. Consequently, the shell amplitude asymptotically decays through readjustments in the shell potential energy and through the supply of kinetic energy to the massive quantity of liquid (see Fig. 4).

The natural frequency f for the system vibrating in the inextensible elliptical bending mode (n = 2) with the fluid assumed incompressible is derived in Appendix E and is given by

$$\frac{f}{f_o} = \left\{1 + \frac{\frac{1}{5}}{\frac{h}{R}\frac{\rho_s}{\rho_o}\left[\frac{1}{2} + \frac{1}{\left(\frac{b}{r}\right)^4 - 1}\right]}\right\}^{-1/2},$$

where $f_o$ is the n = 2 frequency (Hz) for the structure in absence of the fluid:

$$f_o = \frac{1}{2\pi}\left[\frac{3}{5}\ \frac{E\,h^2}{\rho_s R^4 (1-\nu)^2}\right]^{1/2},$$

where

$E$ = Young's modulus of elasticity ($2.0685 \times 10^6$ bars),

$\rho_s$ = shell density (7.803 gm/cm$^3$),

$R$ = shell radius (25.72 cm),

$\nu$ = Poisson's ratio (0.3),

$h$ = shell thickness (0.635 cm),

$b$ = free surface radius (82.8 cm).

For a fluid density of $\rho_o$ = 1 g/cm$^3$, the following result from the exact solution:

$$f_o = 63.9 \text{ Hz}$$

$$f = \begin{cases} 36.6 \text{ Hz for } b = 82.8 \text{ cm} \\ 36.4 \text{ Hz for } b \to \infty \end{cases}$$

Because the shell thickness (h) is small compared to the shell radius (R), the analysis presented in Appendix E does not distinguish between the mean radius of the shell, upon which the shell equilibrium equations are written, and the outer surface of the shell, to which the fluid motion equations are coupled. If the difference between mean and outer radius is accommodated in the analysis, the above frequency for b = 82.8 cm decreases from 36.6 Hz to 36.3 Hz and the corresponding periods are 27.3 ms and 27.6 ms, respectively. Either of these values compares favorably with the 27-ms PELE-IC computed period for the cycle demonstrated in Fig. 5.

The submerged cylinder's n = 2 wavelength of 1300 cm (assuming the fluid in water) is an order of magnitude larger than the outer-fluid-boundary radius (b = 82.8 cm). Consequently, the incompressible assumption for the fluid is justifiable. It was also necessary to justify the omission of the advection

term within the momentum equations on the computed PELE-IC frequency since these terms were also omitted in the exact solution given in Appendix E. PELE-IC was run with and without advection present and no discernable frequency shift was noted (see Fig. 5).

## 3.4 CONCLUSIONS

The advantage of treating the fluid in an Eulerian coordinate system is shown by our success in accommodating large relative tangential motions between shell and fluid. (In the n = 2 mode the two tangential motions are always opposed.) Such cases have escaped previous solution because of numerical problems encountered when the finite-element method is applied to the relatively large tangential motion between fluid and structure. These problems are discussed in a survey paper by Nickell and Carey.[19]

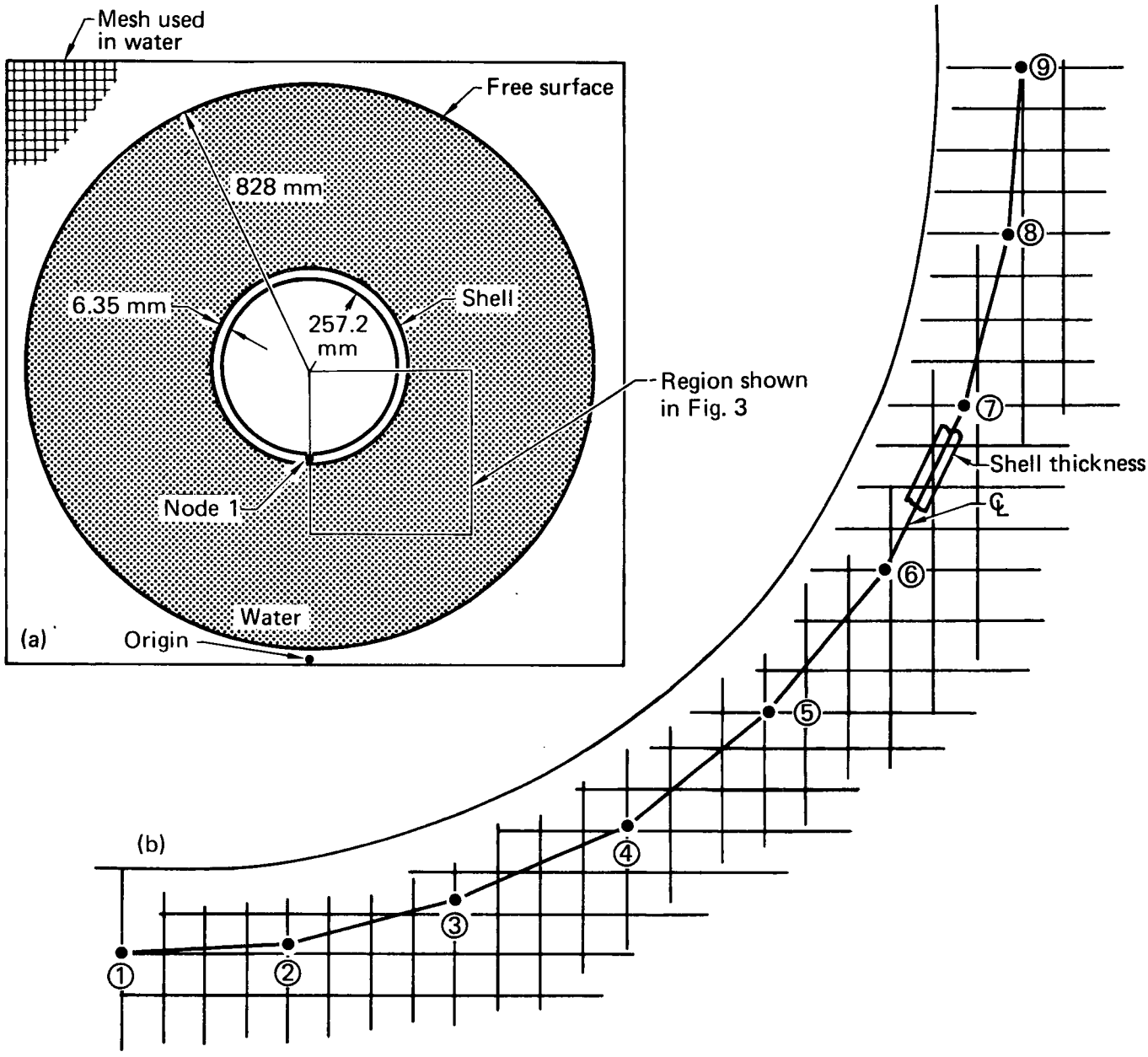


FIG. 2. (a) Geometry and dimensions used when modeling a submerged cylindrical shell. (b) Shell elements used and their relationship to the Eulerian fluid grid selected.

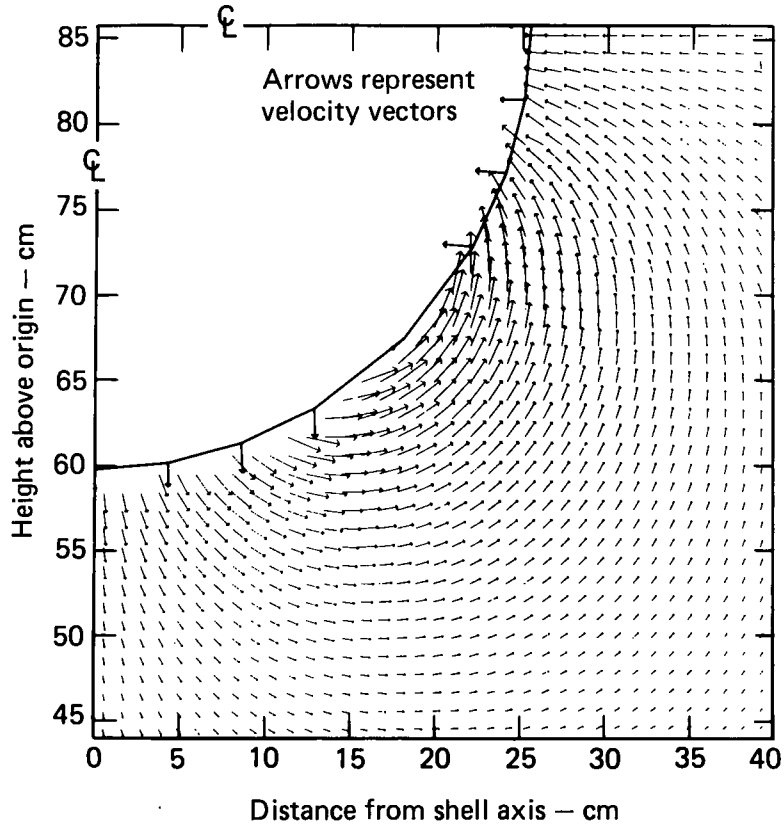


FIG. 3. Computed flow field (blowup of square region shown in Fig. 2a) for a submerged cylindrical shell 20 ms after excitation.

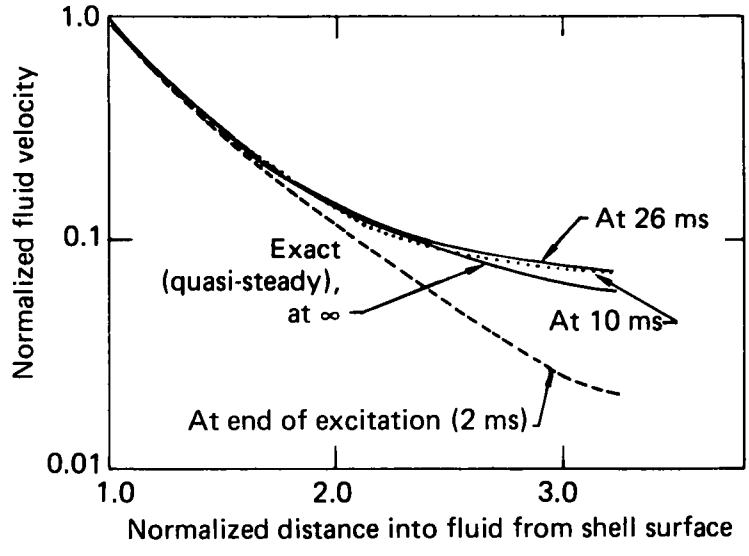


FIG. 4. Normalized fluid velocity distributions along the elliptical axes for a submerged cylindrical shell. The exact (infinitely late) distribution is compared to those computed for three different times after excitation.

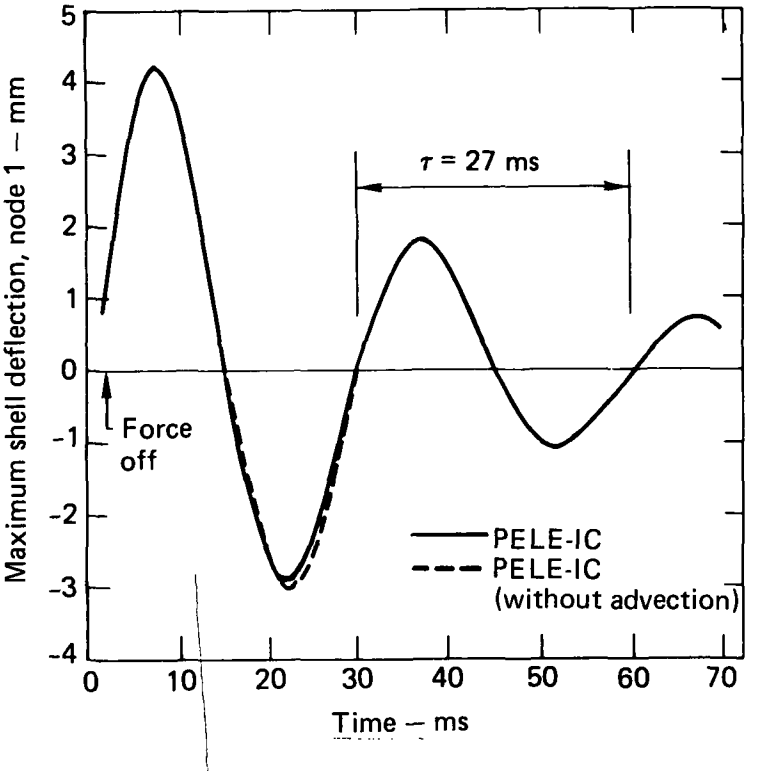


FIG. 5. Calculated maximum shell deflection at Node 1 (See Fig. 2a) at either (perturbed) elliptical axis as a function of time.

## 4.0 COMPARISON WITH LABORATORY AIR-BLOWDOWN EXPERIMENTS CONDUCTED AT MIT

These experiments by Javadi and Huber[20] use a rigid, cylindrical tank (see Fig. 6) with a central downcomer whose exit is submerged below the water surface. A fast-opening valve releases (from a pressurized drywell) air that flows through an orifice and down the pipe into the water. The flow is initially choked by the orifice, but the dynamic pressure rises in a few milliseconds to that of the drywell. This pressure is applied to the water surface and pushes the water out of the pipe in about 20 ms. The peak dynamic pressure occurs at the center of the bottom plate shortly after this time. The drywell pressure in the downcomer at vent clearing time is suddenly reduced by the growing bubble. As the bubble expands toward the water surface the pressure rises again to that of the drywell.

Tests were made with rigid and flexible bottom plates. Pressure was recorded in the downcomer (see gage A in Fig. 6), in the wetwell air space above the water surface, and in the water. The air in the wetwell was pressurized to 5.7 kPa (absolute) initially, and the pressure was balanced on the flexible bottom plate so that it registered only the weight of the water. The drywell pressure was 17.1 kPa. The water was cooled to just above freezing to lower the vapor pressure, and a surfactant was added to remove trapped air bubbles.

We found that computer simulations using the experimental downcomer pressure trace predicted smaller bubble volumes than those given by Javadi and Huber. Hence, we replaced this pressure forcing-function with a computer model of the orifice flow (see Appendix B). This flow calculation couples the bubble volume pressure to the drywell by the equation

$$P = P_{u_i}\left(\frac{V_o}{V(t)}\right)^{\gamma}\left[1 + \frac{\gamma}{\rho_{u_i} V_o^{\gamma}}\int_0^t \dot{m}\, V^{\gamma-1}\, d\tau\right], \qquad (1)$$

where the symbols are defined in Appendix B. The flow rate ($\dot{m}$) through the orifice is specified in Vennard.[21]

The differences between the measured downcomer pressures and the pressure predictions of the revised computer model are shown in Fig. 7. The calculation reveals a strong coupling between the start of bubble growth and the driving pressure decay. Incompatibilities in prescribed bubble pressure, however, introduce instabilities in the calculation.

Results for the rigid-bottom calculation are given in Fig. 8. Calculated pressures at three different locations are compared with the Javadi and Huber data from the pressure transducer. These calculated traces are almost identical except for the vertical shift caused by the static head. In Figs. 8 through 11 we have enforced agreement in measured and calculated vent clearing times. Calculated bubble growth is shown in Fig. 9. Figure 10 compares the computed increase of ullage pressure from pool swell with the Javadi and Huber data. The good agreement in wetwell pressure confirms accuracy of the calculated bubble volume.

A second calculation, using a flexible, 1-mm-thick aluminum bottom plate (Fig. 11), reveals the strong effect of the fluid-structure interaction. The computed pressure at three different locations in the water varies considerably in contrast to that of the rigid base plate. The measured pressure, also plotted on this figure, agrees well both in amplitude and frequency with the calculations. The spatial dependence of pressure appears again in the pressure contours of Fig. 12. The peak response shows a dynamic amplification of 68% above the drywell pressure. Hence, both calculations and experiments imply that the phasing of the structural response and the driving pressure can cause large dynamic amplifications.

Calculated bottom plate displacement as a function of time is shown in Fig. 13. We predict a peak displacement of 0.75 mm for the 1-mm-thick plate. This is large compared to the plate thickness and results in substantial deviations from the linear theory which excludes the effects of membrane stresses (e.g., Timoshenko and Woinowsky-Krieger[22]). The natural frequency is increased by the plate membrane stresses but decreased by the fluid-structure interactions. We calculated a peak strain of 364 microstrain, compared with 300 microstrain obtained by Javadi and Huber.

We have given considerable attention to the differences in vent clearing times between the calculations and the experiments. It may be shown (see Kang[23]) that for a constant pressure differential ($\Delta P$) the vent clearing

time is given by

$$t \approx L\sqrt{\frac{\pi}{2}\frac{\rho}{\Delta P}}\,, \tag{2}$$

where L is the submerged vent length and $\rho$ is fluid density.

If we assume a constant backpressure that is equal to the wetwell pressure plus the static head at the end of the downcomer, Eq. (2) gives the vent clearing time at 19.4 ms. Javadi and Huber give 21 ms, whereas we calculate about 24 ms. The PELE-IC calculation shows that considerable dynamic backpressure develops at the bottom of the vent. The backpressure is ignored in Eq. (2), which therefore becomes a lower bound to the actual vent clearing time. We therefore conclude that the empirical origin for time differs from that used in our calculations.

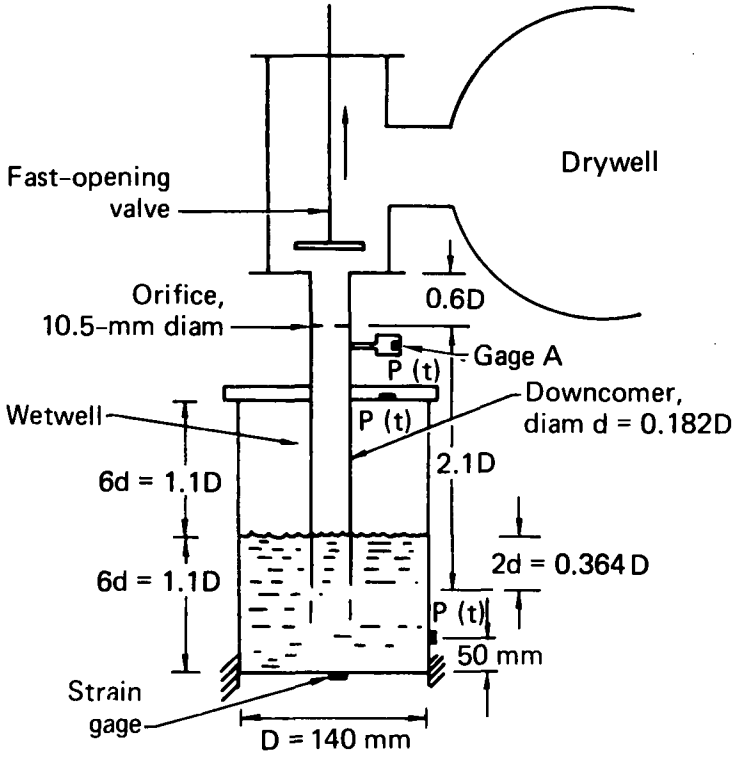


FIG. 6. Apparatus used for the MIT tank air-blowdown experiments.

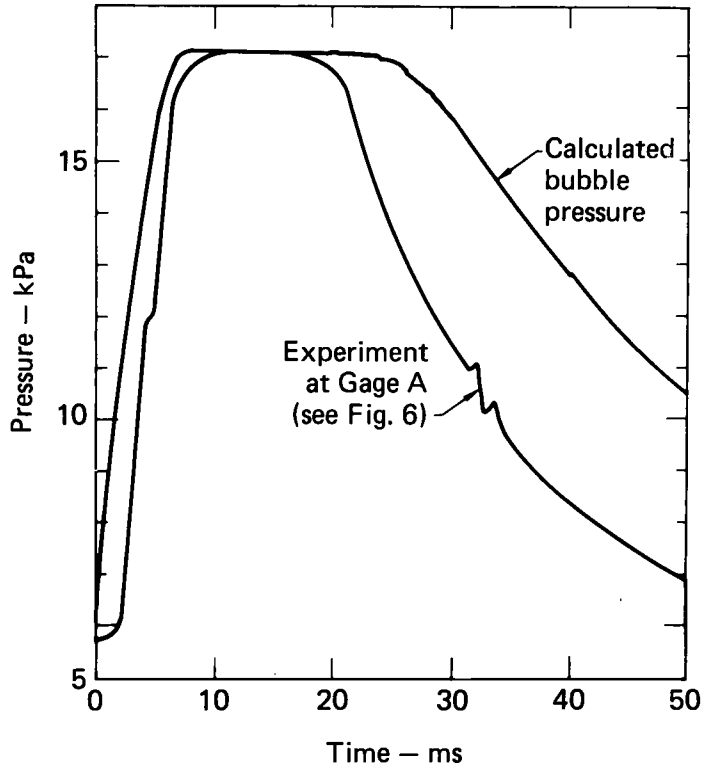


FIG. 7. Comparison of measured downcomer pressure and the bubble pressure calculated from an orifice-flow computer model for the MIT tank air-blowdown experiment.

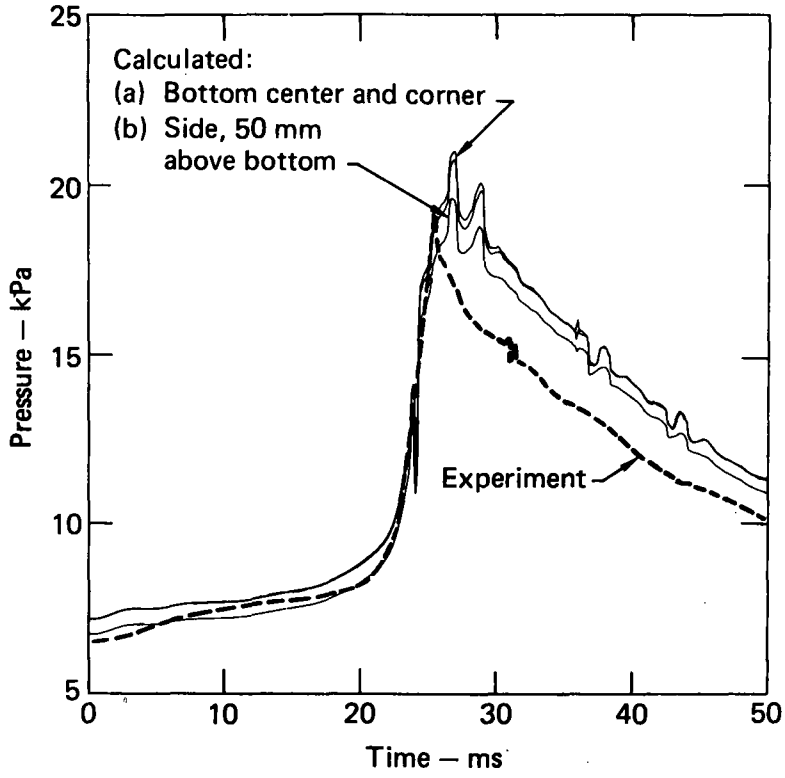


FIG. 8. Calculated fluid pressure-time histories at three locations in the MIT rigid-bottom tank and experimental pressures measured 50 mm above tank bottom. Times are normalized so that vent clearing times coincide.

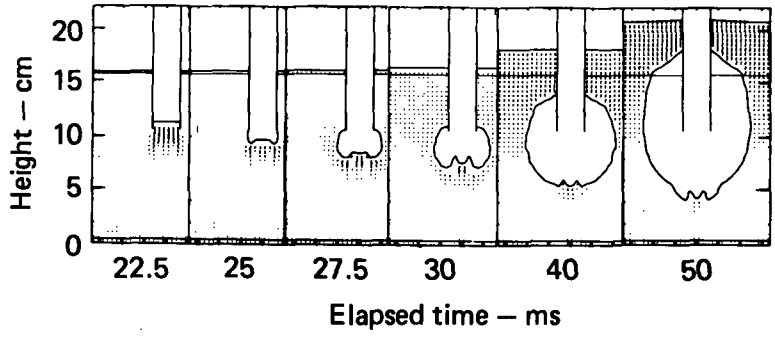


FIG. 9. Six calculated bubble shapes in the MIT rigid-bottom tank during a 27.5-ms interval.

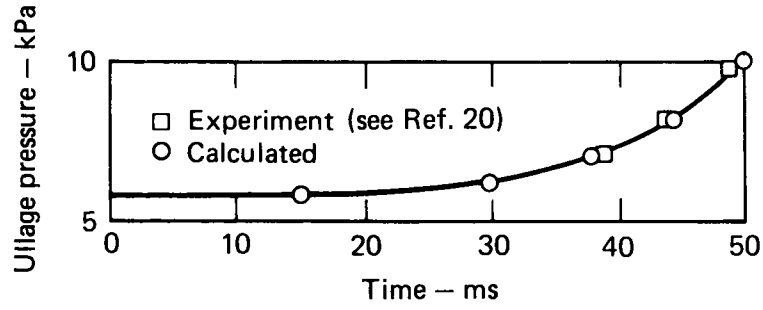


FIG. 10. Comparison of calculated and measured ullage pressure as a function of time for the MIT rigid-bottom tank.

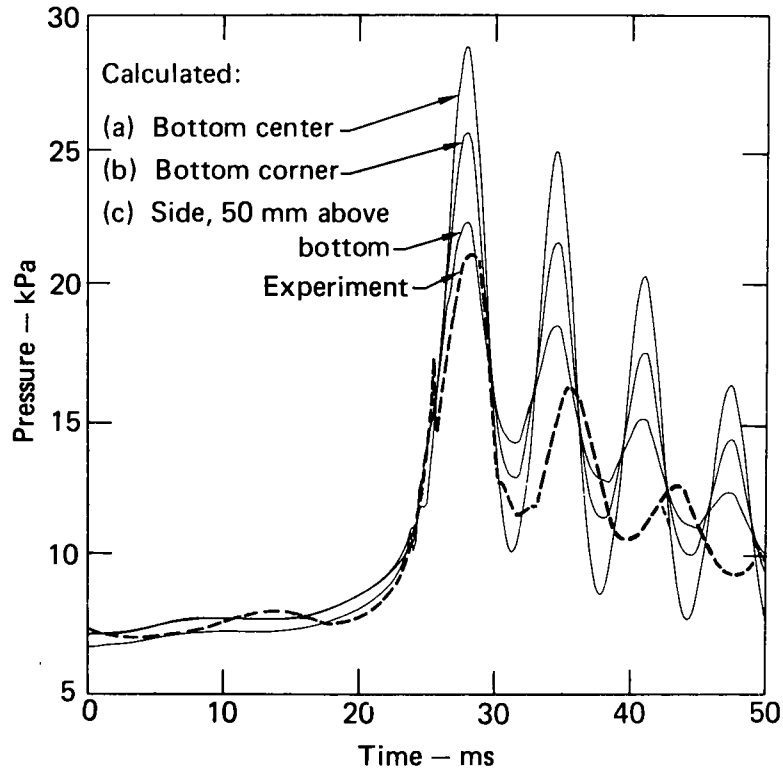


FIG. 11. Calculated fluid pressure-time histories at three locations in the MIT tank with the flexible 1-mm-thick bottom and experimental pressures measured 50 mm above the tank bottom.

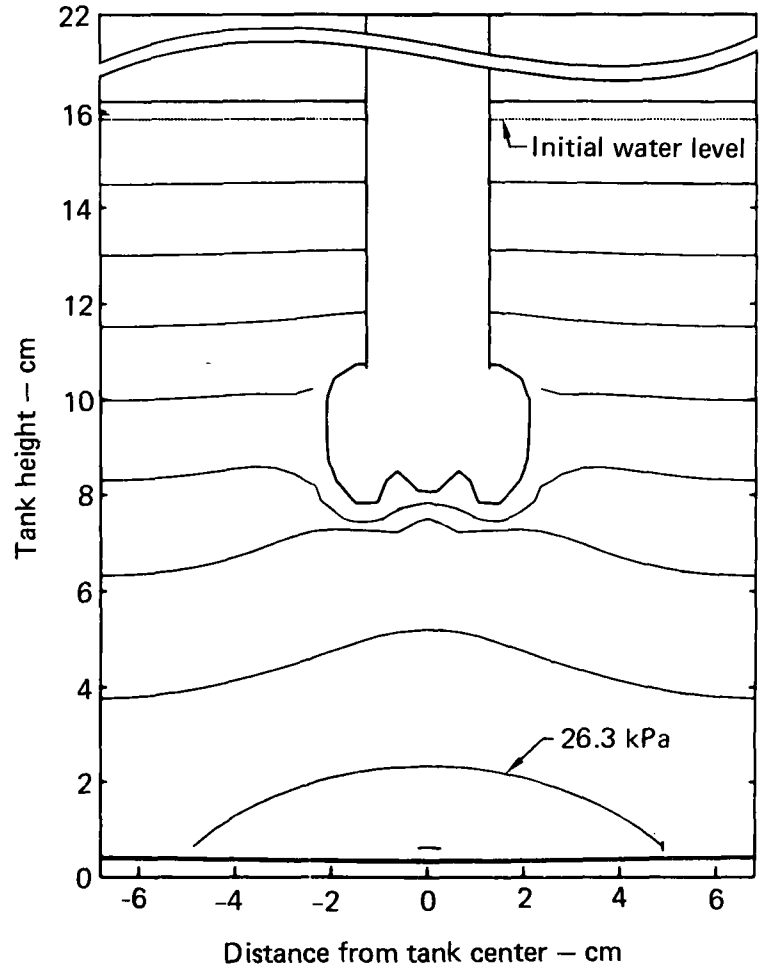


FIG. 12. Calculated pressure distribution after 28 ms for the MIT tank with the flexible 1-mm-thick bottom at a time of peak pressure.

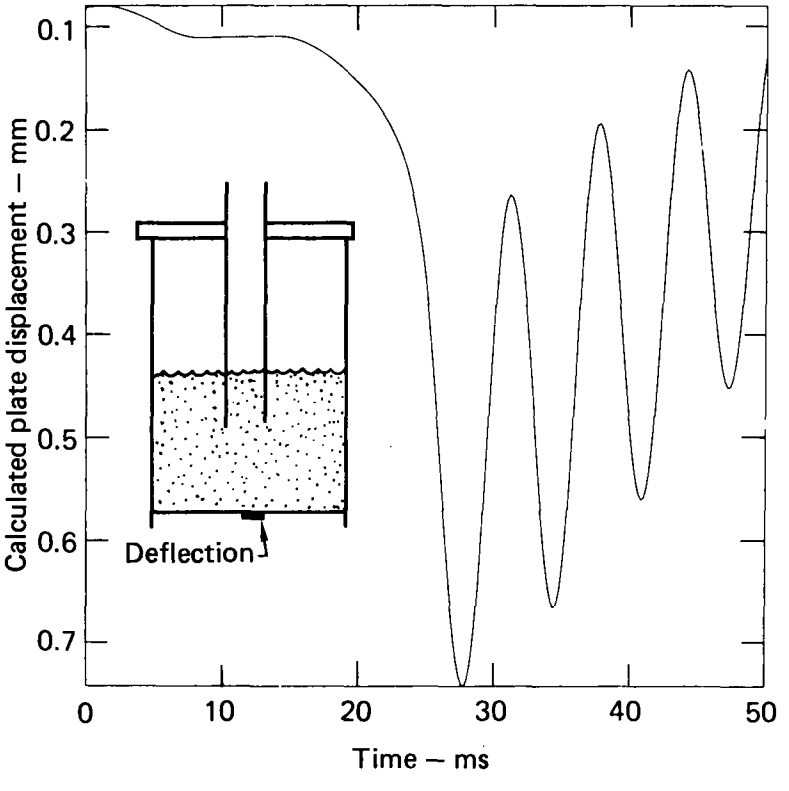


FIG. 13. Calculated displacement-time history of the center of the 1-mm-thick plate in the MIT tank.

# 5.0 APPLICATION TO MARK I BWR PRESSURE SUPPRESSION SYSTEMS ANALYZING 1/5-SCALE EXPERIMENTS CONDUCTED AT LLL

## 5.1 INTRODUCTION

A series of air blowdown tests were conducted on the 90°- and 7.5°-wetwell torus sectors of the LLL 1/5-scale Mark I pressure-suppression system to determine the effects of initial conditions and wetwell water levels on the tank pressures, the uploads, and the downloads. We developed the PELE-IC models in order to understand how vent clearing, bubble expansion, and pool swelling affect the torus sector loads. A computer parameter study determines the effects of pressurization rate, wetwell pressure, and downcomer fill level are also presented, and the three-dimensional effects for the 1/5-scale tests are discussed. The main focus of this section is the download and upload computations.

## 5.2 DESCRIPTION OF EXPERIMENTAL APPARATUS ANALYZED

Figure 14 is a model of the Peachbottom Mark I BWR pressure-suppression system with a cross sectional view of the toroidal wetwell and drywell. The 48 downcomer pairs are unevenly spaced due to the presence of the eight vent lines and the torus/flange connections. Figure 15a shows the LLL 1/5-scale test facility. Experimental tests with both the 7.5°-torus sector with one downcomer pair and the 90°-torus sector with 12 downcomer pairs were conducted simultaneously.[6] (The 7.5°-torus sector is actually a closed cylinder rather than a torus sector.) Both the 7.5- and 90°- 1/5-scale torus sectors are three dimensional because the downcomer vents are bent, round pipes rather than toroidal channels. Details of the experimental facility are covered in the 1/5-scale facility report[24] and are summarized in Table 5.1. The roughly half-filled torus has a major diameter of 6.8 m and a wetwell diameter of about 1.9 m. The downcomers of a given pair are separated by 4.9 m and are submerged 0.25 m into the pool. All steel used in the vessel is ASTM A537, Class 1, Grade A.

The 7.5°-torus sector is supported at the midsection by two steel structural legs bolted directly to a rigid reinforced concrete slab (see Fig. 15a bottom left corner). The 90° sector (see Fig. 15a right side) is

partially supported by trunnions on both sides of a center ring between the two dissected 45° sectors (see Fig. 15b) by a pair of steel columns bolted to the concrete slab. These columns, in addition to four ringheader support struts, contain load cells. The third 90°-sector wetwell support is below the left-end flange of the 90° assembly. The right-end flange is unsupported. Pressure transducers were located at several locations including the bottom torus center location, inside the downcomer pipe above the waterline, and in the ullage space and drywell. The initial ullage pressure is about one-fifth of an atmosphere and the pressurization rate of air blowdown is about 190 KPa/s.

We calculated the 1/5-scale tests conducted on both the 90° and 7.5° sectors. A plane strain model with channel downcomers was used with a vertical axis of symmetry containing the torus cross section centerline as shown in Fig. 16a. One pair of calculations was done in a donut configuration with the axis of symmetry at the torus center.

PELE-IC calculations* were done for the rigid- and flexible-wall toroids. The rigid-wall calculations were done with and without calling the finite element shell subroutine. The flexible-wall torus calculations with vertical support springs are shown in Fig. 17. The effects of the ringheader are not included here, but are discussed in a separate report.[25] The previous champ ringheader calculations with and without the ringheader impact showed the bottom pressure to be essentially the same but that the calculations with the ringheader indicated additional uploads from 214 to 250 ms. Typical rigid-wall, inviscid PELE-IC calculations ran to 200 ms using a time step of 0.2 ms and a convergence criterion of $10^{-4}$ $ms^{-1}$ with CDC 7600 CPU run times of about 1.5 min. Donut calculations with flexible structure used about 3.0 min of Cray-1 time.

## 5.3 PARAMETRIC SENSITIVITY ANALYSIS

Our first set of rigid-wall calculations was a parameter study for drywell pressurization rate, downcomer submergence, torus pool level, downcomer fill level, and initial wetwell pressure. Calculations with ±25% variations in the above parameters were compared to a nominal calculation using the

*We assumed synchronous downcomer discharge.

smoothed-downcomer pressure-time histories of experiment 1.3.1 ($90^{o}$ sector). We defined time zero to be experimental time (2.9875 s) when the pressurization starts. Runs with an unsmoothed-downcomer history showed little difference in terms of vent clearing time and peak bottom pressure.

The downcomer pressure was used as a driver at the moving water interface in either the downcomer prior to vent clearing or in the bubble after vent clearing. It should be noted that the parameter studies did not attempt to adjust or compensate the downcomer driver pressure for its dependence on the variables being perturbed. Details of the parameter study are given in Appendix F. This parameter study showed that a 25% change in downcomer submergence, pressurization rate, and change in wetwell pressure resulted in about a 10% change in the peak bottom pressure. The code version used for these calculations did not have provisions for calculating structural loads. Subsequent runs calculated load/time histories.

Our plane strain calculation of 1/5-scale experiment 1.3.1, the base case for the parameter study, is reported in Appendix F. In addition to a 16% increase in peak bottom pressure as compared to experiment, the PELE-IC results show vent clearing between 14- and 30-ms late. Similar discrepancies were found when we calculated 1/5-scale experiment 2.10 which had 6% less downcomer submergence than experiment 1.3.1. These differences can be traced to the assumption of plane strain behavior. Because of the out-of-plane restraint against wetwell fluid motion for this model, the fluid leaving the downcomer during vent clearing does not have the freedom of dispersion present in the actual three-dimensional geometry. An axisymmetric (donut) calculation of the torus did not produce any detectable change with respect to the plane strain calculation in vent clearing time, since the downcomers are modeled as toroidal channels rather than plane channels and the out-of-plane restraint is still present with respect to the fluid departing the downcomer. Additionally, the ratio of fluid volume in the downcomers to the fluid volume in a tributary segment of the torus is too large when plane strain behavior is assumed. The factor by which this volume ratio exceeds the actual ratio is approximately equal to s/d, where s is the length along the torus between downcomer pairs and d is the downcomer diameter.

A proper three-dimensional simulation of these two effects will permit a more accurate computation of experiment 1.3.1.

## 5.4 DEPARTURE FROM PLANE-STRAIN CALCULATIONS

### 5.4.1 Plane-Strain vs. Axisymmetric Calculations

To test our hypotheses of three-dimensional effects two single pipe geometries were analyzed. Both involved single on-axis downcomers, but one was plane strain (the downcomer is represented by a long channel and the major torus radius is infinite) and the other axisymmetric* (torus modeled as a sphere and downcomer represented by a round pipe). The two wetwell diameters were the same as were the flow width openings for the two downcomers. The exit velocity at vent clearing for the axisymmetric case was 30% greater than that for plane strain (10.3 m/s compared to 7.6 m/s) and the vent cleared 11 ms earlier than the plane strain case. A common vent pressure was used for each case. A plot of axial velocity and radial velocity (see Fig. 18) beneath the downcomer at the time of vent clearing illustrates the geometric effect. The velocity for the axisymmetric case is larger, but tends to decay faster as a function of distance from the end of the downcomer. These findings are in qualitative agreement with free jet theory (i.e., with momentum exchange arguments for unconfined jets). Peak bottom center pressures for the plane strain and axisymmetric geometries with the downcomer on axis were 52 KPa and 44 KPa, respectively. The corresponding peak dynamic pressures (obtained by subtracting the wetwell static ullage air pressure and the fluid gravity pressure from the total pressure) are 27 KPa and 19 KPa, respectively. Direct comparison between computed single-downcomer pressures (downcomer on axis) with experiment 1.3.1 are not too meaningful, because the additional fluid momentum from the other downcomer of the pair has not been accounted for. Some estimate of this effect can be obtained by examining the double-downcomer plane-strain (see Fig. 16) and the single-downcomer (on axis) plane-strain results and comparing the peak bottom center pressures from the two cases. In the single downcomer case, the bottom center pressure is calculated directly beneath the downcomer as 52.1 KPa, while for the double downcomer the bottom center pressure is calculated midway between the two downcomers at the bottom of the torus as 56.8 KPa. Based upon this ratio, the increase in pressure at the bottom center (due to an adjacent downcomer clearing simultaneously) is on

*Not to be confused with the axisymmetric donut calculation.

the order of 5 KPa. Adding this pressure increment to the axisymmetric single-downcomer on-axis result gives approximately 49 KPa (experiment 1.3.1 peak bottom pressure is 49.3 KPa); this indicates almost perfect agreement with the experiment in terms of vent-clearing hydrodynamics.

### 5.4.2 Finite Torus Diameter

One further comparison of peak bottom center pressure can be made between a plane strain calculation (infinite torus diameter with a single downcomer centered in torus cross section)* and an axisymmetric donut calculation (finite torus diameter and a single downcomer centered in torus cross section). This pair of calculations, unlike others, modeled both halves of the torus cross section. The axisymmetric calculation, therefore, did not assume an infinite major diameter. The peak bottom pressure for the donut calculation was found to be 3.6% lower than that of the plane-strain problem. As stated earlier, the vent clearing times were identical. A small portion of the 16% discrepancy between experiment 1.3.1 and our plane strain calculation is thus due to curvature of the wetwell torus.

## 5.5 LOADING RESULTS

Our final set of calculations investigated downloads and uploads in the $90^{\circ}$- and $7.5^{\circ}$-torus sectors. The downloads are produced by the momentum of the water at vent clearing. As the bubble expands and the water surface rises, the net load on the torus shifts upward until it reaches a peak before returning to the static condition. We computed the 1/5-scale uploads to gain insight into the physical mechanisms involved so that the unexpectedly higher (~20%) experimental uploads found in the $90^{\circ}$ sector, relative to the $7.5^{\circ}$ sector,[26] might be explained.

A plane strain model (see Fig. 16) was used with a vertical axis of symmetry containing the torus cross section center line. The torus was supported as shown in Fig. 17. Our calculations investigated the influence of both torus stiffness and flexible supports on uploads. Three typical vertical

*This calculation is the same as the plane strain (downcomer on axis calculation) except symmetry is not assumed.

load histories, computed from integration of the pressure distributions, are shown in Figs. 19a, b, c.

Figure 19a shows our calculated results for a rigid structure and support. A low-frequency response showing download and upload follows the initial static deflection. Figures 19b and c show our results for a flexible structure and support, where support motion was allowed only in the vertical direction. We obtained the same low-frequency response as the rigid calculation but with a high-frequency component superimposed. The latter frequency corresponds to that of a simple spring-mass system with a spring constant equal to the support stiffness and a mass equal to that of the structure plus a calculated effective water mass (about half the total water mass). This mass remains approximately constant for hard and soft spring supports. The support spring constant for Fig. 19b is about 16 times larger than that for Fig. 19c, and the calculated frequency differs by a factor of 4 as expected. The superposition of the three calculations (Fig. 19d), reveals that the response of the rigid structure represents the mean of the flexible-structure responses.

Figure 20 shows the interrelation between bubble dynamics and upload and the pressure contours at different periods of bubble growth. Important to the understanding of the upload phenomenon is the phasing between the bubble and pool pressure and the ullage pressure. In Fig. 20a the early pressure contours show a net downward force. The dynamics are still dominated by the force of the water pushing down as vent clearing occurs and the bubble starts to grow. As the bubble expands, the path of least resistance is towards the surface. A net upward force clearly appears in Fig. 20b. A high pressure region is located in the upper portion of the torus because of ullage compression. The lower section of the torus is now at a lower pressure. Later, the phase difference disappears, and the forces equilibrate as shown in Fig. 20c.

These calculations explain the upload phenomenon. Uploads are caused by bubble growth toward the free surface. This bubble growth produces a higher pressure region in the upper part of the torus. The movement of the structure and support contributes a relatively small high-frequency component to this main load time history. The distribution of the pressure contours of Fig. 20 shows that the geometry of the structure plays an important role in the magnitude of these loads. Hence, careful design can reduce them.

The two-dimensional nature of these calculations limits the conclusions that can be drawn. Extrapolating the computer results to a full $90^{o}$-torus sector, for example, gives downloads much larger and uploads smaller than the experimental results. Such an extrapolation implies much more water displacement than is actually the case. The downcomers are circular and discretely placed, but in the plane-strain analysis the downcomer is a continuous channel. So in our calculations bubbles cannot expand and interact in three dimensions. The calculations reported here, however, are sufficient to describe the general upload phenomenology.

## 5.6 DISCUSSIONS AND CONCLUSIONS

We have demonstrated the versatility of PELE-IC in calculating LLL 1/5-scale experiments with varying initial conditions or changes in the geometry. All calculations are two dimensional and our results are conservative with respect to the experimental bottom pressure associated with the downloads. In terms of uploads, PELE-IC is nonconservative with respect to experiment. Our calculations demonstrate the limitations of modeling a three-dimensional geometry with a two-dimensional computer code.

Three-dimensional vent clearing and pool swell hydrodynamics have been successfully calculated with two-dimensional models by proper consideration of two effects: (1) the geometric decay of fluid velocity near the downcomer for plane strain and axisymmetric calculations, and (2) the ratio of the initial fluid mass in the downcomers to the total fluid mass in a tributary volume of the torus. Plane-strain models are substantially in error on both counts, because of out-of-plane restraint against fluid motion and because of downcomers being treated as channels.

Axisymmetric models with downcomers on axis or with downcomers treated as equivalent annuli proved to be successful in predicting vent clearing time and peak bottom center pressure. As a result, it is suggested that a combination of two-dimensional (early time) and three-dimensional (structural response time) fluid-structure analysis may accurately and economically provide vent clearing and pool swell evaluations without recourse to a fully coupled three-dimensional treatment.

We have shown that uploads are neither dependent on the stiffness of the torus shell nor on the stiffness of the supports, but are a consequence of

wetwell liquid being accelerated upward by the growing bubble. Wetwell design contours can control upload magnitudes.

Shell flexibility affects the load-time histories by the addition of oscillations to the main signal after vent clearing.

The greatest limitation of PELE-IC in performing Mark I safety analyses is the code's inability to calculate three-dimensional fluid-structure problems. On the other hand, great care must be taken in attempting to substitute other computational devices (e.g., acoustic models) for PELE-IC which may be able to treat the three-dimensional aspects of the problem at the expense of neglecting bubble dynamics and other nonlinear fluid phenomena. Such phenomena control both the download and upload histories.

TABLE 5.1. Geometry material properties and initial conditions of 1/5-scale torus.

| | Experiment (1.3.1) | Calculation |
|---|---|---|
| Geometry | | |
| Torus wetwell inside diameter (2R), cm | 190.0 | 189.0 |
| Torus major diameter, cm | 680 ($90^{o}$ sector) | 680 or infinity |
| Pipe diameter, cm | 12.2 | 12.0 |
| Downcomer submergence, cm | 24.67 | 24.38 |
| Spacing between downcomers, cm | 48.77 | 48.20 |
| Wall thickness (h), cm | 1.905 | 1.905 |
| Water depth, cm | 90.67 | 90.67 |
| Material properties | | |
| Poisson's ratio[a] | 0.29 | 0.29 |
| Mass density,[a] $kg/m^3$ | 7.86 | 7.86 |
| Young's modulus,[a] GPa | $2.06 \times 10^6$ | $2.06 \times 10^6$ |
| Water temperature, $^{o}C$ | $21.7^{o}$ | - |
| Initial conditions | | |
| Initial wetwell pressure, KPa | 20.3 | ~20.4 |
| Initial downcomer pressure, KPa | 20.3 | ~20.4 |
| Drywell pressurization rate, KPa/s | 187.8 | 187.8 |

[a]ASTM A537 Class I, Grade A steel.

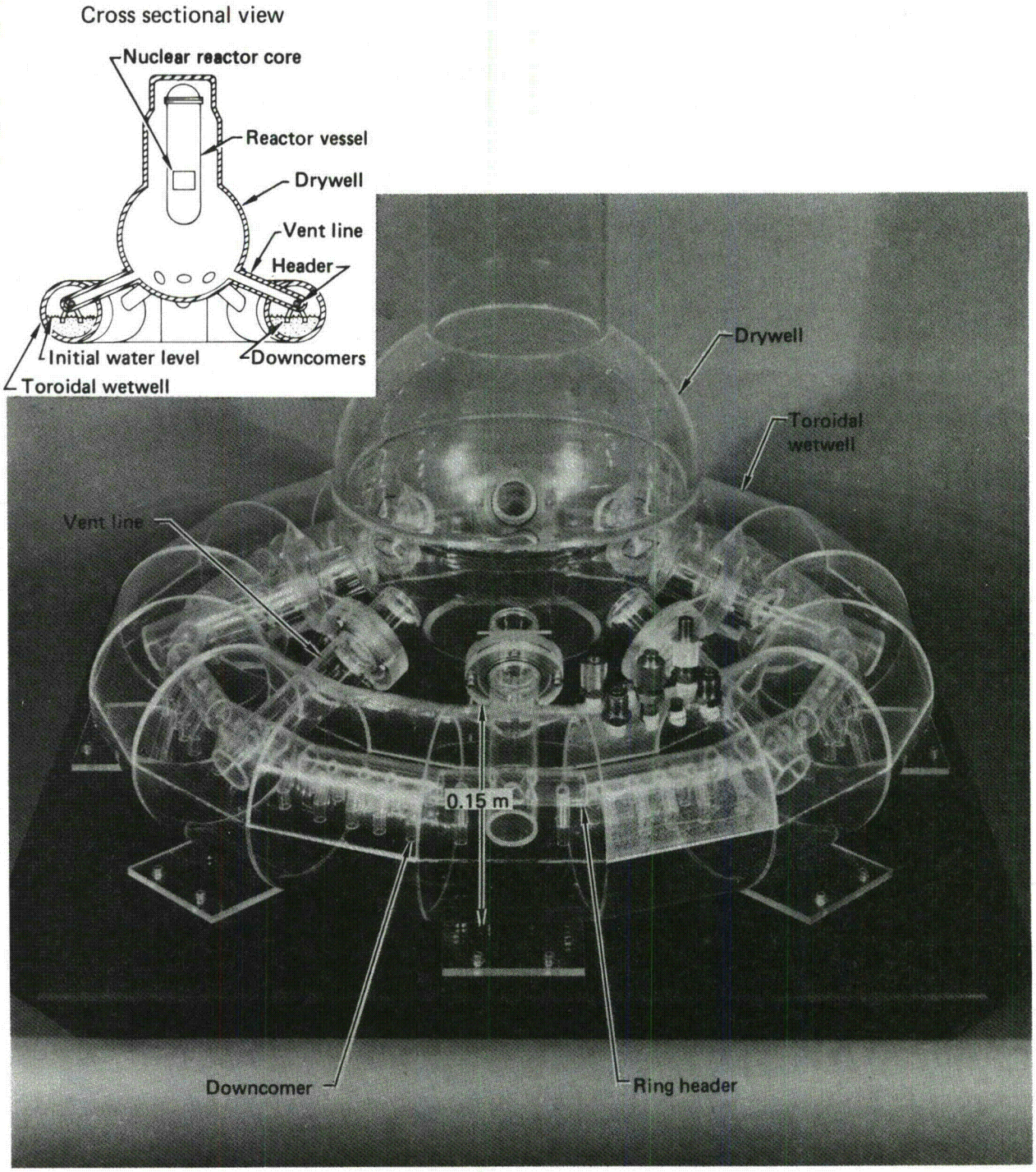


FIG. 14. Scale model (1/64 size) of the Peachbottom Mark I BWR pressure-suppression system.

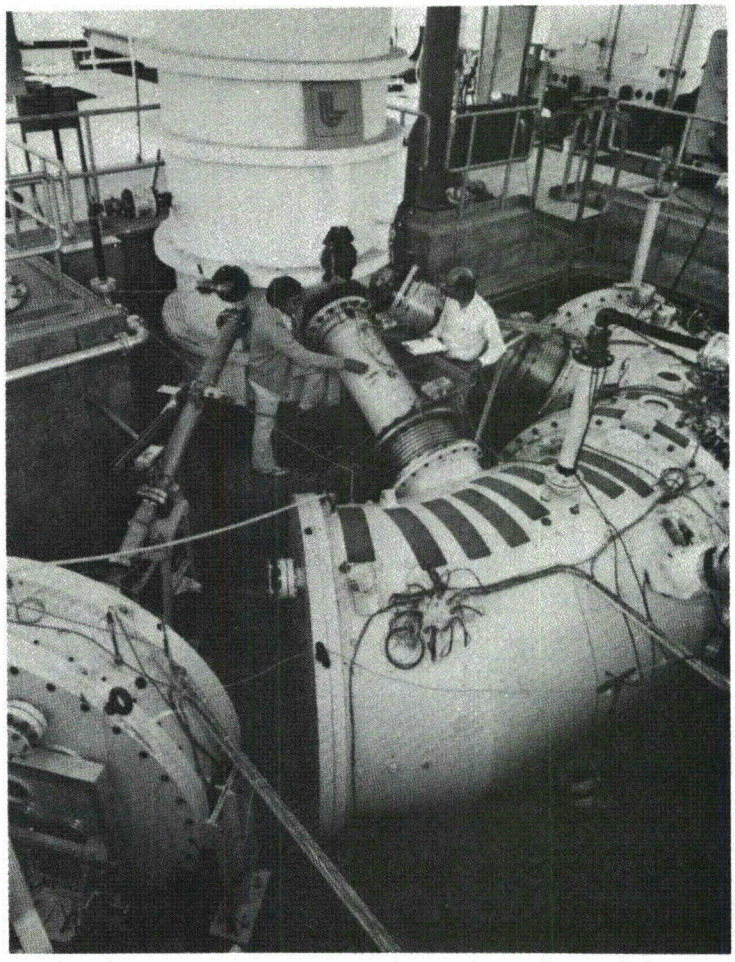

(a)

(b)

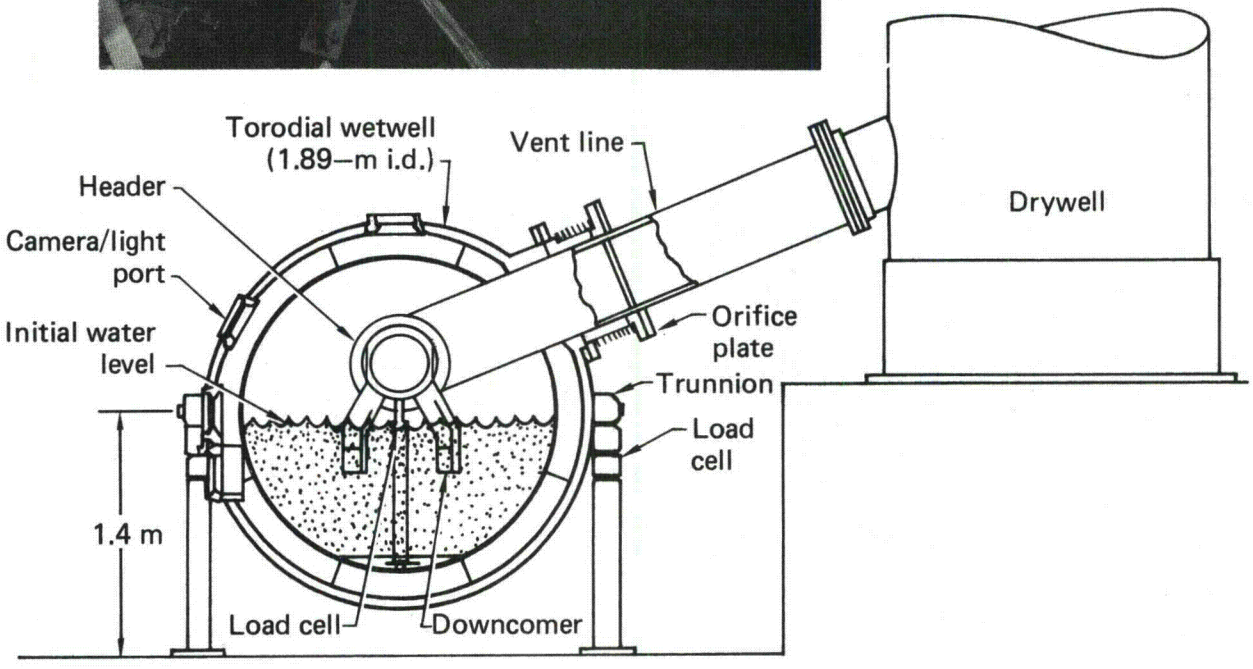


FIG. 15. LLL 1/5-scale experimental facility. (a) 7.5°- and 90°-wetwell torus sectors, vent lines and drywell. (b) Cross section of toroidal wetwell.

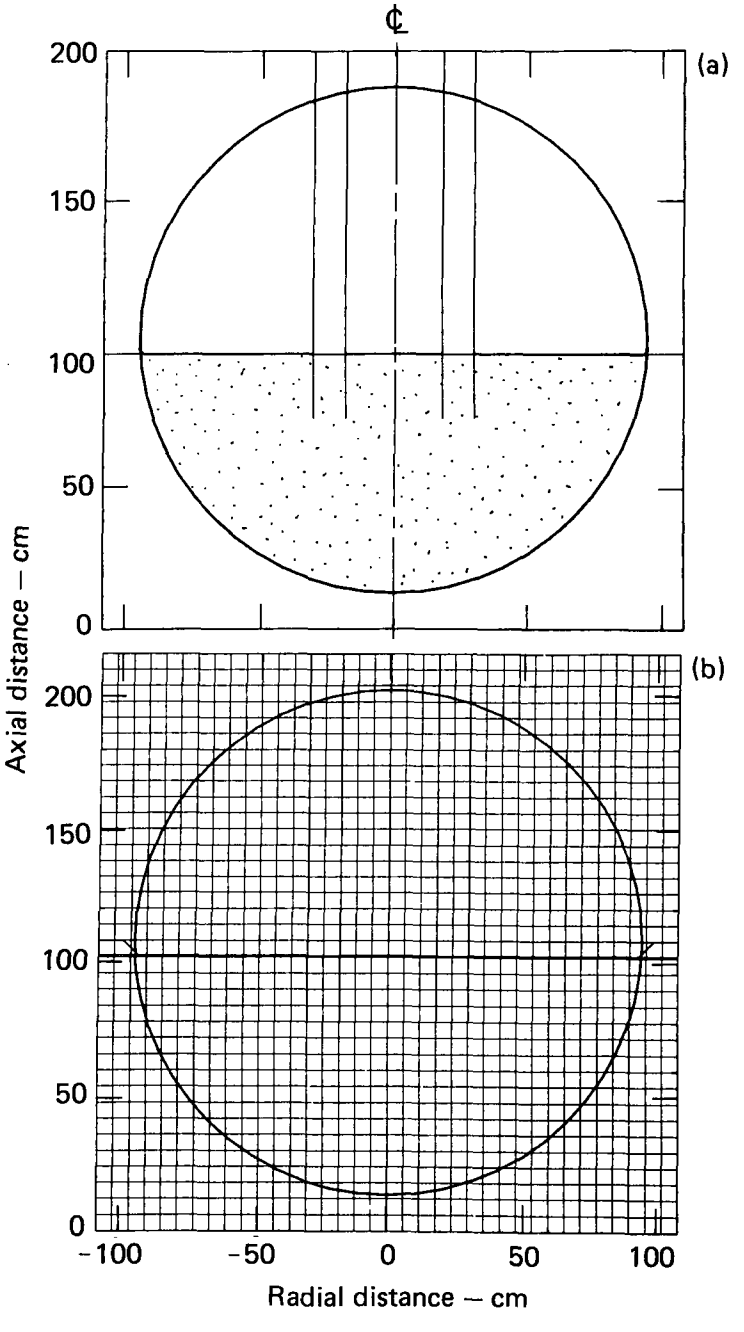


FIG. 16. LLL 1/5-scale torus calculated geometry. (a) Torus walls and downcomer vents. (b) Eulerian grid overlaying shell--648 cells and 30 shell elements.

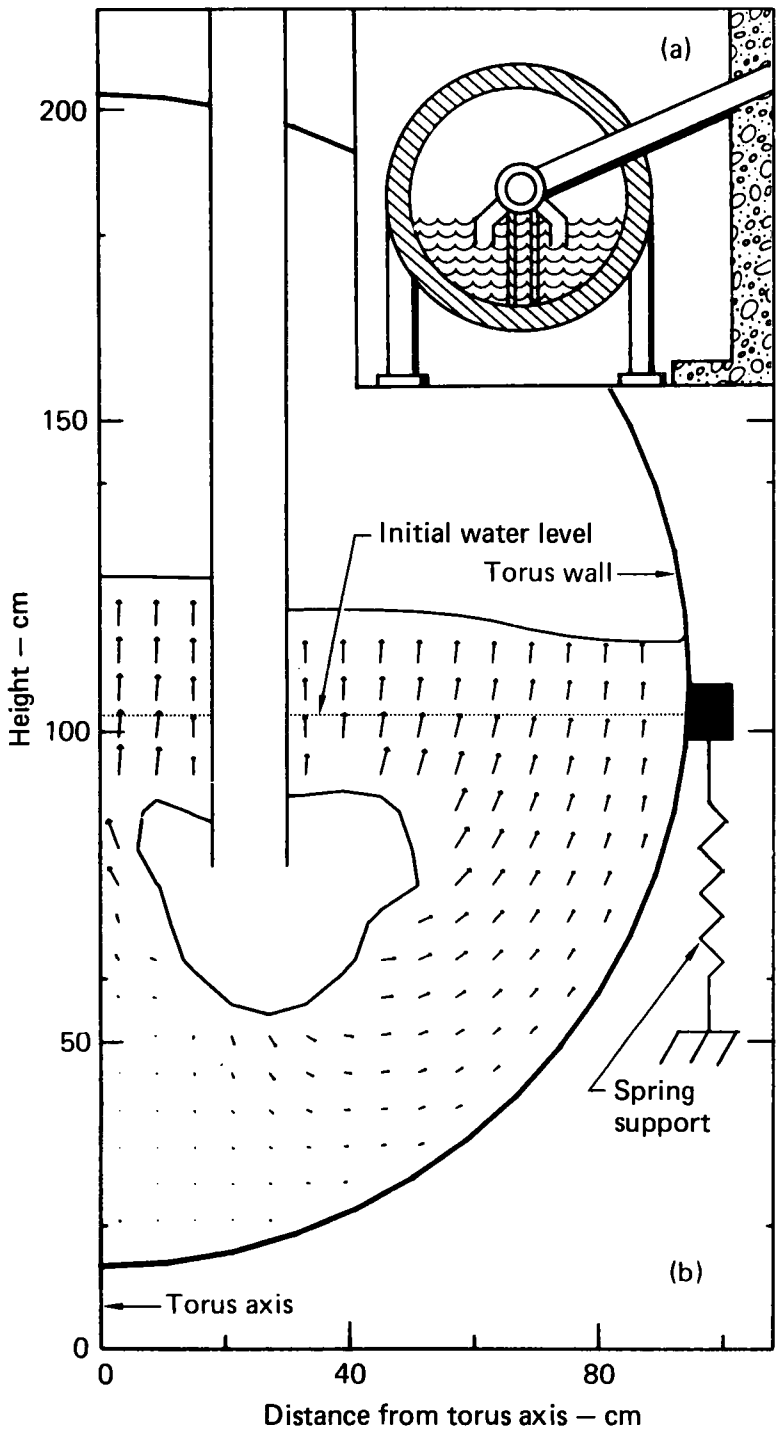


FIG. 17. LLL 1/5-scale plane strain model of the Mark I BWR. (a) Basic geometry showing a cross section of the torus to be modeled. (b) Calculated geometry showing typical bubble shape with arrows representing velocity vectors.

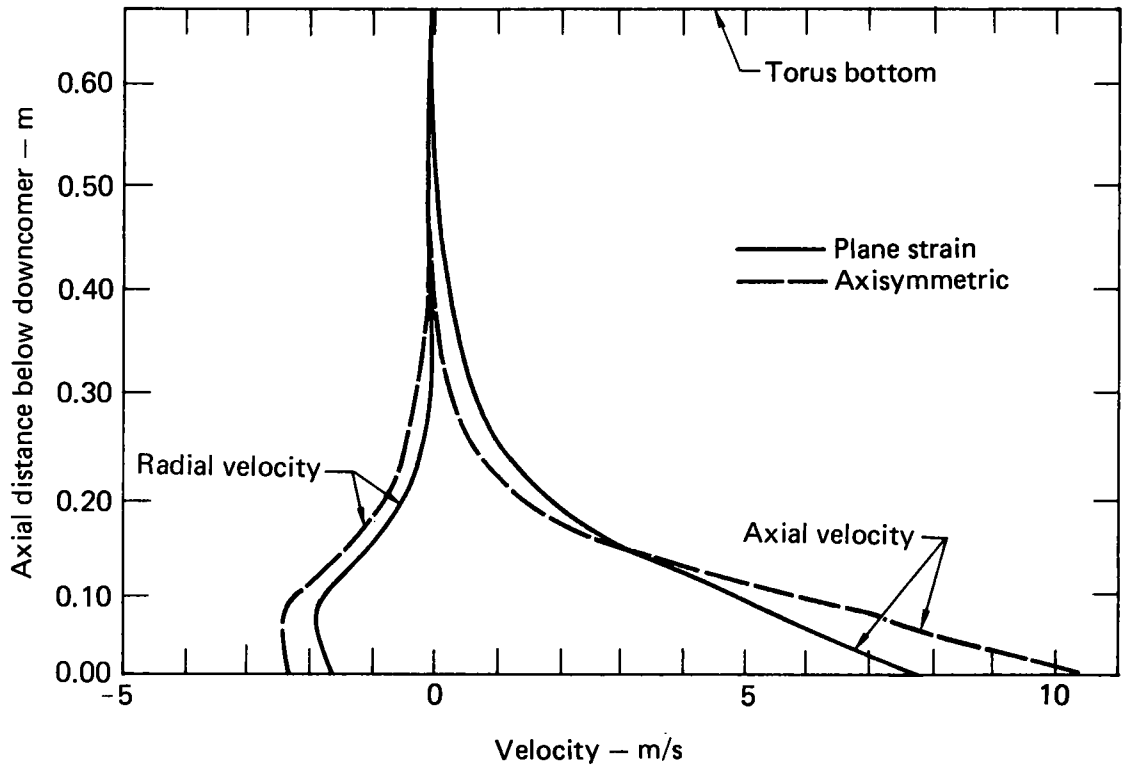


FIG. 18. Radial and axial velocity profiles below the downcomer exit for plane-strain and axisymmetric LLL 1/5-scale calculations.

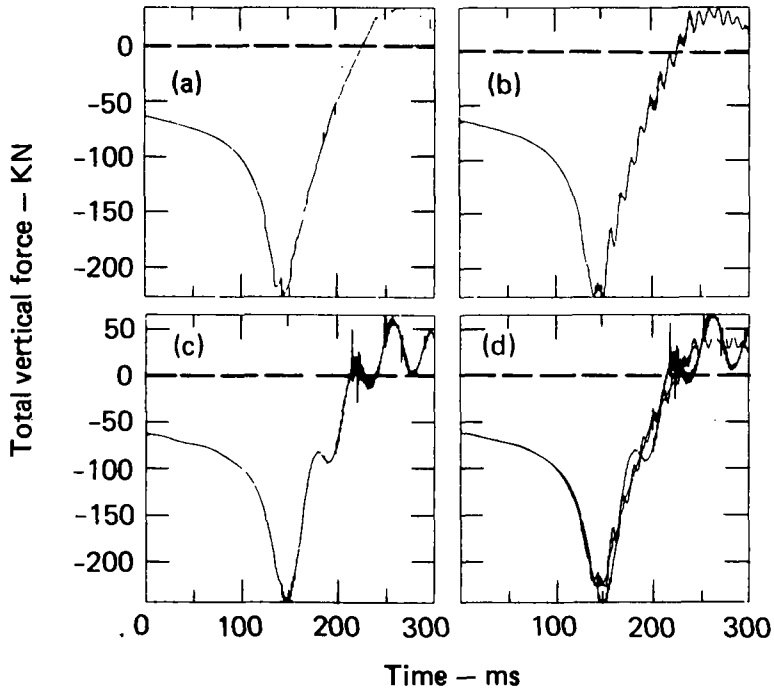


FIG. 19. Calculated uploads and downloads during vent clearing in the LLL 1/5-scale torus. (a) For rigid structure and supports. (b) Flexible structure and supports. (c) For flexible structure with 1/16 the support stiffness of (b). The sharp pressure spikes result from numerical difficulties absent in subsequent calculations. (d) Superposition of previous three cases.

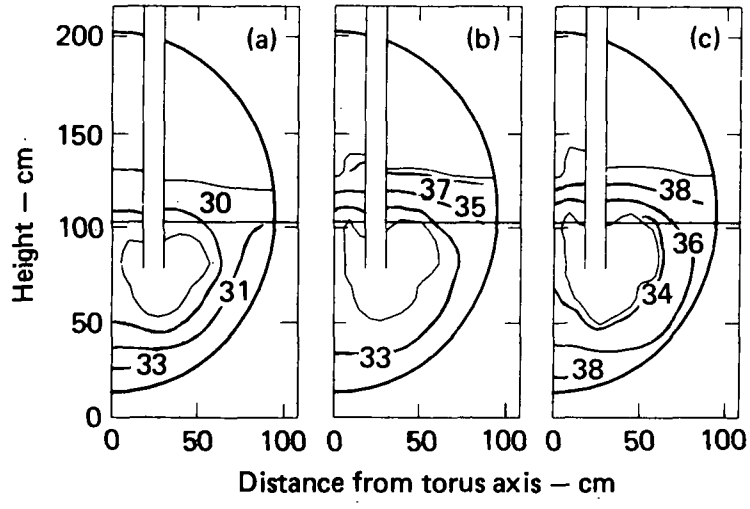


FIG. 20. Calculated bubble growth and pressure contours in the LLL 1/5-scale torus during air blowdown. (a) After 200 ms. (b) After 260 ms. (c) After 280 ms. The pressure contours are in kPa. The horizontal line is the initial water level.

# 6.0 APPLICATION TO MARK II BWR PRESSURE-SUPPRESSION SYSTEMS ANALYZING SCALED EXPERIMENTS

## 6.1 SIMULATION OF A HARMONICALLY DRIVEN WATER TANK

A test of the low-amplitude, long wavelength acoustic capability of the PELE-IC code was provided by the problem of dynamic response prediction for a cylindrical, water-filled tank harmonically excited by a top surface piston. The tank bottom is closed by a rigid plate mounted on hinged supports. Fluid-structural interaction experiments on this system were conducted for the Electric Power Research Institute by the Aeronautical Research Associates of Princeton (ARAP)[27] and offer a geometric similarity useful for verifying the PELE-IC code for calculations of the General Electric (GE4T) (Mark II) tests described in the next section. For the present problem we calculate the second symmetric wall-bending mode and compare our results with ARAP experiments.

ARAP's experimental apparatus, which includes an aluminum tank and an electromagnetic shaker-driven piston, is shown in Fig. 21a. Of the three tanks tested--steel, aluminum, and acrylic--we chose the aluminum tank because of its intermediate rigidity. This tank has a column of piezoelectric transducers located 4.13 cm from the centerline, which allows pressure to be measured as a function of height. The piston was located approximately 3-cm below the waterline and had a clearance of about 0.5 cm between the outer periphery of the piston and the cylinder wall. A 520-Hz sinusoidal frequency was applied just below the water surface; the frequency represents a resonance discovered in the ARAP experiments by a discrete frequency sweep (i.e., altering the electromagnetic shaker driving frequency in discrete jumps while monitoring vibrational amplitude of several points in order to detect resonance). The tank bottom is a rigid, substantially thick steel plate hinged by means of a thin, circumferential flexure strip, as shown in Fig. 21b. The strip is wedged to a base flange that is screwed to the sub-base plate which is, in turn, bolted to the concrete floor.

Table 6.1 gives the material properties and geometry of the slender ARAP tank. The tank's inside diameter (2R) is 0.18 m and the height (H) is 0.93 m. The geometry ratio (H/R) and the sidewall thickness-to-radius ratio indicates that the bending terms are small. The Strouhal number ($\omega R/a$), together with

the (H/R) ratio, provide clues on acoustic wavelength effects and radial variations in the water pressure.

For the PELE-IC calculations we modeled the tank walls and bottom as a continuous aluminum shell overlaid with a rectangular Eulerian grid, as shown in Figs. 22a and 22b. At the present time, PELE-IC can model only one shell material; therefore, the tank bottom thickness was scaled by 1.44 to maintain the same bending stiffness as steel. Calculations with the bottom plate thickness scaled by a factor of three gave the same mode shape. However, a calculation with the bottom plate thickness of about the same thickness as the side wall produced the next higher axisymmetric (sidewall) mode. The bottom hinged edge supports were modeled by placing a single extremely rigid vertical stiffener ring on the outer bottom shell node. A velocity (piston) boundary condition corresponding to an experimental acceleration history (Fig. 23) was applied to the top row of Eulerian cells. Note that the water surface was excited in the PELE-IC analysis, whereas the piston lies somewhat below the surface water level. All axisymmetric calculations using a time step size of 0.05 ms were run out to four milliseconds and consumed two minutes of Cray-1 CPU computer time. A viscosity corresponding to that of room temperature water was used in the calculations.

The calculated bottom center pressure for the aluminum ARAP tank excited at 520 Hz is shown in Fig. 24a. Note that the initial pressure reflects the gravitational head about which the pressure oscillates. The radial variation in pressure is less than 2% at the tank bottom but as much as 8.3% at the water surface. A comparison of the normalized axial pressure distribution (pressure mode shape) is shown in Fig. 24b. Calculated data at times of peak compression and tension are compared to experimental data taken in compression. The pressure plotted is the calculated pressure minus the local static gravity head, which is then normalized to the maximum pressure occurring at that time. A null modal circle for this pressure occurs at an elevation of 0.5H at t = 2.25 ms and at 0.6L at t = 3.25 ms. Cylinder wall motion is represented by the velocity plots in Figs. 25a and 25b for these same two times, respectively. Null radial displacement modal circles occur at an elevation of about 0.33H at t = 2.25 ms and at 0.66H at t = 3.25 ms. Note that while the pressure mode shape is approximately symmetric about a mid-height plane, the velocity mode shapes are inverted images of each other.

The ARAP calculation is a useful exercise of PELE-IC because it demonstrates the capability of the code to calculate long wavelength axisymmetric acoustic modes in a cylindrical geometry, similar to the GE4T tank. The fluid-structure iteration effect can be appreciated by observing that the corresponding in-vacuo natural frequency of the aluminum cylindrical shell is about 9000 Hz, and the interaction reduces this to about 500 Hz. At the same time the acoustic wavelength is about three meters or about thirty times the tank radius--indicating the validity of our incompressibility assumption--yet the flexible structure contributes an apparent acoustic effect as evidenced by the axial variation in pressure. In summary, an incompressible calculation has accurately predicted an n = 2 wall bending mode seen in ARAP's harmonically driven tank experiment at 520 Hz.

## 6.2 THE GENERAL ELECTRIC TALL TEMPORARY TEST TANK (GE4T) EXPERIMENTS

In order to control the pressure in the reactor cavity (drywell) following a loss-of-coolant accident (LOCA), some General Electric BWR designs incorporate a pressure suppression pool with vertical downcomers (the Mark II system). A set of phenomenological experiments characterizing the Mark II design has been conducted in the General Electric Temporary Tall Test Tank (GE4T) which resulted in a variety of stable and unstable steam condensation events in the pool. The dynamic response of the GE4T during these events was measured, and these data, together with analytical models, are being used to develop design criteria and loading functions for Mark II equipment.

The purpose of these PELE-IC calculations is to compare the fluid/structural dynamic response characteristics for variations in wall stiffness, the type of pressure signature, various downcomer vent lengths, the effects of the vent acoustics, and compressibility effects.

The PELE-IC results in this section focus mainly on the GE4T parameter studies rather than comparisons with experimental data. Most of the experimental data[28-30] are proprietary. Reference 31 is a non-proprietary summary report.

The partially filled cylindrical GE4T tank is a single vent chugging facility operated by General Electric that may simulate the performance of a Mark II BWR pressure-suppression system under LOCA conditions. This facility approximates a unit cell of a full-scale Mark II containment system. The GE4T

tank is a tall, thin-walled, upright cylinder with thick end plates, several circumferential stiffeners, and a single central downcomer.

### 6.2.1 Experimental Apparatus and Computer Model

Figure 26 shows the GE4T experimental apparatus and a diagram of the actual multivent torus configuration. Table 6.2 gives details of the GE4T geometry and material properties. The sealed steel tank is 16-m high, roughly 38% water filled, and has a tank height to radius ratio of about 15. The downcomer pipe is submerged about 2.5 m, and the tank walls are 1.59-cm thick. The 10.2-cm-thick base is secured to a concrete pad through the flange at the bottom of the cylinder walls.

For one set of tests air and steam are injected from the drywell into the downcomer causing chugging/condensation oscillation to occur at the downcomer exit. Chugging is an unstable, irregular steam condensation process associated with an oscillatory motion of the steam-water interface occurring at the end of the blowdown process. Condensation oscillation, another chugging type, has regular pressure oscillations but with frequencies corresponding to the vent acoustic frequencies. A more detailed description of chugging is given in Appendix A. Typical experimental pressure time histories for these tests ran to 768 ms. Other tests designed to simulate a single chugging event were driven by a collapse of a partially evacuated belljar placed under the downcomer exit. Pressure transducers were located at the bottom center, bottom half-radius, at the downcomer and at several locations on the cylinder wall. Because we have calculated the collapsing belljar experiments with rigid walls these calculations are of little interest. In this section, we present only the chugging/condensation oscillation calculations with flexible walls and ends.

Axisymmetric PELE-IC calculations of the GE4T tank used a continuous flexible finite-element shell of variable thickness and a rigid downcomer, as shown in Fig. 27a. Extra shell zones were added at the tank side corners where sharp gradients in bending deformation occur. A rectangular Eulerian mesh (see Fig. 27b) consisting of 972 cells overlaid the shell. Void cells in the ullage airspace are automatically deleted during the calculation. The bottom flange support was modeled as an extremely stiff vertical stiffener placed at the outermost base plate node. Ring stiffeners on the side walls

were used in only one calculation. The kinematic viscosity corresponded to water at room temperature and was used for all calculations. No shell damping was added.

The initial ullage pressure was 275 kPa. The downcomer is assumed to be precleared, i.e., a mass flow rate of steam sufficient to clear the vent of water prior to the chug/condensation oscillation was assumed. Then a prescribed pressure time history is applied to the moving free surface in the initially precleared downcomer.

The actual pressure time history (pressure source function) at the liquid-vent interface is coupled to the interfacial thermal-hydraulics there and to the flow field within the liquid occupying the wetwell. The possibility of a change in the prescribed source pressure as the result of liquid-vent interface motion has not been considered in these calculations. We recognize that the simultaneous prescription of an initially precleared downcomer (with no bubble volume) and a source pressure overspecifies the initial condition of the problem. However, use of both prescriptions will not influence the fluid-structure frequency response for any prescribed pressure history provided the prototypical bubbles for the GE4T tests (and bubbles from our calculations) displace little liquid within the wetwell. Our calculations have demonstrated that the liquid-vent gas interface moves little for all pressure histories considered.

A typical GE4T calculation, using a time step of 0.05 ms and a convergence criterion $\epsilon = 10^{-6}$ $ms^{-1}$ ran to 200 ms using 22 minutes of Cray-1 CPU time. Calculated pressures were selected at the bottom half-radius and on the side wall at an elevation of 465 cm, and Fourier transforms of these PELE-IC pressure histories were performed by the method discussed in Appendix D.

### 6.2.2 Calculations

The two forcing functions used in the PELE-IC calculations are shown in Fig. 28. The first forcing function is a 50-ms triangular pulse, rising 6.9 KPa above the reference pressure. The reference pressure is the sum of the initial ullage pressure and the static pressure corresponding to the downcomer submergence. The second forcing function is a 55-ms pressure pulse consisting of a sharp, 5-ms negative pressure spike, which models the bubble collapse, followed by a 50-ms triangular pulse, which models fluid leaving the

downcomer. This pulse, called the WPPSS (Washington Public Power Supply System) pulse, has been suggested as being representative of chugging/condensation oscillation and has been constructed, in terms of amplitude and pulse shape, to conservatively bound an experimental amplitude-frequency envelope formed from 137 preselected GE4T chug pulses. The GE4T data base used a 29.3-m downcomer, whereas the actual Mark II containment has a downcomer length of about 12.2 m.

We modeled vent acoustics in some of the PELE-IC calculations by including the organ pipe reflections of the input pulses (see Fig. 28) in the pressure time history applied at the vent exit. Details of the acoustic pipe model used to calculate the acoustic reflections are given in Appendix C.

Our first set of calculations examined the static gravitational and dynamic deflections of the GE4T tank shell. Axial deflections of the thick end plates and the radial deflections of the thin side wall are shown in Fig. 29. Static end plate axial deflections are an order of magnitude larger than the radial deflection of the side wall, but the dynamic axial deflections of the end plates are two orders of magnitude larger than the dynamic radial side deflections. Also, the dynamic axial motion of the side walls dominates the radial motion. The displacement profiles at the top and bottom corners spatially oscillate due to the discontinuity in bending stiffness between the end plates and the thin cylindrical shell. In order to examine the effects of these spatial oscillations on the fluid-structure vibrational characteristics, a model with separate end plates and a cylinder (see Fig. 29) was constructed. Either this model or the continuous shell provided approximately the same deflections and pressure histories. In subsequent calculations we used a continuous steel shell.

Our second set of PELE-IC calculations was designed to isolate the GE4T frequency components associated with the cylinder wall and tank bottom. (An earlier attempt to perform an eigenvalue analysis using a Lagrangian finite element code was unsuccessful due to ill-conditioned matrices and spurious modes.) For one calculation, calculation A, the axial motion of the bottom plate was constrained. Calculation B constrained the radial motion of the cylinder walls and is the limiting case for continuous ring stiffeners. Both calculations A and B used the WPPSS pulse without acoustic reflections as a forcing function in a precleared downcomer. Figure 30 compares the bottom pressure-time histories and the Fourier spectra of these two histories. These

Fourier spectra were calculated only for a partial history--after the driving pulse has ended--in order to exclude the contribution from the driving transient. Note that a 42-Hz frequency component is associated with the bottom plate and the 57- and 68-Hz components are associated with the cylinder walls. An examination of deflection component histories for the center of the bottom plate and for points both above and below the water surface on the cylindrical shell for the fully flexible GE4T geometry supports this observation. For instance, the axial deflection at the center of the bottom plate shows a pronounced 38-to-40-Hz signal, whereas the wall axial deflections exhibit predominantly 60-Hz motion. Radial deflections of the wall below the water surface display the effects of fluid loading and, therefore, are similar to the bottom plate 38-to-40-Hz response; above the water surface, on the other hand, radial deflections conform to wall axial 60-Hz vibrations. The fluid velocities are almost entirely vertical, so that radial shell motion below the water surface appears to be a function of pressure coupling through the fluid to the bottom plate.

A point of interest is the approximately 5-Hz (see the partial time histories in Fig. 30a) modulation of the 65-Hz carrier frequency when the bottom plate is restrained against axial motion. In this example, the fluid velocity is no longer virtually vertical, but includes conversion from vertical to radial motion as the fluid particles stagnate against the rigid bottom plate. The modulation is associated with a beat frequency between a radial breathing mode (~70 Hz) and the longitudinal vibration mode (~60 Hz). The radial and axial deflections of the cylindrical shell wall below the water surface are $90^{\circ}$ out of phase with each other, rather than the $180^{\circ}$ out of phase that is typical for a fully flexible calculation. We find the 5-Hz frequency component to be independent of kinematic viscosity, but dependent upon compressibility. A compressible calculation (sound speed equal to 740 m/s) with a rigid bottom had no detectable modulation.

Frequency data for the two partially-flexible calculations--rigid bottom plate, flexible side wall; rigid side wall, flexible bottom plate--are summarized in Table 6.3. The amplitudes are listed from largest to smallest, reading from left to right. Typical error bounds on the frequency components are from ±2 to ±4 Hz, depending on the temporal duration of the sampling interval. Data in Table 6.3 are given for two locations: the bottom half radius location and at an elevation of 465 cm on the side wall. Note that the

15- and 25-Hz frequency components occur in each of the two calculations. These frequency components of lesser magnitude are of the same order of magnitude as the spurious contents introduced as a result of finite time domain sampling during the determination of the Fourier spectrum, as discussed in Appendix D. Because of this similarity, the smaller amplitude peaks in the spectra should not be given too great an emphasis.

The next pair of calculations compared the GE4T dynamic response for the triangular and WPPSS pulses (see Fig. 28) without vent acoustics. Bottom pressure-time histories for these calculations and their Fourier spectra are presented in Fig. 31. Note that the triangular pulse tends to excite the bottom plate and side walls, whereas the WPPSS pulse excites mainly the bottom plate. Again, the spectra were calculated for the portion of the response after the input pulse has ended.

The Fourier spectra of the triangular and WPPSS pulses were computed separately so that the transient contributions of the forcing function to the fluid-structure response could be evaluated. The WPPSS pulse frequencies are given in Table 6.4. Next we used an acoustic pipe model (see Appendix C) to compute the acoustic pressure reflections and the Fourier spectra of these reflections. Reflected organ pipe pressures of the triangular pulse for the 28.6- and 14.3-meter downcomer vents are shown in Fig. 32. Fourier spectra of the reflected pressures are shown in Fig. 32b and 32d. The downcomer was assumed to be open at one end (simulating a drywell pressure boundary condition) and closed at the other end where the chugging pressure pulse is applied (simulating the high impedance of the wetwell water). Note that the 29-m vent length corresponds to the GE4T configuration, whereas the 14-m vent corresponds roughly to the Mark II vent length.

The reflected pressure time history shown in Fig. 32a and 32b begins at about 118 ms, approximately equal to the round-trip travel time for the pulse up and down the pipe. Each pulse reflection at the water surface causes a sign change in the signal. Frequencies of the reflected pressure are indicated next to its corresponding peaks in Fig. 32b and 32c. Theoretical frequencies shown in parentheses correspond to the classical organ pipe frequencies given by

$$f_n = \frac{(2n - 1)c}{4L} \quad , \qquad n = 1, 2, 3, \ldots ,$$

where the steam sound speed c is 488 m/s and L is the downcomer length.

Reflected pressures and their Fourier spectra for the WPPSS pulse are shown in Fig. 33. Again, the calculated and theoretical frequency components are shown in Fig. 33b and 33d for the two vent lengths, with a summary in Table 6.4. Note that the reflected triangular pulse is masked somewhat by the higher frequency oscillations. Both the triangular and WPPSS organ pipe calculations were run for 270 ms with a Courant number of 0.6. Note that the Fourier amplitudes for the shorter vent length are roughly 30% higher than those of the longer vent length. The characteristics of the Fourier amplitudes can be modified by either changing the chugging forcing function (pressure pulse) shape or the vent length.

Our next pair of PELE-IC calculations included the reflected acoustic signal for the WPPSS pulse in the forcing function applied at the downcomer exit. For the first 55 ms the forcing function is as shown in Fig. 28b; then, at the time of arrival of the reflected signal, the time history is as shown in Fig. 33a for L = 29 m, and Fig. 33c for L = 14 m. As mentioned previously, these vent lengths roughly correspond to either the GE4T or the Mark II downcomer lengths, respectively. Results for these calculations are shown in Fig. 34. Here we show the bottom pressure-time history at half radius location out to 274 ms, with the Fourier spectra of these pressures calculated for the entire response history. The dominant fluid-structure frequency is about 39 Hz. Note that the effect of the shorter downcomer length is to increase the Fourier amplitude of this particular frequency component by about 80%. The bottom pressure amplitude is also larger for the shorter vent length.

Prior to the time of arrival of the acoustic reflection (indicated by the arrows in Fig. 34a and 34c), the response histories show a mixture of predominantly 39- and 63-Hz frequency components. After the acoustic reflection is applied, more of the 39-Hz bottom plate contribution is present. Shortening the downcomer length further increases the 39-Hz amplitude since the time of arrival of the reflected pressure occurs earlier in the response history. These effects are listed in the last three rows of Table 6.4. The frequency components of the forcing functions by themselves and the frequency components of just their acoustic reflections are shown in the first two rows. The frequency components are listed largest to smallest in terms of Fourier amplitude from left to right. Because the PELE-IC calculations were run to only 274 ms, frequencies less than 4 Hz are absent. Most of the frequency components listed in Table 6.2 are also present in Table 6.4.

## 6.3 COMPRESSIBLE CALCULATIONS

Our final pair of fully flexible calculations used the compressibility option in PELE-IC to determine the effects of water compressibility on the fundamental fluid-structure frequency. Steam injection into the wetwell and partial entrainment in the water is believed to reduce the fluid sound speed substantially. We ran two cases, one with the sound speed of pure liquid water c = 1480 m/s and another calculation with half this sound speed. Figure 35 shows the Fourier spectra of the bottom pressure from 100-200 ms after the impulse function has ended. For a water sound speed of 1480 m/s the fundamental fluid-structure frequency is essentially unchanged in comparison to the incompressible calculation. However, when the sound speed is halved the fundamental fluid-structure frequency is reduced to 26 Hz. Also a 95-Hz frequency component (Fig. 35a) is reduced to a 72.5-Hz component (Fig. 35b). The 62.5 Hz (Fig. 35a) component associated with the side wall is not present in the second calculation (Fig. 35b). A separate rigid-bottom compressible calculation (c = 740 m/s) showed that the 62-Hz component is reduced to 31 Hz.

These results indicate that steam entrainment may have a considerable effect on the reduction of the fundamental fluid-structure interaction mode. Further verification efforts are underway to enhance our confidence in the compressible calculations.

## 6.4 DISCUSSION AND CONCLUSIONS

We have associated various GE4T frequencies with the vibration of either the bottom plate or the cylinder walls. The bottom plate frequency of 42 Hz reduces to about 39 Hz due to interactions of the base plate edges with the side wall. Similarly the 57- and 68-Hz frequency components associated with the side wall appear as a single 63-Hz component due to interactions with the end plate. The beat frequency of approximately 5 Hz is indiscernible for the fully flexible PELE-IC calculations. We have also shown that the effect of wall ring stiffeners is to enhance the 39-Hz fundamental fluid-structure frequency component that is associated with the bottom plate.

We find that the WPPSS forcing function also enhances the 39-Hz frequency component. We have demonstrated that the Fourier amplitude-frequency envelope is strongly affected by the downcomer vent length. Shorter downcomers, as in

the actual Mark II configuration, produce higher Fourier amplitudes for the fundamental fluid-structure 39-Hz frequency component.

The effect of the fluid-structure interaction for the GE4T tank can be seen by the reduction of the frequency of the dry GE4T cylinder from about 800 Hz to 63 Hz and the frequency of the dry bottom plate from about 190 to 39 Hz. This reduction in frequency has been demonstrated using an incompressible representation of the wetwell liquid. Liquid (wetwell) compressibility effects introduced through entrainment of noncondensables have a potential for significant reduction of the effective liquid wave speed. Such compressibility effects can reduce the computed incompressible fluid-structure frequencies.

Two primary system characteristics appear important in achieving a match between experimental and computed Fourier spectra for GE4T bottom center pressures:

1. Liquid compressibility effects decreased the calculated primary fluid-structure frequency downward from 39 Hz computed on the basis of an incompressible wetwell liquid to 26 Hz when the water sound speed was halved.

2. The temporal shape of the specified pressure-history at the downcomer exit as well as the duration of this source are important in the excitation of the fluid-structure frequency components when downcomer vent acoustics are included. (a) For the 29-m GE4T vent length, the triangular pressure pulse duration of 50 ms has the effect of exciting the 13.2-Hz frequency (second-vent acoustic mode). For a 25-ms pressure pulse, the 21-Hz frequency (third-vent acoustic mode) has the greatest Fourier amplitude; this frequency is closer to the natural frequency of the fluid-structure system. (b) At half the total GE4T vent length (prototypical of Mark II), the 50-ms pressure pulse duration has a predominant 25.5-Hz content which approaches the natural frequency of the GE4T system.

The GE4T system is sensitive to downcomer vent acoustic effects and to the prescribed vent exit pressure-forcing functions. The reason for this sensitivity is that the reflected acoustic pressure pulse traversing the downcomer has a strong frequency component only slightly below the dominant fluid-structure natural frequency of the GE4T system. Shortening the GE4T downcomer to a prototypical Mark II length and decreasing the 50-to-55-ms duration of the pressure source will produce a near resonant condition in the 20-to-30-Hz range when wetwell liquid compressibility effects are included.

Because of the system sensitivity to this resonant or potentially near resonant condition, it may be concluded that the envelope of experimental response spectra obtained from GE4T tests is heavily influenced by the particular GE4T system characteristics--downcomer length, bottom plate thickness and radius, entrained noncondensables, and all other Mark II nonscaleable parameters. Therefore, the use of such an enveloped response spectra cannot be considered conservative unless near prototypical test configurations and conditions were obtained. Such prototypical conditions were not established for the GE4T apparatus.

Further work on the Mark II (GE4T) is needed. It is obvious from the above discussion that we need to reassess the data obtained from the GE4T or a similar apparatus using the shorter, more prototypical downcomer. Just as important, however, is the need to eliminate the use of an artificially prescribed pressure history. Such a nonphysical temporal prescription provides a net vent forcing function whose Fourier spectra can be as arbitrarily close or remote as desired to the physically derivable dominant spectra of the fluid-structure system. Instead, further investigation of generic, mechanistically derived source function signatures is recommended. This work should reflect the thermal-hydraulics associated with the steam bubble overexpansion and collapse as they relate to the stable and unstable events.

TABLE 6.1 Geometry and material properties of ARAP aluminum tank.

| | Experiment | Calculation |
|---|---|---|
| Geometry | | |
| Tank height (H), cm | 92.7 | 92.3 |
| Water depth ($H_w$), cm | 90.0 | 92.3 |
| Piston height, cm | 87.0 | 92.3 |
| Tank inside diameter (2R), cm | 17.78 | 17.78 |
| Side wall thickness (h), cm | 0.318 | 0.318 |
| Steel tank bottom thickness, cm | 3.20 | 4.61[a] |
| h/R | 0.036 | 0.036 |
| H/R | 10.4 | 10.4 |
| Material properties | | |
| Poisson's ratio[b] | 0.29 | 0.29 |
| Mass density,[b] $Kg/m^3$ | 2700.0 | 2700.0 |
| Young's modulus,[b] GPa | 68.95 | 68.95 |
| Water temperature, $^oC$ | 20-22 | - |

[a]Bottom plate thickness scaled (see text).

[b]ASTM 6061-T6 aluminum.

TABLE 6.2 Geometry and material properties of GE4T steel tank.

| | GE4T experiment | Calculation |
|---|---|---|
| Geometry | | |
| Tank height (H), cm | 1600 | 1584.8 |
| Water depth ($H_w$), cm | 609.6 - 701.4 | 609.6 |
| Downcomer submergence, cm | 274 - 411.5 | 359.8 |
| Tank inside diameter (2R), cm | 213.4 | 213.4 |
| Sidewall thickness (h), cm | 1.59 | 1.59 |
| End plate thicknesses, cm | 10.16 | 10.16 |
| Downcomer diameter, cm | 50.8 and 61.0 | 56.0 |
| Vent length, cm | 2926 | 2865 and 1432[a] |
| Ullage pressure, kPa | 100 - 275 | 275 |
| h/R | 0.015 | 0.015 |
| H/R | 14.9 | 14.8 |
| $H_w/H$ | 0.38 - 0.44 | 0.38 |
| Material Properties | | |
| Poisson's ratio | ~0.29 | 0.29 |
| Mass density, $Kg/m^3$ | ~7.86 | 7.86 |
| Young's modulus, GPa | ~206 | 206 |
| Water temperature, $^oC$ | 21 - 65 | - |

[a]The actual Mark II vent length is approximately 1220 cm.

TABLE 6.3 GE4T fluid-structure frequencies[a] from Fourier transform of pressure histories.

| | | | | |
|---|---|---|---|---|
| Calculation A: | No axial motion allowed at bottom plate | | | |
| bottom | 67.6 | 56.6 | 14.2[b] | 24.2[b] |
| side wall | 67.6 | 57.2 | 14.2[b] | 24.2[b] |
| Calculation B: | No radial motion allowed on cylinder wall | | | |
| bottom | 41.8 | 15.4[b] | 26.7[b] | 41.8 |
| side wall | 42.4 | 27.6 | 16.3[b] | 57.2 |

[a]Frequencies (Hz) associated with amplitudes are progressively listed from left to right. Those having the largest amplitudes appear on the left with those having the smallest on the right.

[b]See text.

TABLE 6.4 GE4T frequency components Fourier transform of pressure histories.

| Pulse description | | Frequencies[a], Hz | | | | |
|---|---|---|---|---|---|---|
| WPPSS input pulse alone | | 13.5 | 53.4 | 38.7 | - | - |
| Reflected WPPSS pulse alone (vent acoustics) | | 12.5 | 20.7 | 37.2 | 29.0 | 3.9 |
| PELE-IC bottom pressure for WPPSS pulse (no reflection) | (100-200 ms) | 38.4 | 62.6 | 15.2 | 25.5 | 52.6 |
| PELE-IC bottom pressure for WPPSS pulse with its acoustic reflection (L = 28.6 m) | (100-273 ms) | 39.1 | 25.4 | 18.7 | 53.0 | 11.5 |
| | (0-273 ms) | 37.6 | 25.8 | 10.5 | 63.0 | 18.0 |
| PELE-IC bottom pressure for WPPSS pulse with its acoustic reflection (L = 14.3 cm) | (0-273 ms) | 39.8 | 45.7 | 31.5 | 8.2 | 64.0 |

[a]Frequencies associated with amplitudes are progressively listed from left to right. Those having the largest amplitudes appear on the left with those having the smallest on the right.

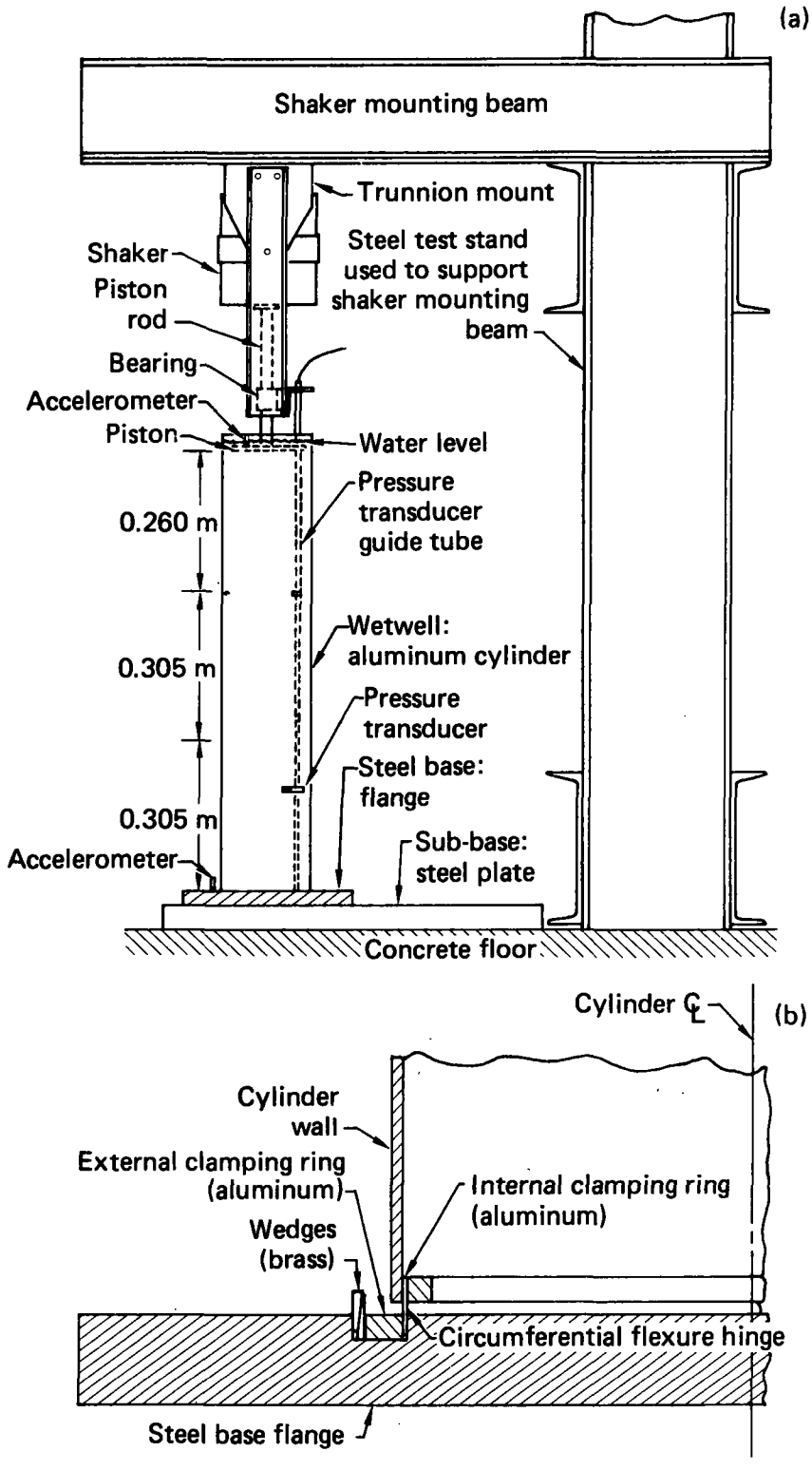


FIG. 21. ARAP test apparatus. (a) Water-filled aluminum cylinder and shaker. (b) Detail of tank base supports.

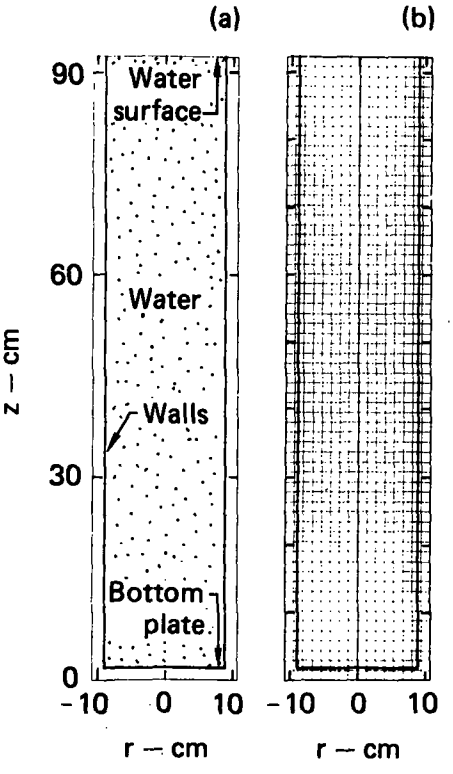


FIG. 22. ARAP cylinder calculated geometry. (a) Cylinder walls and bottom. (b) Cylindrical shell superimposed on rectangular mesh with 504 Eulerian cells and 70 Lagrangian shell elements.

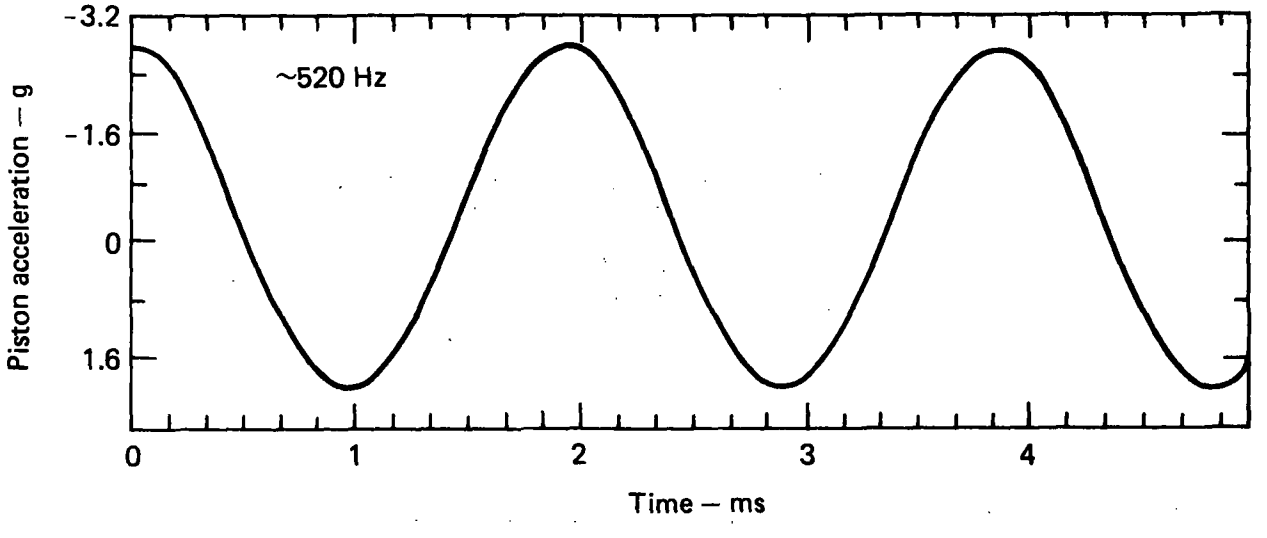


FIG. 23. ARAP cylinder experimental acceleration-time history at top water surface.

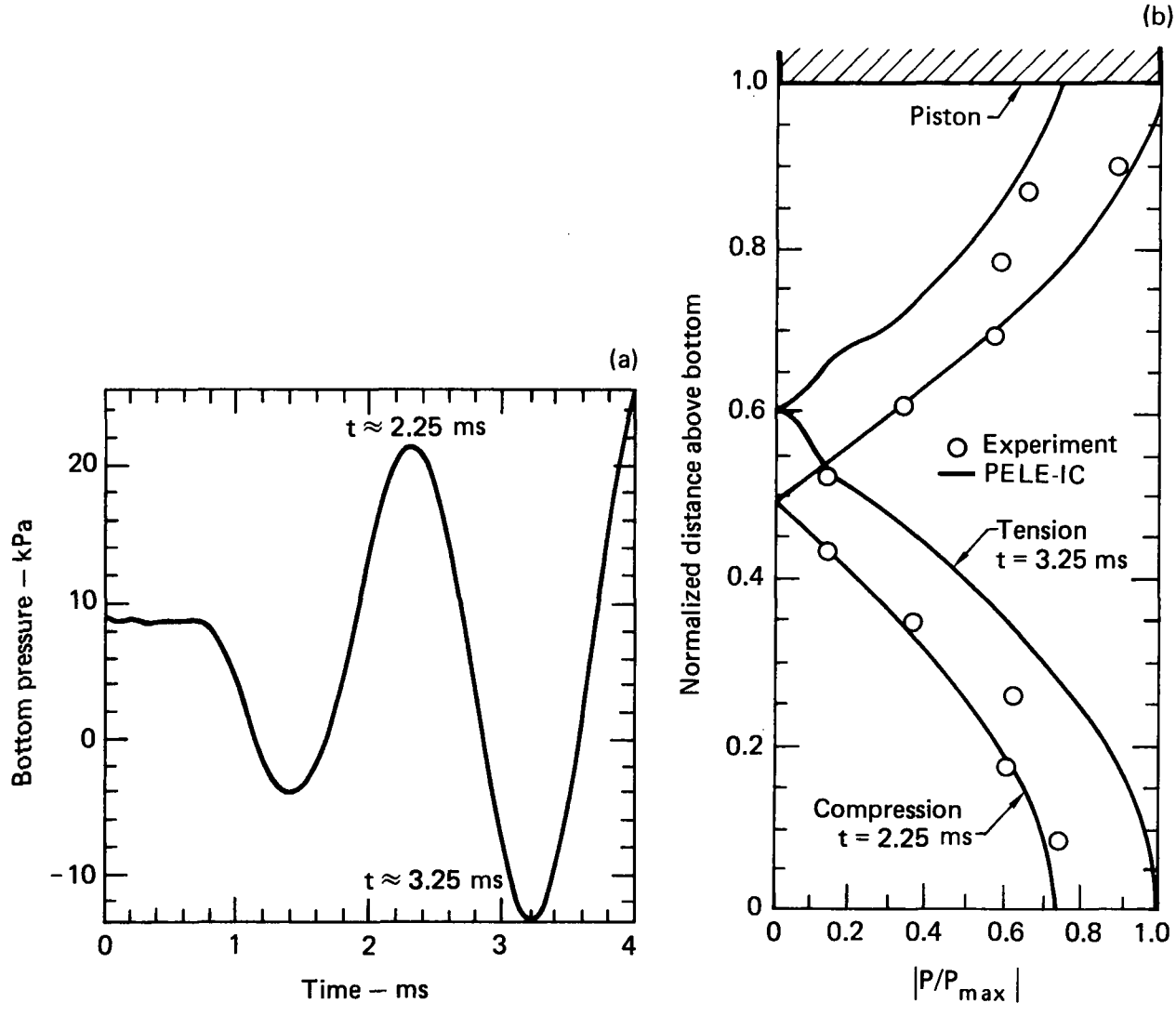


FIG. 24. ARAP pressure plots (f ≈ 520 Hz). (a) Calculated time history at bottom center of tank. (b) Mode shape comparison along vertical column 4.13 cm from cylinder axis.

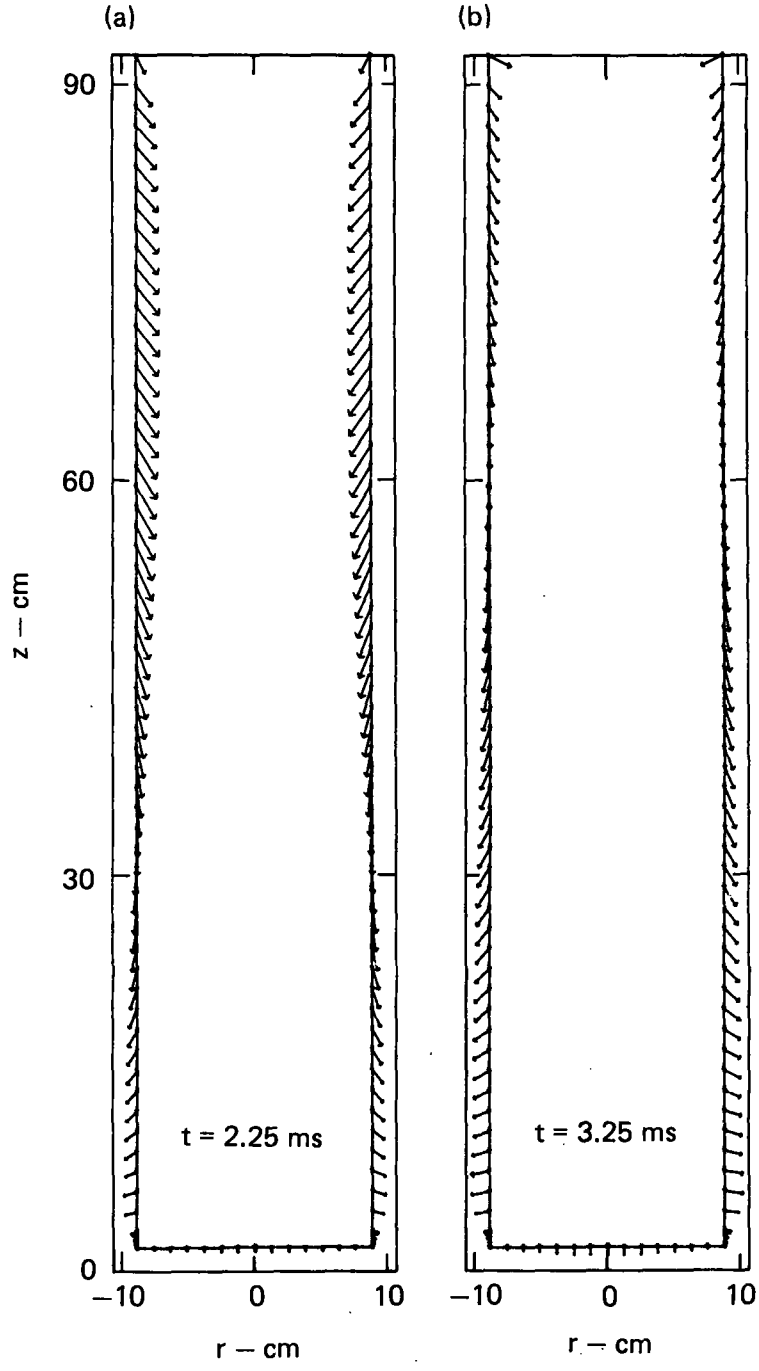


FIG. 25. ARAP cylinder velocity vector plots showing second axisymmetric (side wall) mode. (a) Peak compression. (b) Peak tension.

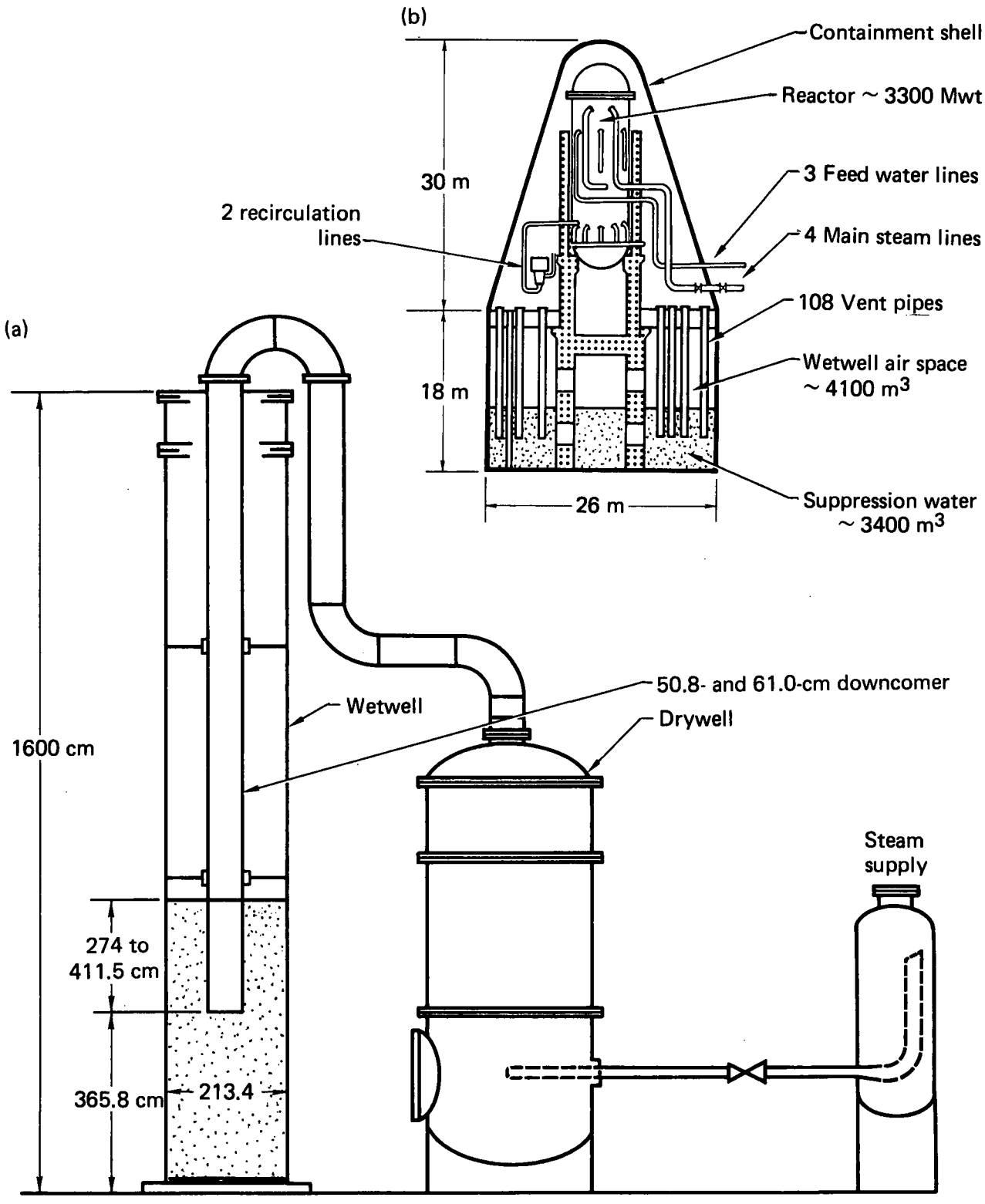


FIG. 26. GE Mark II facilities. (a) Single vent GE4T wetwell and drywell. (b) Cross section of actual multivent reactor wetwell and drywell.

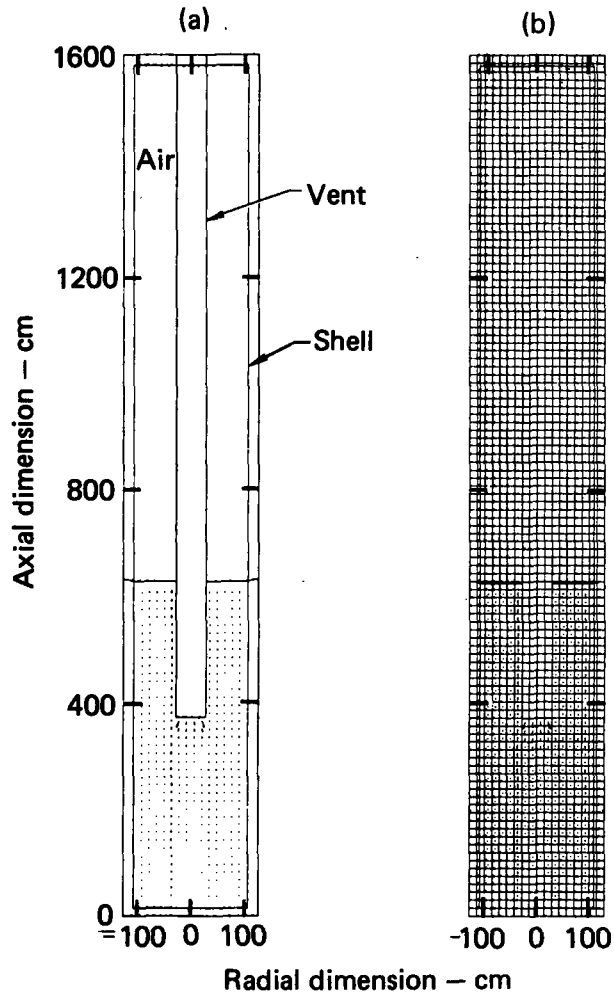


FIG. 27. GE4T calculated geometry with 972 Eulerian cells and 130 shell elements. (a) Tank shell, downcomer, and water. (b) Overlaid rectangular Eulerian grid.

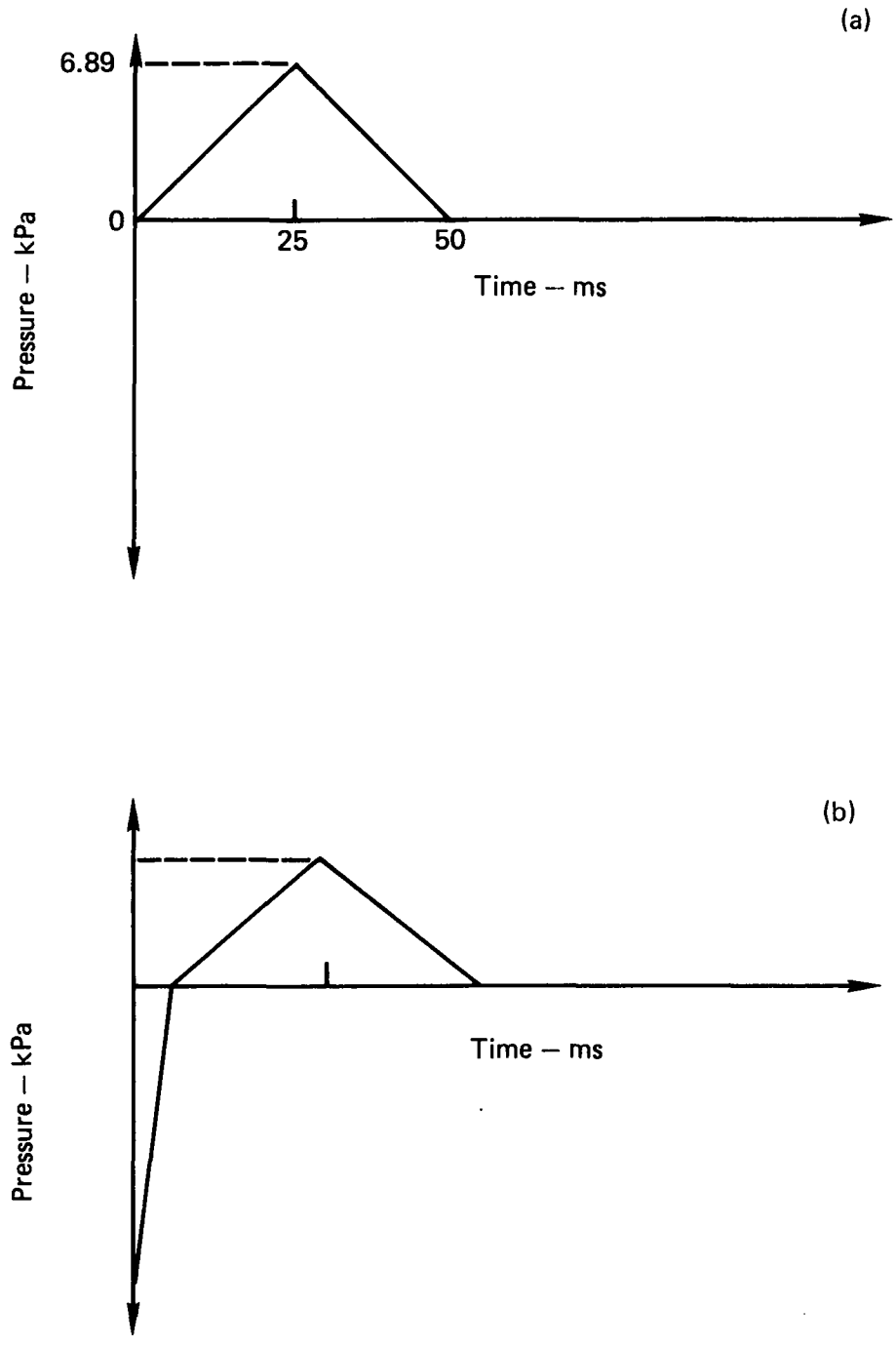


FIG. 28. Chugging load defined at downcomer exit for GE4T. (a) Triangular pressure pulse. (b) WPPSS pressure pulse.

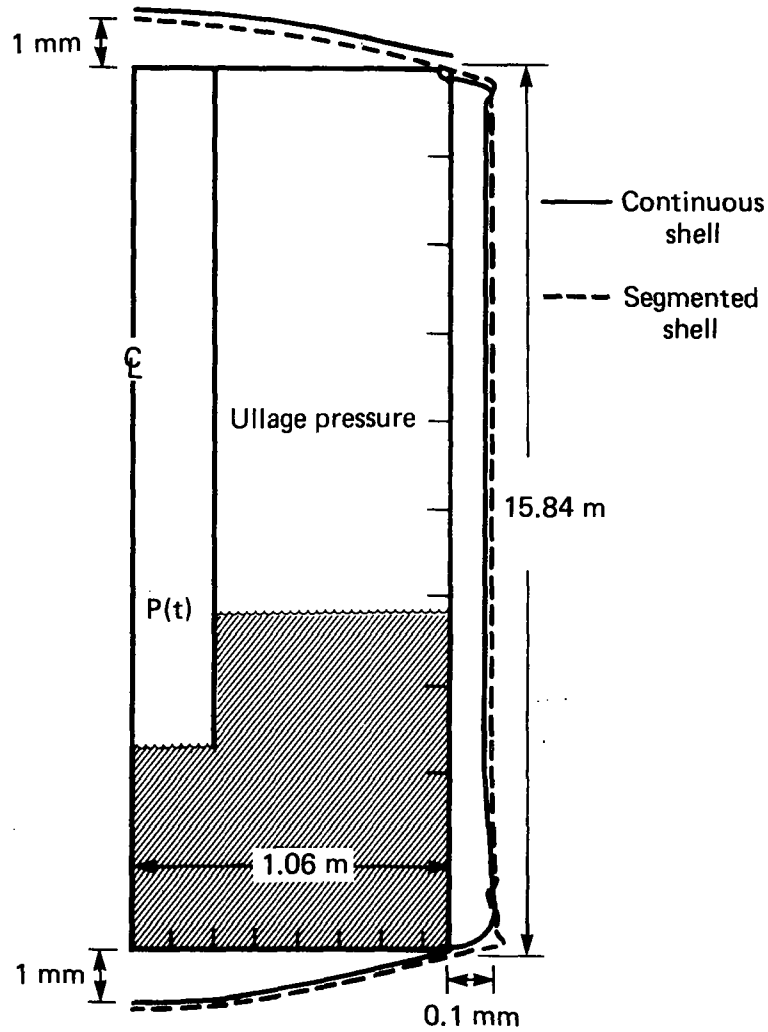


FIG. 29. GE4T calculated static deflection. Note that the radial deflection scale is 1/10 the axial deflection scale.

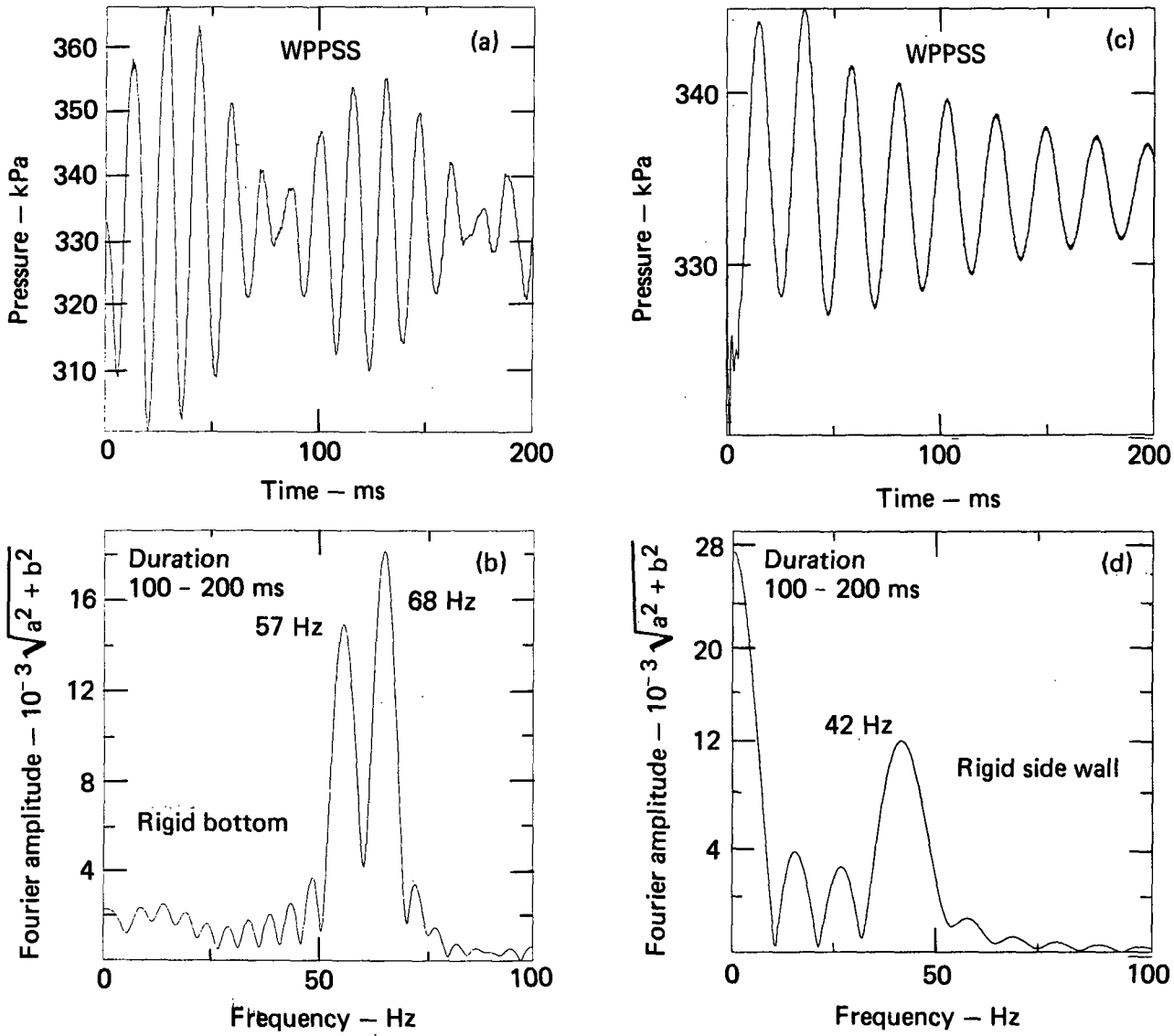


FIG. 30. GE4T fluid-structure frequencies for rigid bottom (left) and rigid side wall (right) calculations. (a) and (c) Bottom pressure from PELE-IC. (b) and (d) Fourier transform of bottom pressure. Note the approximate 5-Hz beat frequency in (a).

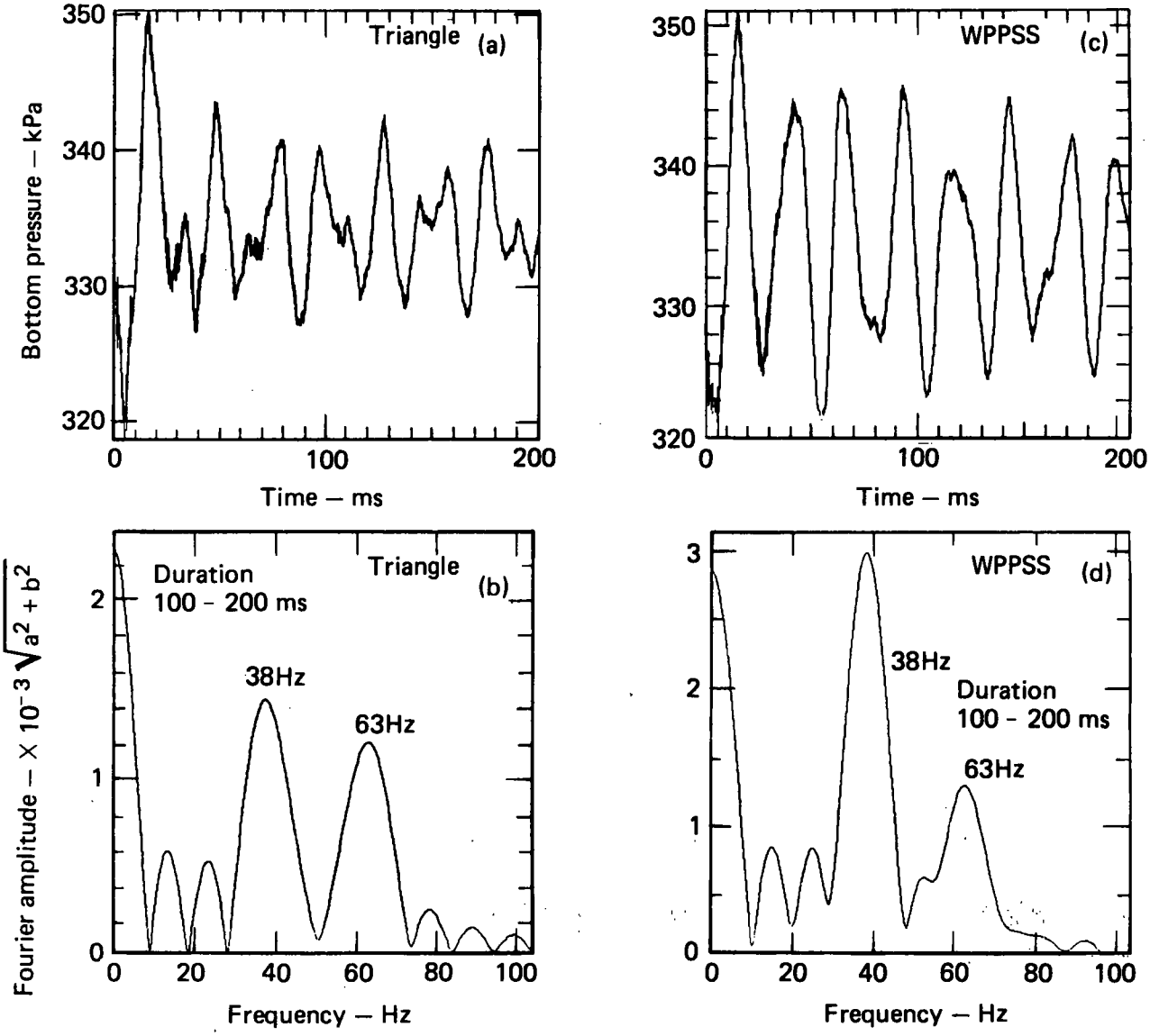


FIG. 31. GE4T fluid-structural frequencies calculated by PELE-IC for two input pulses, triangular (left) and WPPSS (right). (a) and (c) Bottom pressure at half radius. (b) and (d) Fourier transform of bottom pressure.

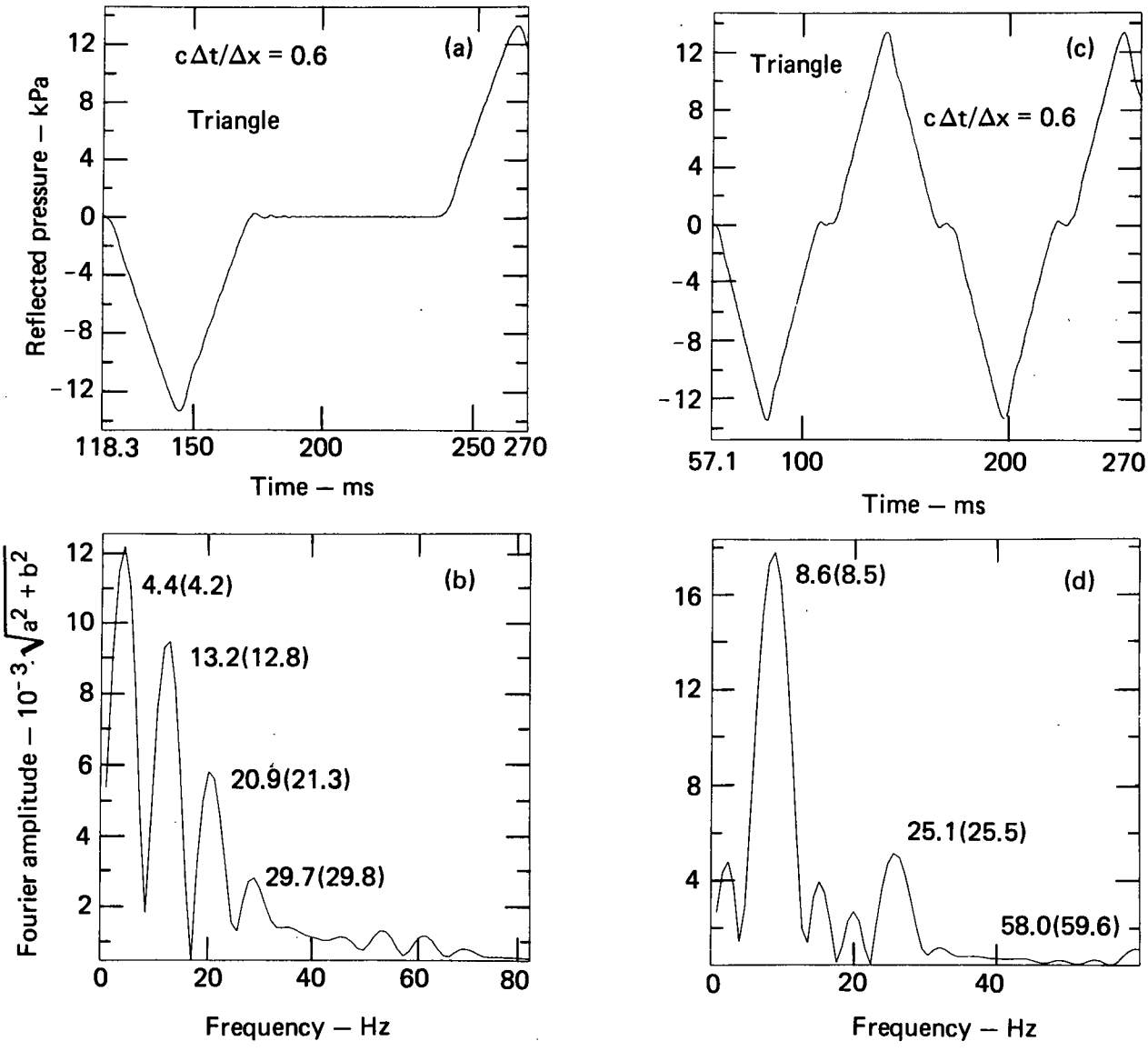


FIG. 32. Vent acoustics calculations using triangular pulse for downcomer pipes of length 28.6 m (left) and 14.3 m (right). (a) and (c) Reflected pressure at end of vent pipe, beginning with the first reflection. (b) and (d) Fourier transform of reflected triangular pulse.

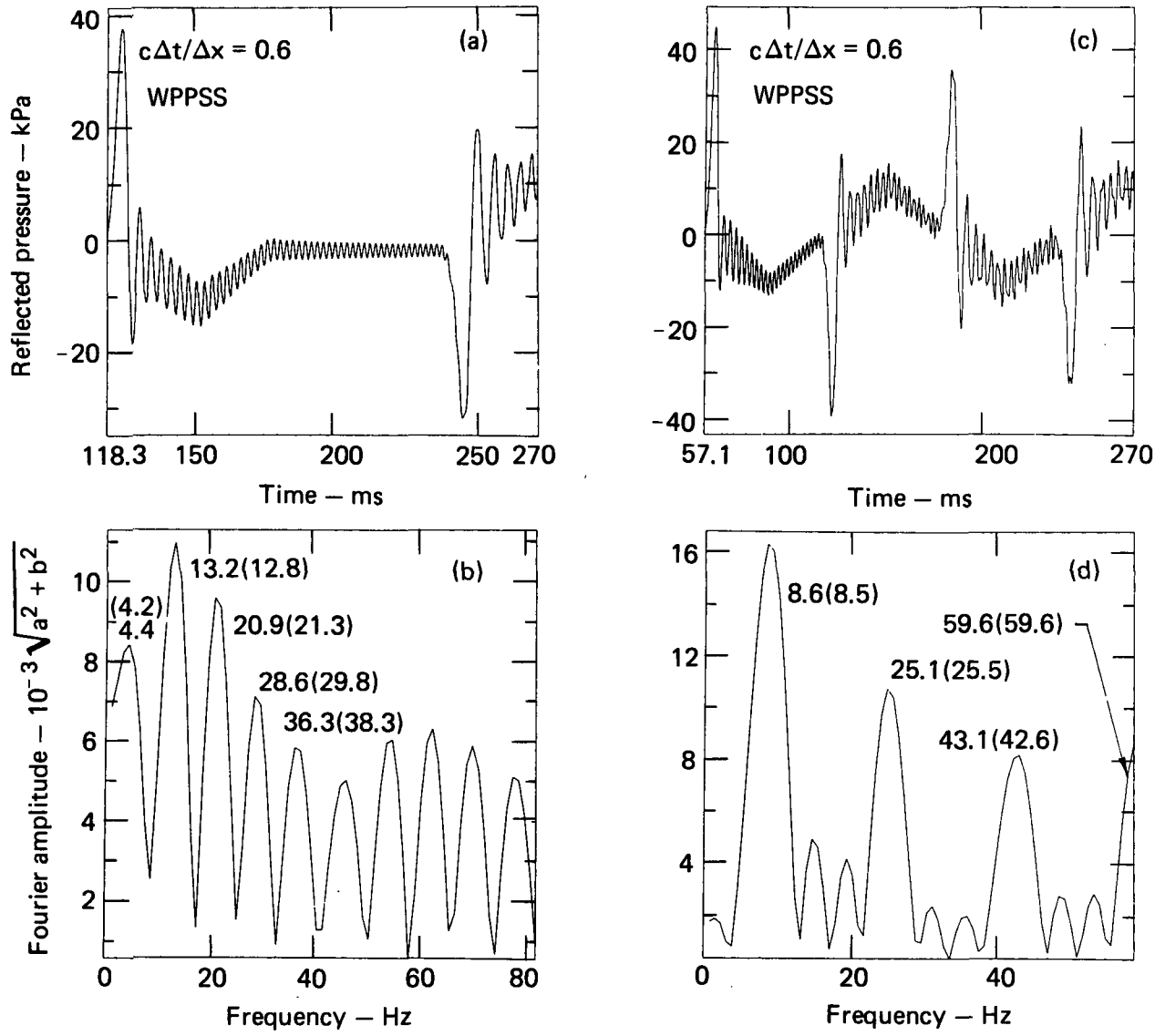


FIG. 33. Vent acoustic calculations using WPPSS pulse for downcomer pipes of length 28.6 m (left) and 14.3 m (right). (a) and (c) Reflected pressure at end of vent pipe, beginning with first reflection. (b) and (d) Fourier transform of reflected WPPSS pulse.

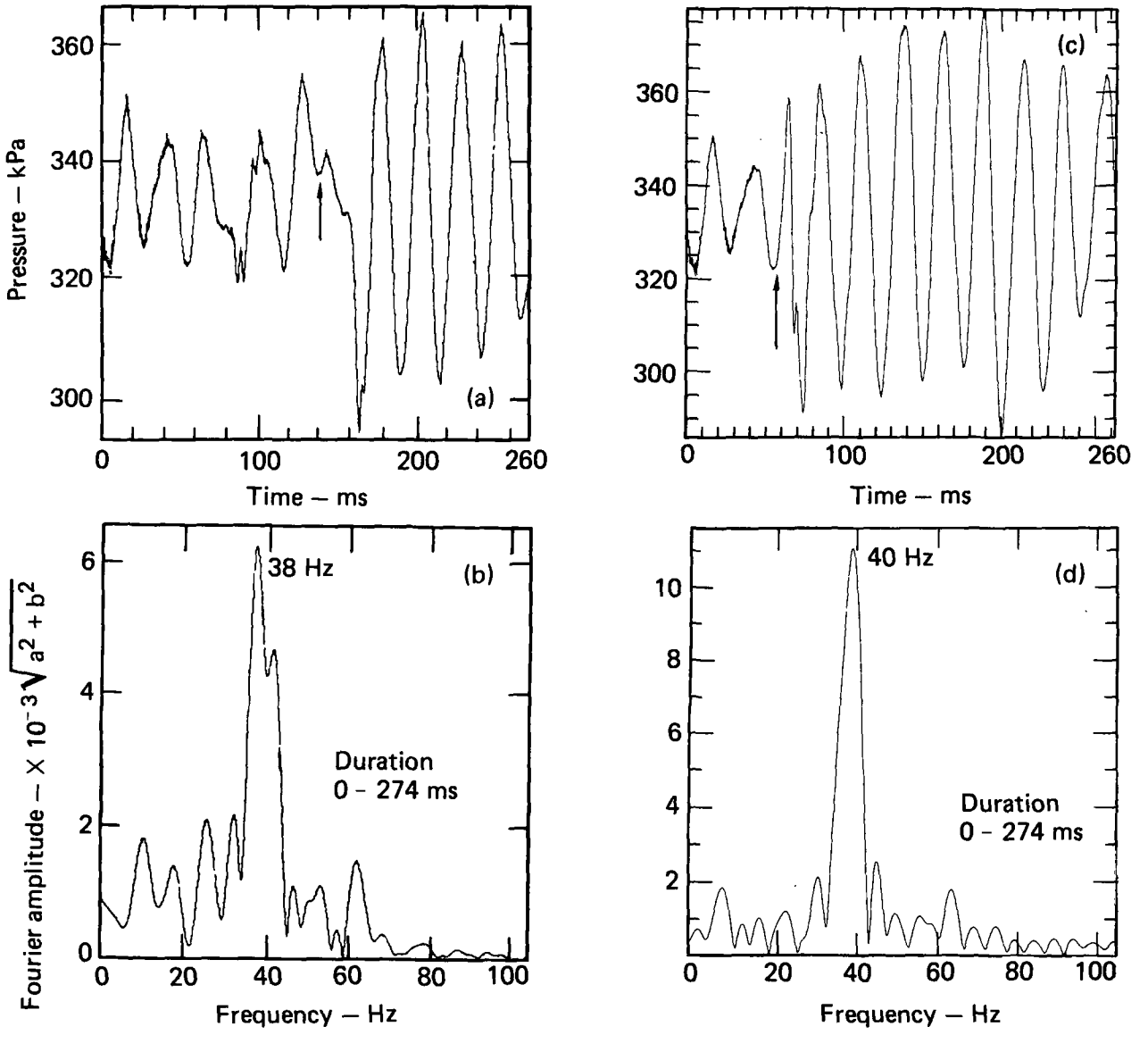


FIG. 34. GE4T calculation using WPPSS pulse and its acoustic reflection as driving pressure for two pipe lengths, 28.6 m (left) and 14.3 m (right). (a) and (b) Bottom pressure at half radius; arrows discussed in text. (c) and (d) Fourier transform of entire bottom pressure history.

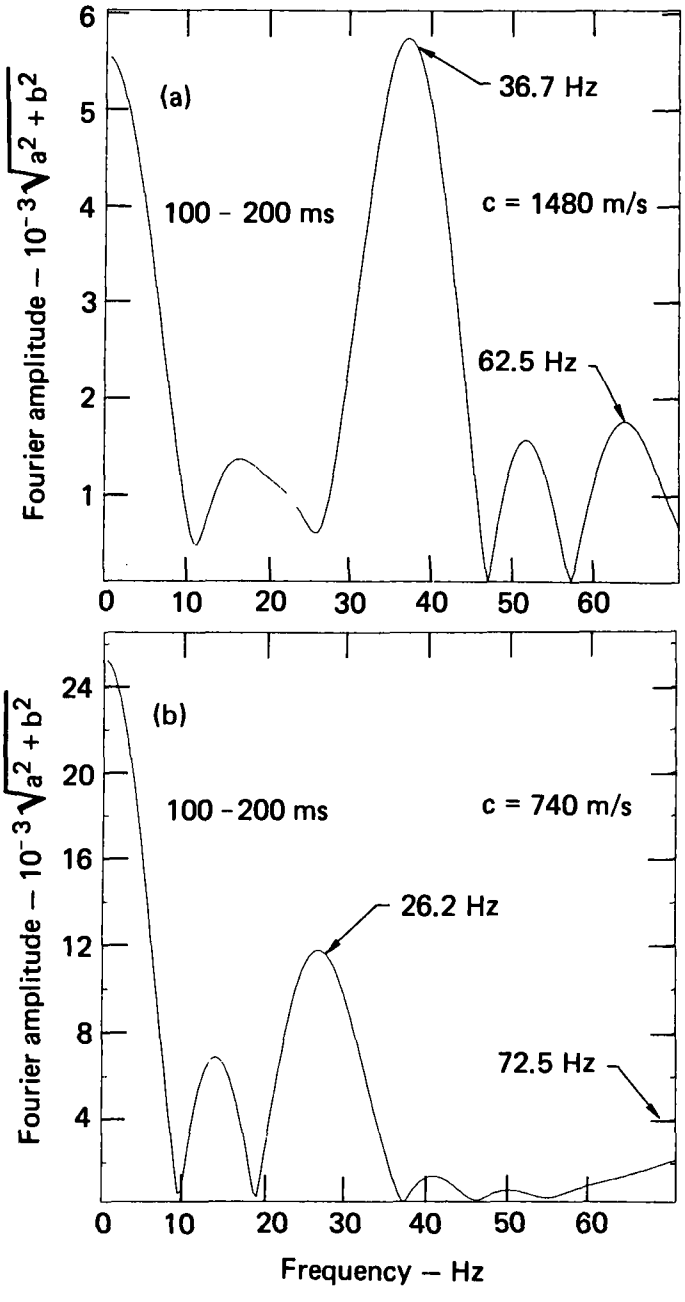


FIG. 35. GE4T compressibility effects without vent acoustics for WPPSS pulse. Fourier transform of bottom pressure. (a) Normal water, c = 1480 m/s. (b) Steam injected water, c = 740 m/s.

## REFERENCES


1. E. Y. Gong, E. E. Alexander, W. M. McMaster and D. F. Quiñones, PELE-IC Test Problems, Lawrence Livermore Laboratory, Livermore, Calif., UCRL 52835 (1979).
2. F. N. Browder, "Evolution and Current Status of the BWR Containment System," Nuclear Safety 15 (2) March-April 1974.
3. W. M. McMaster, D. M. Norris, Jr., G. L. Goudreau, D. F. Quiñones, E. Y. Gong, B. Moran, and N. A. Macken, Coupled Fluid-Structure Method for Pressure Suppression Analysis, Lawrence Livermore Laboratory, Livermore, Calif., NUREG/CR-0607 (1979).
4. C. W. Hirt, B. D. Nichols, and N. C. Romero, SOLA--A Numerical Solution Algorithm for Transient Fluid, Los Alamos Scientific Laboratory, Los Alamos, New Mexico, LA-5852 (1975).
5. J. O. Hallquist, NIKE2D--An Implicit, Finite Deformation, Finite Element Code for Analyzing the Static and Dynamic Response of Two-Dimensional Solids, Lawrence Livermore Laboratory, Livermore, Calif., UCRL-52678 (1979).
6. E. K. Collins and W. Lai, Final Air Test Results for the 1/5-Scale Mark I Boiling Water Reactor Pressure Vessel Suppression Experiment, Lawrence Livermore Laboratory, Livermore, Calif., UCRL-52371 (1977).
7. G. L. Goudreau, A Computer Module for One Step Dynamic Response of an Axisymmetric or Plane Linear Elastic Thin Shell, Lawrence Livermore Laboratory, Livermore, Calif., UCID-17730 (1978).
8. W. H. McMaster and E. Y. Gong, User's Manual for PELE-IC: A Computer Code for Eulerian Hydrodynamics, Lawrence Livermore Laboratory, Livermore, Calif., UCRL-52609 (1979).
9. H. Kraus, Thin Elastic Shells (John Wiley & Sons, Inc., New York 1967).
10. T. J. R. Hughes and R. L. Taylor, in Smirt Proc., M2/1 (1977).
11. G. L. Goudreau and R. L. Taylor, Computational Methods in Applied Mechanics and Engineering 2 (1), 69 (1973).
12. O. C. Zienkiewicz, J. Bayer, K. Morgan, and E. Omate, Int. J. Numerical Methods in Eng. 11 (10), 1545 (1977).

13. J. K. Vennard, Elementary Fluid Mechanics (John Wiley & Sons, New York, 1954), 3rd ed., pp. 110-111 and 301-305.

14. G. Goertzel, Mathematical Methods for Digital Computers, Ralston and Wilf, Eds. (John Wiley & Sons, New York 1967).

15. A. E. H. Love, A Treatise on the Mathematical Theory of Elasticity (Dover Publications, New York, 1944), 4th ed., p. 513.

16. E. A. Schroeder and M. S. Marcus, in Proc. 46th Shock and Vibration Symposium, San Diego, Calif., (1975).

17. R. E. Nickell and R. S. Dunham, Numerical Methods for Acoustic Fluid/Structure Interaction, Final Report to the Electric Power Research Institute by Pacifica Technology, Palo Alto, Calif., Contract No. RP965-4 (1979).

18. C. W. Hirt, "Heuristic Stability Theory for Finite-Difference Equations," Journal of Comp. Physics 2, 339 (1968).

19. R. E. Nickell and J. J. Carey, "Interaction of Structural Mechanics and Thermal-Hydraulic-Neutronics Codes," in Proc. 5th Int. Conf. on Structural Mechanics in Reactor Technology (Post-Conference Seminar on Fluid-Structure Interaction, Berlin, 1979).

20. Y. Javadi and P. W. Huber, Tests of Fluid-Structure Interactions in a Small Scale "Pool Swell" System, Progress Report, Fluid Mechanics Laboratory Department of Mechanical Engineering, Massachusetts Institute of Technology, Cambridge, Mass. (1979).

21. J. K. Vennard, Elementary Fluid Mechanics (John Wiley, New York, 1954), 3rd ed., pp. 110-111 and 301-305.

22. S. Timoshenko and S. Woinowsky-Krieger, Theory of Plates and Shells (Mcgraw-Hill Book Company, New York, 1959), 2nd ed., pp. 404-408.

23. S. W. Kang, "Analytic Studies of Vent Clearing and Jet-Slug Dynamics," in Reactor Containment Analysis for BWR Suppression Systems, L. L. Edwards, Ed., Lawrence Livermore Laboratory, Livermore, Calif., UCRL-50045-77-2 (1977).

24. R. G. Altes, J. H. Pitts, R. F. Ingrahan, and E. K. Collins, Mark I 1/5 Scale Boiling Water Reactor Pressure Suppression Experiment Facility Report, Lawrence Livermore Laboratory, Livermore, Calif., UCRL-52340 (1977).

25. L. L. Edwards, Computer Simulations of a 1/5-Scale Experiment of a Mark I Boiling Water Reactor Pressure-Suppression System Under Hypothetical L.O.C.A. Conditions, Lawrence Livermore Laboratory, Livermore, Calif., UCID-17782 (1978).

26. E. W. McCauley, G. S. Holman, E. W. Carr, W. Lai, and J. E. Mellor, Extended Analysis of Data from the 1/5-Scale Mark I Boiling Water Reactor Pressure Suppression Experiments, Lawrence Livermore Laboratory, Livermore, Calif., UCRL-52707 (1979).

27. M. J. Normandia, R. S. Snedeker, and A. J. Bilanin, Experimental Investigation of Fluid-Structural Interaction in Cylindrical Containers, Electric Power Research Institute, Palo Alto, Calif., to be published (1980).

28. W. A. Grafton, T. R. McIntyre, and M. A. Ross, Mark II Pressure Suppression Test Program Phase II and III Tests, General Electric Company, San Jose, Calif., Proprietary Report NEDE-13468, Class III (October 1976).

29. Mark II Containment Supporting Program Summary of 4T Fluid-Structure Interaction Studies, Anamet Laboratories, San Carlos, Calif., General Electric Company Proprietary Report NEDE-23710, Class III (April 1978).

30. M. M. Ettouney, Chugging Loads-Improved Definition and Application Methodology to Mark II Containments, Burns and Roe, Inc., Oradell, New Jersey, proprietary report (June 1979).

31. Summary of 4T Fluid-Structure Intersection Studies, Anamet Laboratories, San Carlos, Calif., General Electric Nonproprietary Report NEDO-23710 78NED158 Class I (September 1978).

# APPENDIX A

## A.1.0 DESCRIPTION OF CONDENSATION EVENTS

### A.1.1 STABLE AND UNSTABLE CONDENSATION LOADS

The oscillatory pressure-time histories that are observed at the wall of a partially-water-filled tank subjected to stable steam condensation loads have been explained by a number of investigators.[1-3] At a sufficiently high steam mass flux from the drywell into the downcomer, the dynamics can be described by the thermal-hydrodynamic exchange of energy between inertially-driven steam bubble expansion into a cool, incompressible water pool and the surface-area-driven condensation of this steam bubble. Figures A.1a and A.1b show the individual characteristics of these two processes, while Fig. A.1c indicates their interaction on a temporal scale. This model results in relatively small pressure oscillations and fluid displacements in the water adjacent to the steam bubble.

As the steam mass flux into the downcomer is reduced, the process becomes unstable. The precise mechanics of unstable condensation are not known for certain; however, the wall pressure traces from chugging events have been correlated with a variety of assumed downcomer pressure traces in order to arrive at a reasonable judgment. The following summary of the possible steps involved represents one such judgmental estimate:

1. We begin the event with the downcomer and wetwell water surfaces in equilibrium and with the steam mass flux at the entrance to the downcomer exactly balanced by condensation along the downcomer walls and on the downcomer water surface; this equilibrium mass flux is less than the chugging mass flux, and significantly less than stable condensation mass fluxes.

2. The steam mass flux at the entrance to the downcomer is increased to levels associated with chugging, and the steam begins to push the water from the downcomer and form a steam bubble outside the downcomer exit plane; because of the excess pressure from the chugging mass flux, the water near the end of the downcomer is accelerated to some velocity that depends upon the ratio of downcomer area to wetted pool area and other factors. One should

assume that these velocities are smaller than those generated by the higher steam mass fluxes associated with condensation oscillation.

3. The steam bubble is able to overexpand because of the inertia of the retreating fluid, until it reaches a critical size such that surface heat transfer and condensation begin to dominate. At this point, unlike the condensation oscillation event, the dynamic head is reversed, causing the bubble to collapse. A number of possible physical mechanisms could be contributing to this reversal of both velocity and pressure gradient. The pool temperature could be increasing (thus decreasing the surface heat transfer rate) while the steam mass flow is decreasing, leading to more favorable conditions for bubble over-expansion. Another possibility is that, during condensation oscillation, the higher steam mass flux maintains a sufficiently high bubble pressure so that flow reversal in the adjacent water does not coincide with a reversal in pressure gradient. A third possibility is that a second-order effect, such as surface tension and/or acceleration of the bubble toward the free surface of the pool, could be dominating the physics at neutral equilibrium between surface heat transfer and adjacent water inertia. Regardless of the mechanism, the collapse of the bubble produces a sharp local impulse. This impulse appears as a negative pressure (relative to initial pressure) to the water lateral to and below the bubble, but the impulse would do work on any fluid volume above it, driving some portion of water up the downcomer.

4. When the water volume driven up the downcomer reaches its highest point, the flow reverses again (gravity head is now the dominant term) and the fluid drops almost to the equilibrium position, creating a small positive pressure on fluid particles at the exit plane of the downcomer. Visual examination of chugs would indicate, however, that the downcomer water level returns to equilibrium in an oscillatory fashion, indicating that acoustic waves in the downcomer are interacting with the gravity head dynamics.

This four-step scenario agrees qualitatively with pressure-time histories that have been proposed by a number of investigators for application as forcing functions to the pool, with the pressure being applied to the water surface at the exit plane of a precleared downcomer. These proposed pressure traces tend to be either positive triangular pulses or a combination of a negative pressure spike followed by the positive triangular pulse. In Sec. 6.2 of this report we investigated these pulses for a particular

application to assess their capability in replacing the complex thermal-hydrodynamics of steam bubble expansion and collapse.

## REFERENCES


1. G. B. Andeen, and J. S. Marks, Analysis and Testing of Steam Chugging in Pressure Systems, Electric Power Research Institute, Menlo Park, Calif., Report NP-908 (1978).
2. L. W. Florschuetz, and B. T. Chao, "On the Mechanism of Vapor Bubble Collapse," Journal of Heat Transfer 87 (2), 209 (1965).
3. J. S. Marks, and G. B. Andeen, "Condensation Oscillation" in 18th National Heat Transfer Conference (A.S.M.E./A.I.Ch.E. San Diego, Calif., 1979).

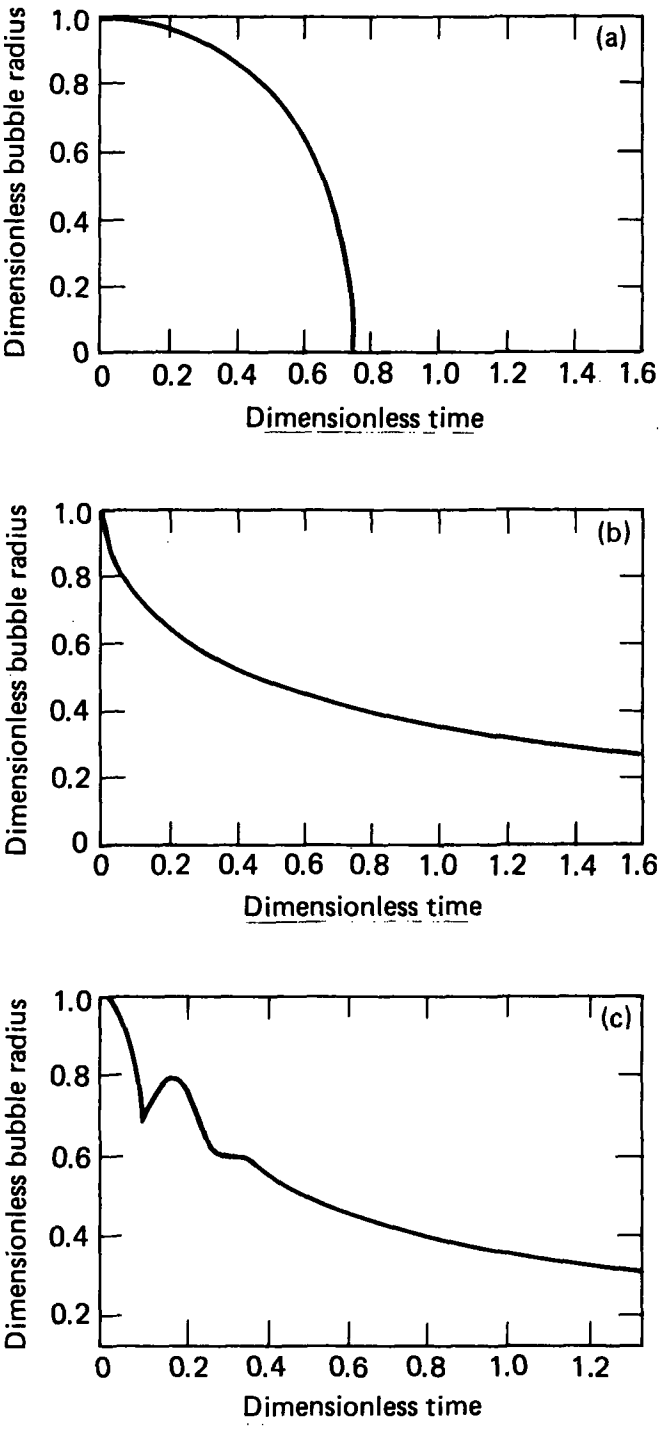


FIG. A.1. Bubble collapse mechanisms. (a) Inertia controlled. (b) Heat transfer controlled collapse. (c) Both considerations included.[1,2]

# APPENDIX B

## B.1.0 BUBBLE PRESSURE MODEL FOR PELE-IC WITHOUT CONDENSATION

### B.1.1 INTRODUCTION

The PELE-IC code used to determine fluid-structure interaction problems will accommodate submerged voided regions (e.g., air bubbles) provided that the pressure within the voided regions is specified. When the void is a submerged bubble eminating from the end of the downcomer and is fed by a mass injected from the drywell, the drywell and bubble pressures are not equal. This Appendix formulates a compressible flow model which couples drywell and bubble pressures to PELE-IC calculations of local pool pressure.

Consider the model illustrated in Fig. B.1. The control volume is defined as the downcomer air volume below the orifice plate plus any volume of bubble formed. The pressure (P) and temperature (T) are assumed to be uniform within the control volume at each instant of time. The initial pressure $P_{u_i}$ of the gas is initial ullage pressure, and the gas at that time is assumed at ambient temperature ($T_0$) which is the drywell temperature. The following analysis holds during vent clearing and during subsequent bubble growth.

After the valve between the orifice and drywell is opened at time t = 0 (see Fig. B.1d), the following constraints on the control volume are formulated:

### B.1.2 MASS BALANCE

$$\dot{m} = \frac{d}{dt}(\rho V) \qquad \text{with} \qquad V = V_0 \qquad \text{at} \qquad t = 0 \ , \tag{B.1}$$

where the flow rate ($\dot{m}$) is subsequently given across the orifice separating the drywell and the bubble. The frictional pressure drop through the downcomer pipe is negligible.

B.1.3 ENERGY BALANCE

$$\frac{d}{dt}(\rho VT) = \gamma T_0 \dot{m} - (\gamma - 1)\frac{p}{R}\frac{dV}{dT}, \tag{B.2}$$

where heat transfer has been ignored and ideal gas behavior has been assumed and

$$\rho = \frac{p}{RT} \qquad C_p/C_v = \gamma \qquad C_v = \frac{R}{\gamma - 1}. \tag{B.3}$$

Perform the indicated differentiation of Eq. (B.2) to obtain

$$\rho V \frac{dT}{dt} + \frac{d}{dt}(\rho V) = \gamma T_0 \dot{m} - \frac{(\gamma - 1)}{R} p \frac{dV}{dt}. \tag{B.4}$$

After dividing through by $\rho V$, place Eqs. (B.1) and (B.3) into Eq. (B.4) to obtain

$$\frac{dT}{dt} + \left[\frac{d}{dt}(\ln \rho V) + (\gamma - 1)\frac{d}{dt}(\ln V)\right] T = \gamma T_o \frac{d}{dt}(\ln \rho V). \tag{B.5}$$

Note that Eq. (B.5) is linear in temperature (T) and may be solved accordingly. Let

$$B \equiv \frac{d}{dt}\left[\ln(\rho V)\right] + (\gamma - 1)\frac{d}{dt}(\ln V)$$

and

$$C \equiv \frac{d}{dt}(\ln \rho V).$$

If the solution of Eq. (B.5) is of the form

$$T = u(t) \cdot e^{-\int_0^t B(\tau)\,d\tau}, \tag{B.6}$$

then u(t) must satisfy

$$\frac{du}{dt} = \gamma T_0 C \, e^{+\int_0^t B(\tau)\,d\tau}$$

so that upon integration

$$u = \gamma T_0 \int_0^t C(\tau) \, e^{+\int_0^\tau B(\tau')\,d\tau'} \, d\tau + \text{const} . \tag{B.7}$$

Therefore since $T = T_0$ when $t = 0$, the constant is $T_0$ and the formal solution is by Eqs. (B.6) and (B.7)

$$\frac{T}{T_0} = \left[ 1 + \gamma \int_0^t C(\tau) \, e^{+\int_0^\tau B(\tau')\,d\tau'} \, d\tau \right] e^{-\int_0^t B(\tau)\,d\tau} . \tag{B.8}$$

Now since B has been previously defined, we have

$$\int_0^t B(\tau)\,d\tau = \Big[ \ln(\rho V) + (\gamma - 1) \ln V \Big] \Big|_0^t = \ln\left( \frac{\rho V^\gamma}{\rho_0 \, V_0^\gamma} \right)$$

so that

$$e^{-\int_0^t B(\tau)\,d\tau} = \frac{\rho_0 \, V_0^\gamma}{\rho V^\gamma} .$$

Also,

$$\int_0^t C(\tau)\, e^{+\int_0^\tau B(\tau')\,d\tau'}\, d\tau = \frac{1}{\rho_0 V_0^\gamma} \int_0^t \left[\frac{d}{dt}(\ln \rho V)\right] \cdot \rho V^\gamma \cdot d\tau$$

$$= \frac{1}{\rho_0 V_0^\gamma} \int_0^t V^{(\gamma-1)} \frac{d}{d\tau}(\rho V)\, d\tau \,.$$

But by Eq. (B.1), $\frac{d}{dt}(\rho V) = \dot{m}(p(t))$, so that Eq. (B.8) is

$$\frac{T}{T_0} = \frac{\rho_0 V_0^\gamma}{\rho V^\gamma} \left[1 + \frac{\gamma}{\rho_0 V_0^\gamma} \int_0^t \dot{m}\, V^{(\gamma-1)}\, d\tau\right] .$$

The state equation along with the initial condition requires

$$\frac{\rho_0}{\rho} = \frac{P_{u_i}}{p} \cdot \frac{T}{T_0} .$$

Hence, the result throughout vent clearing and bubble formation is

$$\frac{p}{p_{u_i}} = \left(\frac{V_0}{V(t)}\right)^\gamma \left[1 + \frac{\gamma}{\rho_{u_i} V_0^\gamma} \int_0^t \dot{m}(p, p_d)\, V(\tau)^{\gamma-1}\, d\tau\right], \qquad \text{(B.9)}$$

where

$$\rho_{u_i} = \rho_0 = \frac{P_{u_i}}{RT_0} ,$$

$P_{u_i}$ = initial ullage pressure corresponding to density $\rho_{u_i}$,

$V_0$ = air volume of downcomer at initial pressure $P_{u_i}$,

$\gamma$ = specific heat ratio; $\gamma$ = 1.4 for air,

$\dot{m}$ = flow rate through orifice,

V = current steam volume,

The expressions for the choked and unchoked flows (see Ref. 1) are combined into Eq. (B.9). Equation (B.9) was numerically evaluated in parallel with the PELE-IC calculations. The mass flow is calculated as follows. If the flow is choked, it will choke at the orifice whose flow area is $A_c$. If the flow is unchoked, allowance is made for bi-directional flow; i.e., either drywell to bubble or bubble to drywell.

For

$$\frac{p}{p_d} \leq \left(\frac{2}{\gamma + 1}\right)^{\gamma/(\gamma-1)} \quad , \text{ choked,}$$

$$\dot{m} = C_f C_c \frac{P_d}{\sqrt{T_0}} A_c \sqrt{\frac{g\gamma}{R}\left(\frac{2}{\gamma + 1}\right)^{(\gamma+1)/(\gamma-1)}} \quad . \tag{B.10}$$

For

$$\frac{p}{p_d} \geq \left(\frac{2}{\gamma + 1}\right)^{\gamma/(\gamma-1)} \quad , \text{ unchoked,}$$

$$m = \begin{cases} \dot{m}_A \leq \text{ if } \dfrac{p}{p_d} \quad 1; & \text{"A" denotes flow forward bubble,} \\ \dot{m}_B \geq \text{ if } \dfrac{p}{p_d} \quad 1; & \text{"B" denotes flow away from bubble,} \end{cases}$$

where

$$\dot{m}_A = C_{f_A} C_{c_A} A_c \sqrt{\frac{2g\gamma\, p_d \rho_d \left[\left(\frac{p}{p_d}\right)^{2/\gamma} - \left(\frac{p}{p_d}\right)^{(\gamma+1)/\gamma}\right]}{(\gamma - 1)\left[1 - \left(\frac{p}{p_d}\right)^{2/\gamma} C_{c_A}{}^2 \left(\frac{A_c}{A_d}\right)^2\right]}} \qquad \text{(B.11)}$$

$$\dot{m}_B = C_{f_B} C_{c_B} A_c \sqrt{\frac{2g\gamma\, \frac{p^2}{RT_0}\left[\left(\frac{p_d}{p}\right)^{2/\gamma} - \left(\frac{p_d}{p}\right)^{(\gamma+1)/\gamma}\right]}{(\gamma - 1)\left[1 - \left(\frac{p_d}{p}\right)^{2/\gamma} C_{c_B}{}^2 \left(\frac{A_c}{A}\right)^2\right]}} \qquad \text{(B.12)}$$

where $p_d$ is the drywell pressure, $\rho_d$ is the drywell density ($\rho_d = p_d/RT_0$), $A_d$ is the flow area on the drywell side of the orifice, and A is the flow area on the bubble side of the orifice (downcomer vent area). The loss coefficients are given in Fig. B.2. All other symbols appearing in Eqs. (B.10) through (B.12) have been previously given except for g which is gravitational acceleration.

It should be noted that in the limit m = 0, the case corresponds to a reversible-adiabatic (i.e., isentropic) expansion which, in conjunction with the Rayleigh problem, has been solved in closed form if $\gamma = 4/3$ (see Ref. 2).

## REFERENCES


1. J. K. Vennard, Elementary Fluid Mechanics (John Wiley & Sons, New York, 1965), 4th ed., pp. 110-111 and 422-431.
2. H. Lamb, Hydrodynamics, (Cambridge Press, London, 1932), 6th ed.

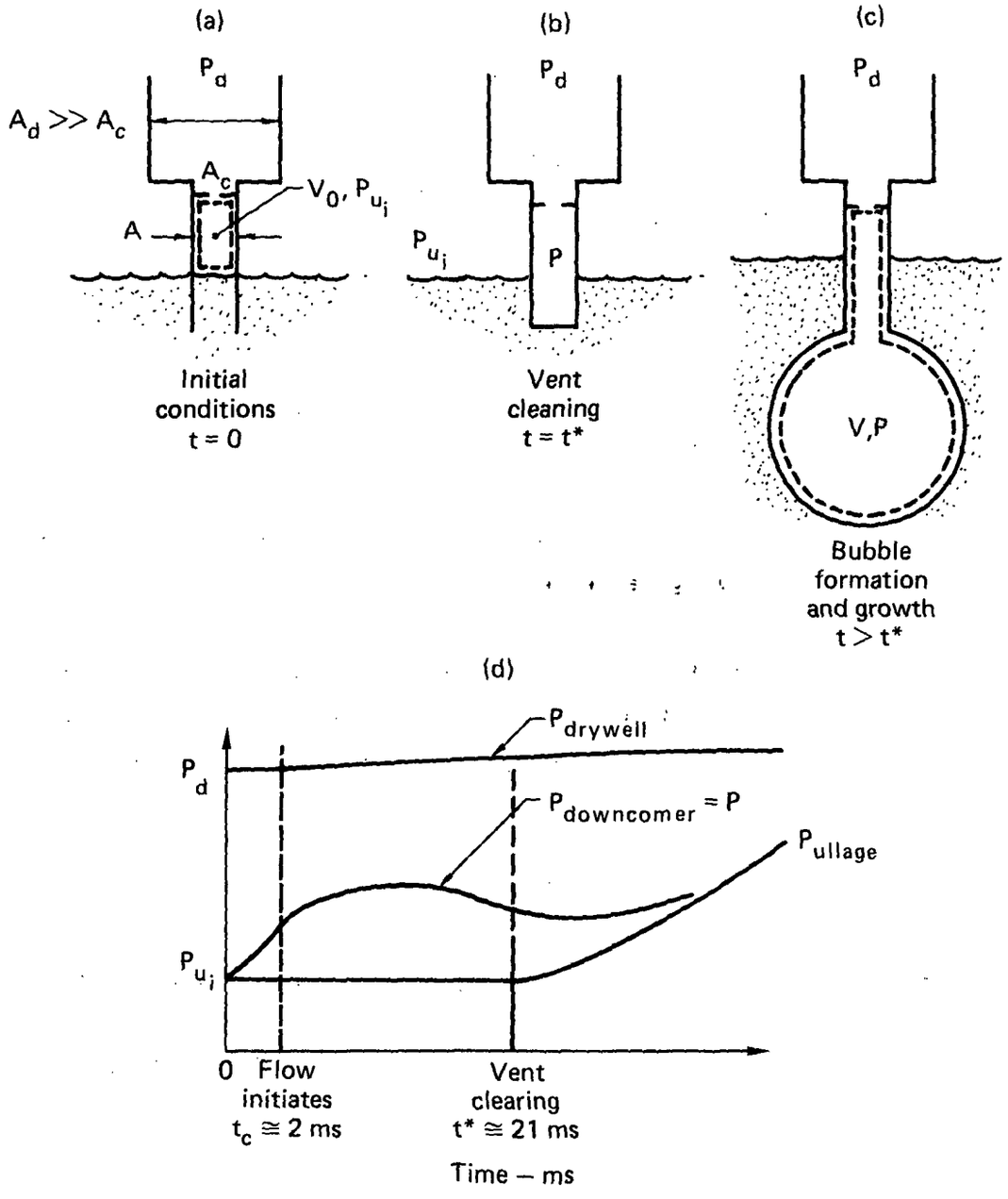


FIG. B.1. Schematic of model used to calculate downcomer pressure history. (a) Control volume before vent clearing. (b) Control volume at vent clearing. (c) Control volume after vent clearing. (d) Pressure-time histories upstream and downstream of orifice and in ullage.

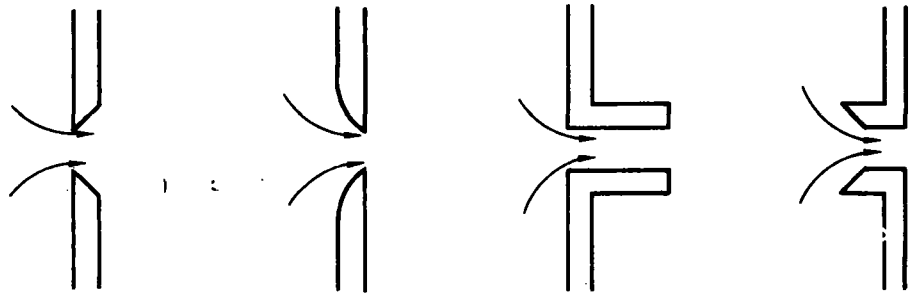

| | | | | |
|---|---|---|---|---|
| $C_c$ = | 0.62 | 1.0 | 1.0 | 0.52 |
| $C_f$ = | 0.98 | 0.98 | 0.80 | 0.98 |

FIG. B.2. Orifice coefficents (see Vennard[1]).

# APPENDIX C

## C.1.0 ACOUSTIC PIPE MODEL

The acoustic reflections in an open ended downcomer pipe are important for the analysis of the effect of chugging pulses in pool suppression systems. We have written a simple one-dimensional acoustic model code to calculate these pulses for use as a driving source in the PELE-IC code. A separate subroutine performs a Fourier analysis of the input and reflected pressure signals.

The pulses are governed by the wave equation for the pressure

$$\frac{\partial^2 P}{\partial t^2} = c^2 \frac{\partial^2 P}{\partial x^2} , \tag{C.1}$$

for which the second order stable central differencing scheme

$$\frac{P^{n+1} - 2P^n + P^{n-1}}{(\delta t)^2} = \frac{c^2(\delta^2 P^{n+1} + 2\delta^2 P^n + \delta^2 P^{n-1})}{4(\delta x)^2} \tag{C.2}$$

can be used, where

$$\delta^2 P = P_{j+1} - 2P_j + P_{j-1} ,$$

the subscript j indicates the spatial discretization, and the superscript n indicates the temporal discretization. We solve this equation using equal time steps ($\delta t$) and equal cell spacing ($\delta x$). If we define

$$\lambda = \frac{c\ t}{2\ x} ,$$

we may then rewrite Eq. (C.2) as

$$(P - \lambda\delta^2 P)^{n+1} = 2P^n - P^{n-1} + \lambda(2\delta^2 P^n + \delta^2 P^{n-1}) \quad . \tag{C.3}$$

If we define the terms on the right hand side as G, which are all evaluated at previous time steps, we can then rewrite Eq. (C.3) in the difference form

$$A_j P_{j-1} - B_j P_j + C_j P_{j+1} + G_j = 0 ,$$

where the pressure terms (P) are all evaluated at time n + 1, and

$$A_j = C_j = \lambda ,$$

$$B_j = 1 + 2\lambda ,$$

and

$$G_j = 2P_j^n - P_j^{n-1} + \lambda(2\delta^2 P^n + \delta^2 P^{n-1}) \quad .$$

These equations form a tridiagonal matrix and can be solved by standard techniques (see Richtmeyer and Morton[1] or Roache[2]) using the recurrence formula

$$P_j = E_j P_{j+1} + F_j , \tag{C.4}$$

where, for the general term, we have

$$E_j = \frac{C_j}{B_j - A_j E_{j-1}} \quad \text{and} \quad F_j = \frac{A_j F_{j-1} + G_j}{B_j - A_j E_{j-1}} \tag{C.5}$$

This equation is readily solved using forward and backward sweeps when we specify the boundary conditions at each end of the pipe. This method is a special case of Gaussian elimination.

For the initial boundary condition we have two cases.

Prescribed Driving Pressure. For this case the boundary condition is of the Dirichlet type and is provided by the specified input pressure time history

$$P_1^{n+1} = P_s^{n+1}(t) \quad .$$

In this case

$$E_2 = C/B \qquad \text{and} \qquad F_2 = G/B \quad ,$$

where

$$G = 2P_2^n - P_2^{n-1} + \lambda\left(2\delta^2 P_2^n + \delta^2 P_2^{n-1}\right) + AP_s \quad .$$

Reflected Pulse. When the reflected pulse returns to the wetwell end of the pipe we use the Neumann type boundary condition for a rigid wall; i.e., $\partial P/\partial x = 0$. Thus in this case we specify that

$$P_1^{n+1} = P_3^{n+1}(t)$$

which gives

$$E_2 = (A + C)/B \qquad \text{and} \qquad F_2 = G/B \quad ,$$

where now

$$G = 2P_2^n - P_2^{n-1} + \lambda\left(2\delta^2 P_2^n + \delta^2 P_2^{n-1}\right) \quad .$$

For the drywell boundary condition, we allow the pipe to be either closed or open and then we apply Neumann type boundary conditions.

Closed Pipe. In this case we specify that $P_{\ell+1} = P_{\ell-1}$, where $\ell$ is the index of the last cell. And then using Eqs. (C.3) and (C.4), we find that the final boundary pressure is

$$P_\ell = \frac{(A_\ell + C_\ell)F_{\ell-1} + G_\ell}{B_\ell - (A_\ell + C_\ell)E_{\ell-1}} \quad .$$

Open Pipe. For an open pipe the boundary condition is $P_{\ell+1} = -P_{\ell-1}$. And then substituting as above, we find

$$P_\ell = \frac{(A_\ell - C_\ell)F_{\ell-1} + C_\ell}{B_\ell - (A_\ell - C_\ell)E_{\ell-1}} .$$

## REFERENCES


1. R. D. Richtmeyer and K. W. Morton, Difference Methods for Initial-Value Problems (Interscience Publishers, New York, 1967), pp. 198-201.
2. P. J. Roache, Computational Fluid Dynamics (Hermosa Publishers, Albuquerque, NM, 1972), pp. 345-349.

# APPENDIX D

## D.1.0 FOURIER ANALYSIS

In many Fourier analysis problems we are interested in the frequency analysis of the pressure pulse or the resultant structural vibrational response. To perform the frequency analysis we have written two small codes using the techniques of the discrete Fourier transform. We used the Goertzel[1] procedure to evaluate the discrete Fourier transform. An excellent discussion of the characteristics and limitations of the discrete Fourier transform can be found in Brigham.[2] Here we give a brief summary of the salient features to guide the user in the use of this tool. Thus it is useful to remind the user of the characteristics and limitations of this method.

### D.1.1 CHARACTERISTICS OF DISCRETE FOURIER TRANSFORMS

The four main topics of interest to the user for interpreting the results of these Fourier transform codes are:

1. time domain sampling,
2. time domain truncation,
3. frequency domain sampling, and
4. time scaling.

We briefly discuss these topics and how they should be used to interpret the code results.

#### D.1.1.1 Time Domain Sampling

The sampling frequency specified by the time spacing ($\delta t$) between points on the signal determines the highest frequency ($f_c$) in the signal that can be determined without aliasing. As a general rule, one should pick a time spacing of

$$\delta t \leq \frac{1}{2f_c} .$$

A time sampling interval greater than this will lead to aliasing shown by the dotted line in Fig. D.1. Figure D.1 shows a typical frequency spectrum of a chugging driving pulse. The time domain sampling ($\delta t$) in this case is such that $1/\delta t$ is less than twice the maximum frequency of interest $f_c$. We find that aliasing occurs in the frequency region from $f_1$ to $f_c$, where $f_1 = (1/\delta t - f_c)$. To remedy this situation, a smaller $\delta t$ must be chosen in the time domain.

D.1.1.2 Time Domain Truncation

Usually we can only sample a portion of the entire signal we wish to analyze. This specific time sample is, in effect, a convolution of the signal with a unit rectangular pulse of duration $t_0$. This rectangular pulse has its own Fourier transform of the form $\sin(2\pi\ t_0 f)/t_0 f$ which also appears in the analysis. The transform of the sampling truncation function is shown in Fig. D.2, where h(t) represents the sampling truncation and H(f) is its corresponding Fourier transform.

The side lobes showing up in the transform of the truncation function will show up as ripples on the analyzed Fourier components and are not to be confused as frequencies present in the signal being analyzed.

Another problem associated with time domain truncation is that the analysis assumes that the function is periodic with period, $t_0$. If this is not the case, as is usually the situation, then additional high frequencies will be artificially introduced in the analysis. One should always take care to attempt to capture the periodicity of the signal, if it exists, in the sample to be analyzed.

D.1.1.3 Frequency Domain Sampling

Figure D.2 shows that an increase in sampling time gives us more of an impulse sampling in the frequency domain; this is what we desire for clear cut frequency analysis. Thus one should use as large a time sample as possible.

D.1.1.4 Time Scaling

The time scaling property of the Fourier transform states that, if we have the signal h(t) and its transform H(f), then we can also form the pair of

the scaled signal h(kt) and its transform 1/k*H(f/k). If we have a signal span of time $t_0$, which we subdivide into points $\delta t$ apart, then we will have $n = t_0/\delta t$ points in the time domain from which we can extract n/2 points in the frequency domain. Each point in the frequency domain has a frequency given by $f = i/n\delta t$, where i is the point in frequency space. By time scaling we can expand the display of the frequency analysis, but there is no gain in resolution. For our codes we have chosen to expand the frequency domain by using a scaling factor of k = 6 and thus each point on the output graph has a frequency of

$$f = \frac{i}{6n\delta t} \quad .$$

### D.2.1 EXAMPLE OF THE ANALYSIS OF ORGAN PIPE FREQUENCIES

To demonstrate the characteristics of our Fourier analysis code we will investigate the analysis of a typical chugging pulse exciting the organ pipe frequencies in a 94-ft long downcomer pipe with an assumed sound speed in steam of 1600 ft/s. The pulse used is illustrated in Fig. D.3 along with its discrete Fourier transform. The analysis was performed using the organ pipe code described in Appendix C. For this pipe the drywell end is open and the wetwell end closed. For this problem we used a spatial discretization of sixty zones and a time step of t = 0.7 ms for a Courant number of 0.71.

When this pulse is applied to the downcomer pipe it excites the organ pipe frequencies which are extracted from the frequency spectrum of the input signal. The use of the code is illustrated in Fig. D.4 where we show the results of the analysis of a single cycle. Note that the Fourier spectrum of the multiply reflected pulse is enclosed in the envelope of the original input signal.

In the organ pipe, the resonant frequencies are spaced at intervals of $\Delta f_r = s/2L_p$ where s is the sound speed and $L_p$ is the length of the pipe. In this example we have a complete cycle consisting of four pipe transient times. Thus the first side lobe will have a null at a frequency of $2/t_0$, where $t_0 = 4L_p/s$ or $\Delta f_s = \Delta f_r$ and there will be no side lobes due to the time truncation of the signal. This relationship is clearly seen in Fig. D.4.

As we increase the length of time in the analyzed signal, then the frequency sampling becomes more of an impulse function and we get a sharper determination of the frequency. As a side effect of this we begin to see the side lobes associated with the time domain truncation function. This is clearly shown in the examples of Fig. D.5 where we show the results of increasing the sampling time while maintaining the same sampling frequency. The number of side lobes in this case can be seen to be predicted by

$$s = t_0 \Delta f_r - 2 \quad .$$

These examples are given to illustrate the care one must exercise in analyzing more complex signals.

## REFERENCES


1. G. Goertzel, Fourier Analysis, Mathematical Methods for Digital Computers, Ralston & Wilf, Eds. (John Wiley & Sons, New York, 1967), pp. 258.
2. E. O. Brigham, The Fast Fourier Transform (Prentice-Hall, Inc., Englewood Cliffs, N.J., 1974).

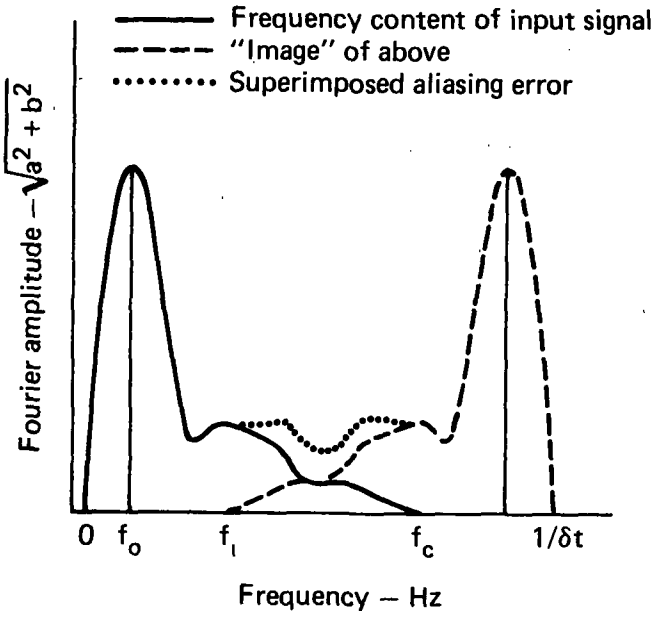


FIG. D.1. Example of aliasing in a typical chugging source pulse, where the time step interval is too large.

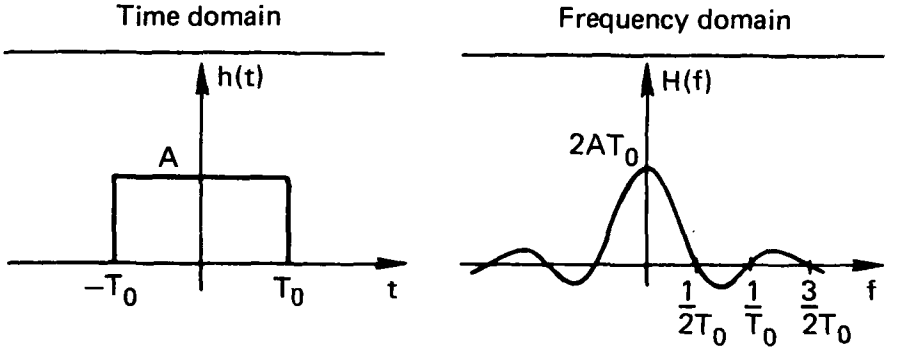


FIG. D.2. Effect in the frequency domain of time truncation of the signal.

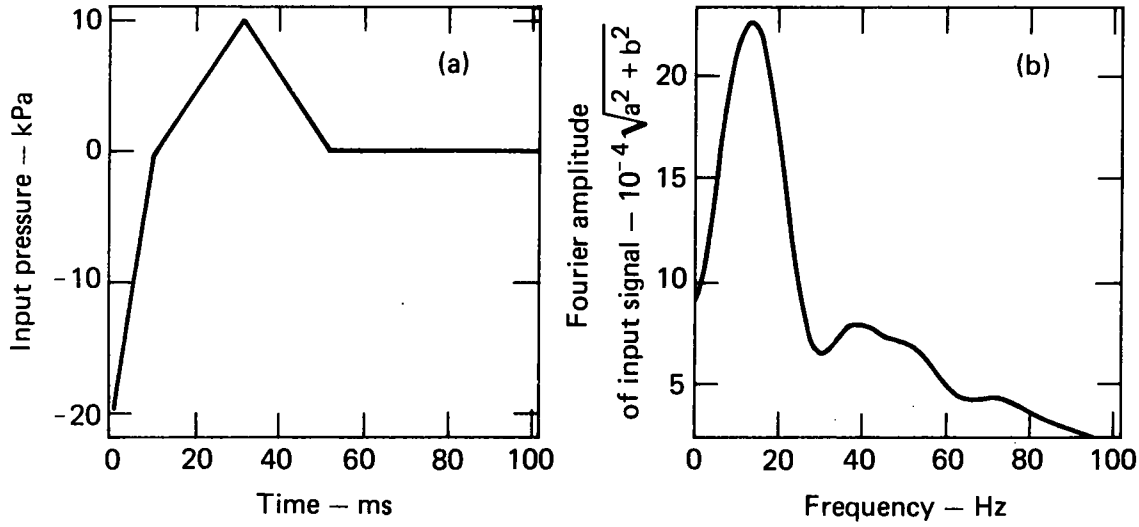


FIG. D.3. A typical simulated chugging pulse and its Fourier transform.

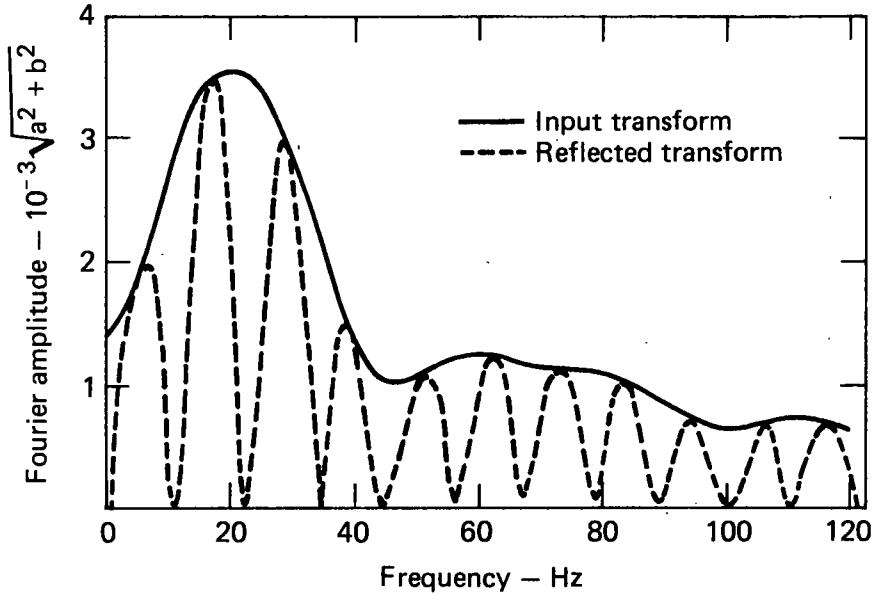


FIG. D.4. Extracted organ pipe frequencies from the chugging input pulse and its reflections.

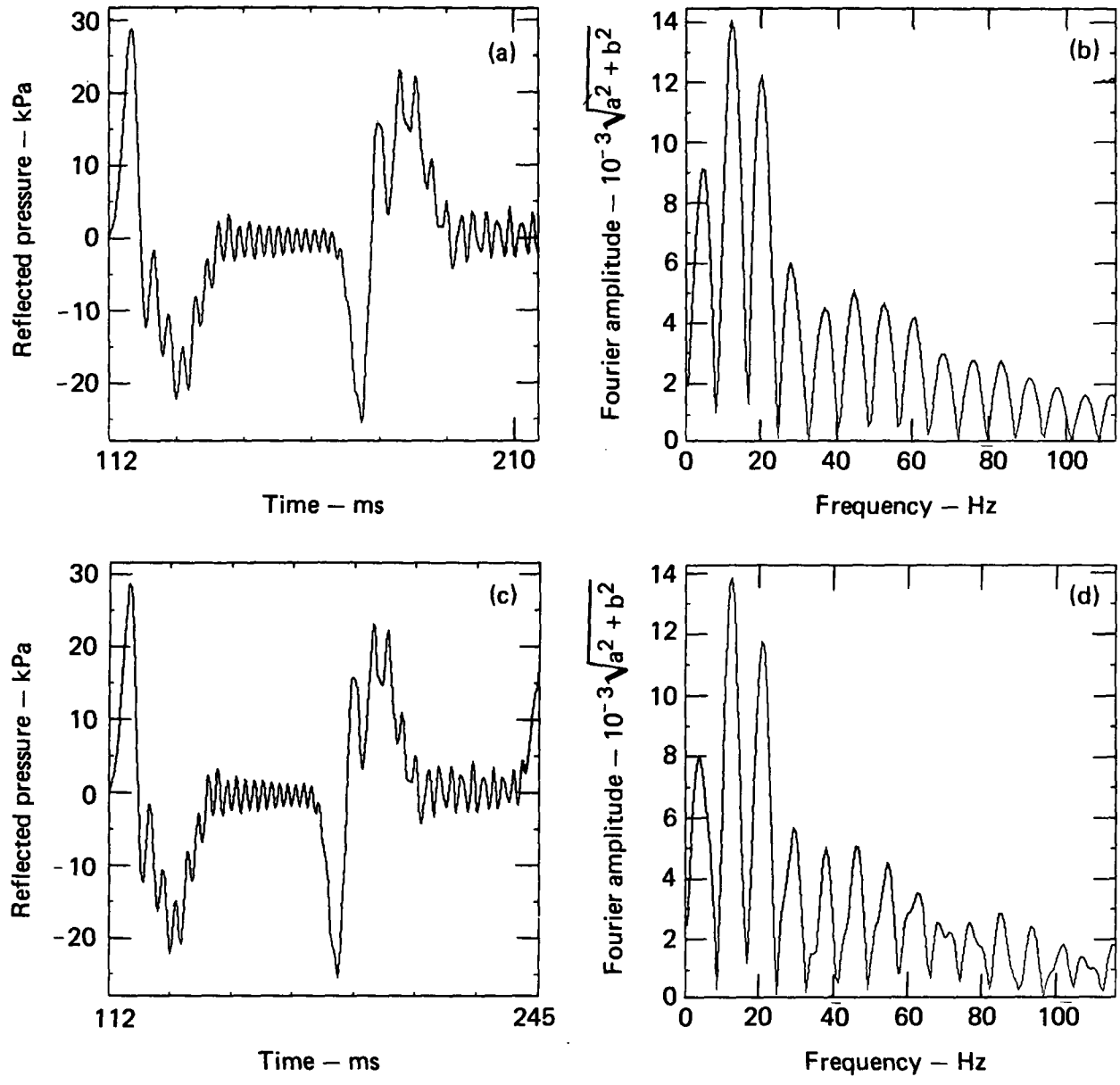


FIG. D.5. Effect of increasing the sampling time (six cases).

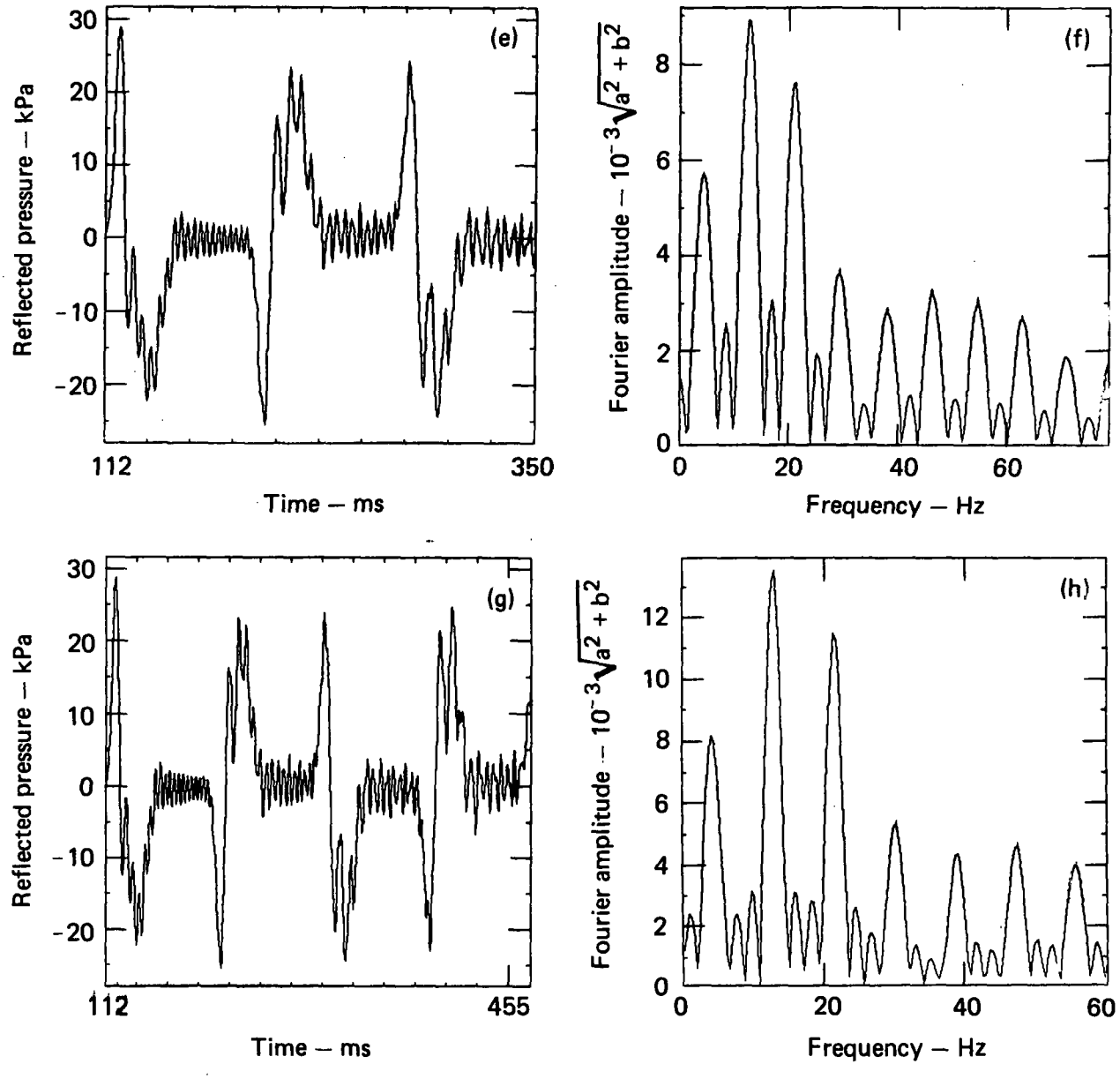


FIG. D.5. Continued.

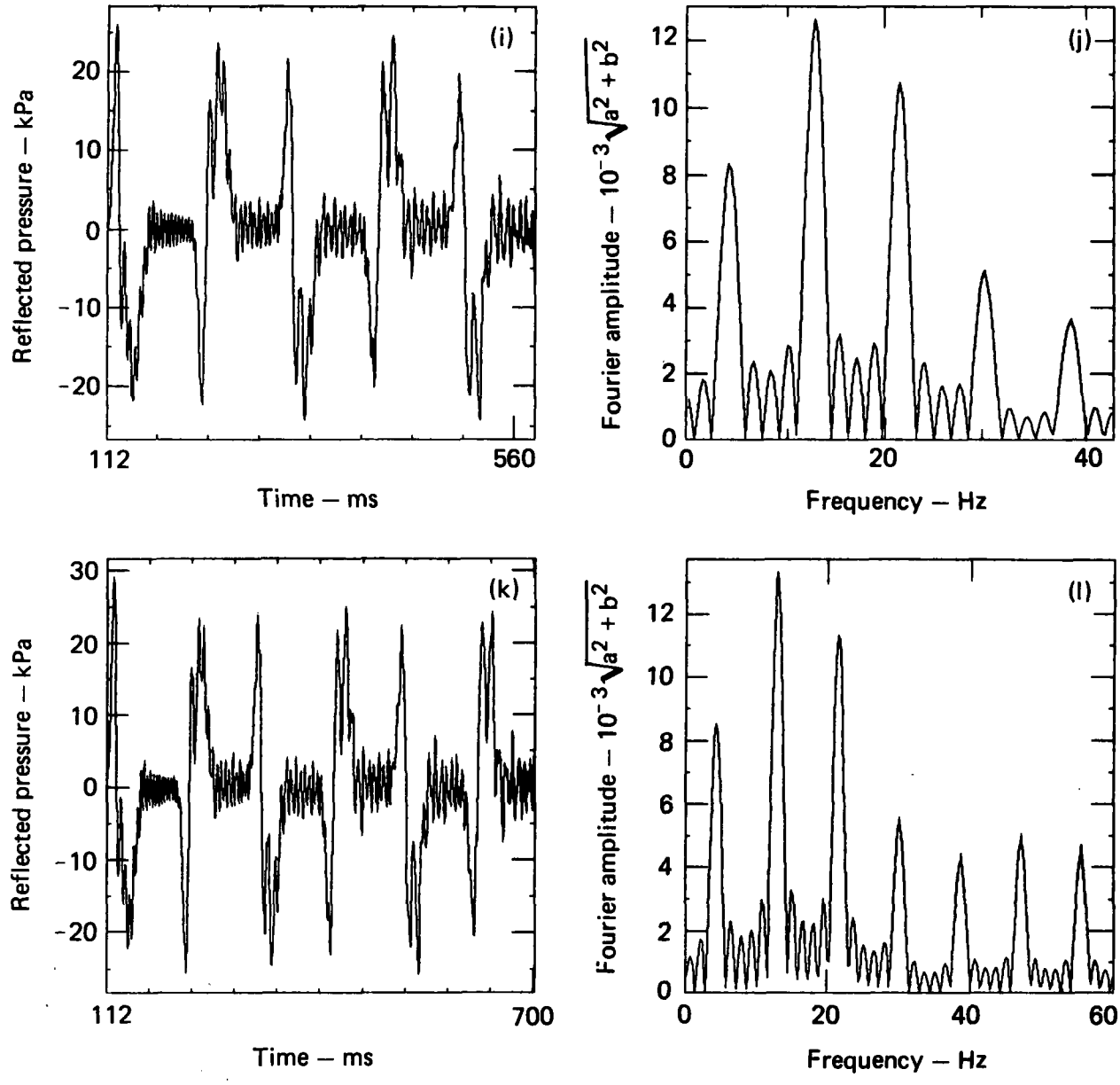


FIG. D.5. Continued.

APPENDIX E

# E.1.0 DERIVATION OF EXACT SOLUTION FOR INEXTENSIBLE ELLIPTIC BENDING MODE OF SUBMERGED SHELL

## E.1.1 INTRODUCTION

The centerline coordinates of the thin cylindrical shell of thickness (h) in its equilibrium position are r = R. The fluid surrounding the shell is located in $R + h/2 \leq r \leq b$, where h is the shell thickness and r = b is the outer free surface of the liquid (water). The dimensions are given in Table E.1. In the analysis which follows, we assume $h/r << 1$ so that the fluid is assumed located in $R \leq r \leq b$. Only the plane strain case is considered so that the polar coordinates are $(r,\Theta)$.

As the fluid-structure system is displaced from its equilibrium position and allowed to vibrate in an inextensible bending mode, the fluid displacement is $\vec{y}(r,\Theta,t)$ and the shell displacement is $\vec{x}(\Theta,t)$, where $\Theta$ is the circumferential dependence measured from a common axis. In each instant of time (t) we assume that $\vec{y}$ and $\vec{x}$ may be decomposed into a radial (subscript r) and a circumferential (subscript $\Theta$) component.

The governing equations of motion are given for the inviscid, compressible fluid and later specialized to an incompressible fluid. Both the shell and fluid are first assumed to vibrate in a general inextensible mode. Results are given only for the n = 2 mode (elliptical bending mode) which is the case to which PELE-IC is to be compared. Consideration is given to the fluid and shell separately.

### Fluid

The equation of state is

$$p = \rho_o c^2 s \ , \tag{E.1}$$

where s is defined as

$$s \equiv \frac{\rho}{\rho_o} - 1 \tag{E.2}$$

and p, $\rho$, $\rho_o$ and c are respectively the fluid pressure, density, undisturbed density, and sound speed. The compressible form of the continuity equation is given by

$$s + \text{div } \vec{y} = o \ . \tag{E.3}$$

The momentum equations may be combined with Eq. (E.1) to write

$$\frac{\partial \vec{y}}{\partial t} = -c^2 \text{ grad } s \ . \tag{E.4}$$

Shell

If a segment of the shell of density ($\rho_s$) is considered on which the fluid pressure ($p_s$) is exerted, the equations of motion are given by

$$-Q - p_s(\Theta,t)\ R + \frac{1}{R}\frac{\partial^2 M}{\partial \Theta^2} = R\ h\ \rho_s \frac{\partial^2 x_r}{\partial t^2} \tag{E.5}$$

and

$$\frac{\partial Q}{\partial \Theta} + \frac{1}{R}\frac{\partial M}{\partial \Theta} = R\ h\ \rho_s \frac{\partial^2 x_\Theta}{\partial t^2} \ , \tag{E.6}$$

where the shear (Q) and bending moment (M) are given through the inextensible constraints and are:

$$Q = \frac{Eh/R}{1 - \nu^2}\left(\frac{\partial x_\Theta}{\partial \Theta} + x_r\right) \tag{E.7}$$

and

$$M = \frac{Eh^3/R^2}{12(1 - \nu^2)}\left(-\frac{\partial^2 x_r}{\partial \Theta^2} + \frac{\partial x_\Theta}{\partial \Theta}\right) \ , \tag{E.8}$$

where E and $\nu$ are Young's elastic modulus and Poisson's ratio, respectively.

The boundary condition on the outer surface of the fluid is given by

$$p = s = o \quad \text{at} \quad r = b \quad \text{for all } \theta,\ t > o \ . \tag{E.9}$$

The matching conditions for the inviscid fluid and shell at the interface are given by

$$p_s(\theta,t) = p(R,\theta,t) \tag{E.10}$$

and

$$x_r(\theta,t) = y_r(R,\theta,t) \ . \tag{E.11}$$

Note that the relative tangential motion between shell and fluid is unconstrained (owing to the absence of fluid viscosity). It may be shown that the tangential motions of the two are opposite one another.

The above analysis presents the framework upon which the solution follows. Assume the existence of a separable solution where

$$y_r = H_f(r)\ \zeta_n(\theta)\ f_1(t) \ , \tag{E.12}$$

$$y_\theta = G_f(r)\ \delta_n(\theta)\ f_2(t) \ , \tag{E.13}$$

$$s = w(r)\ q_n(\theta)\ f_3(t) \ , \tag{E.14}$$

$$x_r = H_s\ g_n(\theta)\ f_4(t) \ , \tag{E.15}$$

and

$$x_\theta = G_s\ \beta_n(\theta)\ f_5(t) \ . \tag{E.16}$$

The product solutions, Eqs. (E.12) through (E.16), when put into the preceding equations, have validity if the following constraints are satisfied for circumferential dependence:

$$\zeta_n = q_n = g_n \tag{E.17}$$

and

$$\delta_n = \beta_n \sim -\zeta_n'^{*} \tag{E.18}$$

which for any integer n are satisfied by

$$\zeta_n = \cos n\theta \tag{E.19}$$

and

$$\delta_n = \sin n\theta \ . \tag{E.20}$$

Also, the temporal dependence must be common; that is

$$f_1 = f_2 \ . \ . \ . = f_5 = f(t) \tag{E.21}$$

with

$$f'' + \omega_n^2 f = 0 \ , \tag{E.22}$$

where $\omega_n$ is a constant of separation which is here identified as the circular natural frequency sought. The general (periodic) solution to Eq. (E.22) is

$$f = e^{\pm i\omega_n t} \ . \tag{E.23}$$

---

*The primed quantities represent ordinary differentiation of that quantity with respect to its sole dependent variable; in this case with respect to $\theta$.

Equations (E.19) through (E.23) are the only conditions which permit a separable solution. Equation (E.23) implies periodicity of circular frequency ($\omega_n$) in all variables, and, therefore, the solution developed here allows computation of only those eigenvalues ($\omega_n$) associated with a particular mode shape, cos $n\theta$. It should be emphasized that the following solutions hold only for periodicity in all variables. The eigenvalues are now derived.

The circumferential component of the momentum equation, Eq. (E.4), and the continuity equation, Eq. (E.3), give the following respective constraints for the radial components given in Eqs. (E.12)-(E.14):

$$G_f = -\left(\frac{c}{\omega_n}\right)^2 \frac{n}{r} w \tag{E.24}$$

and

$$-w = \frac{dH_f}{dr} + \frac{H_f + n\, G_f}{r} \tag{E.25}$$

which combine into

$$\frac{dH_f}{dr} + \frac{H_f + nG_f}{r} - \left(\frac{\omega_n}{c}\right)^2 \frac{r}{n} G_f = 0 \ . \tag{E.26}$$

If we define a displacement potential $\phi(r)$ such that

$$H_f = -\phi_n' \quad \text{and} \quad G_f = \frac{n}{r} \phi_n \ , \tag{E.27}$$

then $\phi_n$ satisfies the Bessel equation of order n so that

$$r^2 \phi_n'' + r\phi_n' + \left[\left(\frac{\omega_n r}{c}\right)^2 - n^2\right] \phi_n = 0 \ . \tag{E.28}$$

A solution to Eq. (E.28) satisfying Eq. (E.9) is

$$\phi_n = J_n\left(\frac{\omega_n r}{c}\right) - Y_n\left(\frac{\omega_n r}{c}\right) \frac{J_n\left(\frac{\omega_n b}{c}\right)}{Y_n\left(\frac{\omega_n b}{c}\right)} \quad . \tag{E.29}$$

The eigenvalues ($\omega_n$) are found when radial displacements (Eq. (E.11)) are equated between fluid and shell. Application of Eq. (E.11) will require calculating the following parameter

$$\frac{p(R,\Theta,t)/(\rho_o^2 \omega_n}{R y_r(R,\Theta,t)} = \frac{1}{R}\left(\frac{c^2}{\omega_n}\right)\frac{w(r)}{H_f(R)} = \frac{1}{R}\left(\frac{c}{\omega_n}\right)^2 \frac{\left(\frac{\omega_n}{c}\right)^2 \phi_n(R)}{\phi_n'(R)}$$

$$= \frac{1}{R}\frac{\phi_n(R)}{\phi_n'(R)} = \frac{1}{R}\frac{\phi_n(R)}{\left[\frac{\omega_n}{c}\phi_{n-1}(R) - \frac{n}{R}\phi_n(R)\right]} = \frac{1}{\frac{\omega_n R}{c}\frac{\phi_{n-1}(R)}{\phi_n(R)} - n}$$

$$= \frac{1}{\frac{\omega_n R}{c}\left[\frac{J_{n-1}\left(\frac{\omega_n R}{c}\right) - Y_{n-1}\left(\frac{\omega_n R}{c}\right)\frac{J_n}{Y_n}\left(\frac{\omega_n b}{c}\right)}{J_n\left(\frac{\omega_n R}{c}\right) - Y_n\left(\frac{\omega_n R}{c}\right)\frac{J_n}{Y_n}\left(\frac{\omega_n b}{c}\right)}\right]} \quad . \tag{E.30}$$

Now we consider the shell. Putting the separated variables in Eqs. (E.17) and (E.18) gives

$$-n\frac{Eh}{(1-\nu^2)}\frac{(nG_s + H_s)}{R^2} - n\frac{E\,h^3/R^4}{12(1-\nu^2)}\left(n^2 H_s + n G_s\right) = -h\rho_s \omega_n^2 G_s$$

and

$$\frac{-Eh/R}{(1-\nu^2)}\frac{(nG_s + H_s)}{R\rho_o \omega_n^2} - \left(\frac{c}{\omega_n}\right)^2 w(R) - \frac{n^2 E\, h/R^3}{12(1-\nu^2)}\frac{\left(n^2 H_s + nG_s\right)}{R\rho_o \omega_n^2} = -\frac{h\rho_s}{\rho_o} H_s \quad .$$

Equations (E.19) through (E.23) are the only conditions which permit a separable solution. Equation (E.23) implies periodicity of circular frequency ($\omega_n$) in all variables, and, therefore, the solution developed here allows computation of only those eigenvalues ($\omega_n$) associated with a particular mode shape, cos $n\theta$. It should be emphasized that the following solutions hold only for periodicity in all variables. The eigenvalues are now derived.

The circumferential component of the momentum equation, Eq. (E.4), and the continuity equation, Eq. (E.3), give the following respective constraints for the radial components given in Eqs. (E.12)-(E.14):

$$G_f = -\left(\frac{c}{\omega_n}\right)^2 \frac{n}{r} w \tag{E.24}$$

and

$$-w = \frac{dH_f}{dr} + \frac{H_f + n\, G_f}{r} \tag{E.25}$$

which combine into

$$\frac{dH_f}{dr} + \frac{H_f + nG_f}{r} - \left(\frac{\omega_n}{c}\right)^2 \frac{r}{n} G_f = 0 \ . \tag{E.26}$$

If we define a displacement potential $\phi(r)$ such that

$$H_f = -\phi_n' \quad \text{and} \quad G_f = \frac{n}{r} \phi_n \ , \tag{E.27}$$

then $\phi_n$ satisfies the Bessel equation of order n so that

$$r^2 \phi_n'' + r\phi_n' + \left[\left(\frac{\omega_n r}{c}\right)^2 - n^2\right] \phi_n = 0 \ . \tag{E.28}$$

A solution to Eq. (E.28) satisfying Eq. (E.9) is

$$\phi_n = J_n\left(\frac{\omega_n r}{c}\right) - Y_n\left(\frac{\omega_n r}{c}\right) \frac{J_n\left(\frac{\omega_n b}{c}\right)}{Y_n\left(\frac{\omega_n b}{c}\right)} \quad . \tag{E.29}$$

The eigenvalues ($\omega_n$) are found when radial displacements (Eq. (E.11)) are equated between fluid and shell. Application of Eq. (E.11) will require calculating the following parameter

$$\frac{p(R,\Theta,t)/(\rho_o^2\omega_n}{Ry_r(R,\Theta,t)} = \frac{1}{R}\left(\frac{c^2}{\omega_n}\right)\frac{w(r)}{H_f(R)} = \frac{1}{R}\left(\frac{c}{\omega_n}\right)^2 \frac{\left(\frac{\omega_n}{c}\right)^2 \phi_n(R)}{\phi_n'(R)}$$

$$= \frac{1}{R}\frac{\phi_n(R)}{\phi_n'(R)} = \frac{1}{R}\frac{\phi_n(R)}{\left[\frac{\omega_n}{c}\phi_{n-1}(R) - \frac{n}{R}\phi_n(R)\right]} = \frac{1}{\frac{\omega_n R}{c}\frac{\phi_{n-1}(R)}{\phi_n(R)} - n}$$

$$= \frac{1}{\frac{\omega_n R}{c}\left[\frac{J_{n-1}\left(\frac{\omega_n R}{c}\right) - Y_{n-1}\left(\frac{\omega_n R}{c}\right)\frac{J_n}{Y_n}\left(\frac{\omega_n b}{c}\right)}{J_n\left(\frac{\omega_n R}{c}\right) - Y_n\left(\frac{\omega_n R}{c}\right)\frac{J_n}{Y_n}\left(\frac{\omega_n b}{c}\right)}\right]} \quad . \tag{E.30}$$

Now we consider the shell. Putting the separated variables in Eqs. (E.17) and (E.18) gives

$$-n\frac{Eh}{(1-\nu^2)}\frac{(nG_s + H_s)}{R^2} - n\frac{E h^3/R^4}{12(1-\nu^2)}\left(n^2 H_s + n G_s\right) = -h\rho_s \omega_n^2 G_s$$

and

$$\frac{-Eh/R}{(1-\nu^2)}\frac{(nG_s + H_s)}{R\rho_o \omega_n^2} - \left(\frac{c}{\omega_n}\right)^2 w(R) - \frac{n^2 E h/R^3}{12(1-\nu^2)}\frac{\left(n^2 H_s + nG_s\right)}{R\rho_o \omega_n^2} = -\frac{h\rho_s}{\rho_o} H_s \quad .$$

Combining the above two equations and letting

$$\epsilon \equiv \frac{1}{12}\left(\frac{h}{r}\right)^2 << 1 \quad \text{and} \quad \sigma \equiv \frac{(1-\nu^2)c^2\rho_s\left(\frac{\omega_n R}{c}\right)^2}{n^2 E}$$

gives from the first

$$nG_s + H_s = -\frac{\left[(n^2-1)\,\epsilon + \sigma\right] H_s}{1+\epsilon-\sigma}$$

and from the second, using the first,

$$\frac{1}{R}\left(\frac{c}{\omega_n}\right)^2 \frac{w(R)}{H_s} = \frac{-(n^2-1)^2\,\frac{1}{12}\,E\left(\frac{h}{R}\right)^3 \frac{1}{(1-\nu^2)R^2\rho_o\omega_n^2} + \left[\frac{n^4}{12}\left(\frac{h}{R}\right)^2 + 1\right]\frac{1}{n^2}\frac{h\rho_s}{R\rho_o}}{1+\epsilon-\sigma} + \frac{h}{R}\frac{\rho_s}{\rho_o} \,.$$

If the inextensible bending is considered, both $\epsilon$ and $\sigma$ are much less than unity and we have

$$\frac{1}{R}\left(\frac{c}{\omega_n}\right)^2 \frac{w(R)}{H_s} = -(n^2-1)^2\,\frac{1}{12}\,E\left(\frac{h}{R}\right)^3 \frac{1}{(1-\nu^2)\,R^2\rho_o\omega_n^2} + \left\{\left[1 + \frac{n^4}{12}\left(\frac{h}{R}\right)^2\right]\frac{1}{n^2} + 1\right\}\frac{h\rho_s}{R\rho_o} \,. \tag{E.31}$$

Equating Eqs. (E.30) and (E.31) and recognizing $H_s = H_f(R)$ from Eq. (E.11) gives the eigenvalue equation from which $\omega_n$ is obtained for any given mode number n.

An explicit result for $\omega_n$ may be obtained by specializing Eq. (E.30) in the incompressible limit, $\omega_n\, b/c \to 0$

$$\lim_{\left(\frac{\omega_n R}{c}\right)\to 0} \frac{1}{R}\left(\frac{c}{\omega_n}\right)^2 \frac{w(R)}{H_f(R)} = -\left[\frac{\frac{1}{n}}{\frac{1}{2} + \frac{\left(\frac{R}{b}\right)^{2n}}{1 - \left(\frac{R}{b}\right)^{2n}}}\right] \tag{E.31}$$

and

$$\left(\frac{\omega_n b}{c}\right) \to 0 \ .$$

Equating the incompressible result to that obtained from Eq. (E.31) gives the incompressible frequency as $\omega_{n_\infty} = \lim_{c \to \infty} \omega_n$

$$\omega_{n_\infty}^2 = \frac{\left(\omega_n^2\right)_{\frac{R}{b}=1}}{1 + \frac{n}{2(n^2+1)} \frac{1}{\frac{h\rho_s}{R\rho_o}\left[\frac{1}{2} + \frac{\left(\frac{R}{b}\right)^{2n}}{1 - \left(\frac{R}{b}\right)^{2n}}\right]}} , \tag{E.32}$$

where $\left(\omega_n^2\right)_{R/b=1}$ is the square of the natural frequency of the shell in absence of the liquid annulus

$$\left(\omega_n^2\right)_{\frac{R}{b}=1} = \frac{n^2(n^2-1)^2}{(n^2+1)} \frac{E}{R^2}\left(\frac{h}{R}\right)^2 \frac{1}{12(1-\nu^2)\rho_s} \equiv (2\pi f_0)^2 , \tag{E.33}$$

where $f_0$ is the frequency in Hz for no liquid annulus present. Note for a shell infinitely surrounded by an incompressible fluid

$$\left(\omega_{n_\infty}^2\right)_{\frac{b}{R}=\infty} = \frac{\left(\omega_n^2\right)_{\frac{R}{b}=1}}{1 + \frac{n}{4(n^2+1)} \frac{1}{\frac{h}{R}\frac{\rho_s}{\rho_o}}} . \tag{E.34}$$

Equations (E.32)-(E.34) were evaluated for the elliptical bending mode, n = 2, and the results were given in the text.

In the incompressible limit the radial velocity distribution ($u_r$) normalized to the radial component of shell velocity at fixed $\Theta$ and t is given by

$$\frac{u}{u_{shell}}(r) = \frac{H_f(r)}{H_f(R)} = \frac{\phi_n'(r)}{\phi_n'(R)}$$

which for the n = 2 mode is

$$\frac{u}{u_{shell}}(r) = \frac{r}{R}\left\{\frac{1 + \frac{1}{2}\left[\left(\frac{b}{r}\right)^4 - 1\right]}{1 + \frac{1}{2}\left[\left(\frac{b}{R}\right)^4 - 1\right]}\right\}, \qquad 1 \leq \frac{r}{R} \leq \frac{b}{R} \tag{E.35}$$

which is the basis for the velocity profile.

TABLE E.1 Dimensions for submerged shell.

| |
|---|
| $E$ = Young's modulus of elasticity ($2.0685 \times 10^6$ bars), |
| $\rho_s$ = shell density (7.803 gm/cm$^3$), |
| $R$ = shell radius (25.72 cm), |
| $\nu$ = Poisson's ratio (0.3), |
| $h$ = shell thickness (0.635 cm), and |
| $b$ = free surface radius (82.8 cm). |

APPENDIX F

# F.1.0 LIVERMORE ONE-FIFTH SCALE PARAMETER STUDY

## F.1.1 INTRODUCTION

We conducted a parameter study of the LLL 1/5-scale pressure suppression experiment (PSE) facility using the PELE-IC code. The object was to investigate the sensitivity of response measurements, such as vent clearing time and peak bottom pressure to variations in drywell pressurization rate, downcomer submergence, torus pool level, downcomer fill level, and initial wetwell pressure. Selected downcomer pressure time histories were used for the calculations.

## F.2.1 COMPUTER MODEL AND BASE CASE

The calculational model is shown in Fig. F.1a. We assumed plane strain conditions in all calculations and the ringheader was omitted because of present code limitations. We considered only peak bottom pressure associated with the download and we assumed the fluid was inviscid. Additional details on the geometry and initial conditions used in the calculations, as well as results for a base case discussed below, are given in Table F.1 and Fig. F.2. All calculations used a time step of 0.2 ms and a zone size of 60 by 60 mm. Each calculation required about 90 s of CDC 7600 CPU time. The same code version was used for all problems.

We first calculated $90^{o}$-sector experiment 1.3.1 with the nominal values of torus water level, initial wetwell pressure, and downcomer pressure time history. It is of interest to compare the $90^{o}$- and $7.5^{o}$-sector bottom pressure-time histories as shown in Fig. F.2. Pressure data are very similar for the two cases. Input description for this case is given in Table F.1. The results are compared in Fig. F.3. This initial experimental drywell pressure was equal to the initial wetwell pressure of about 20 kPa for the nominal case.

Figure F.3 shows that vent clearing time is about 20 ms later than experiment and that peak bottom pressure is 16% higher. Since the calculation is done in plane geometry the source is clearly overspecified so that an

overpressure prediction is to be expected. We assume that the results of this parameter study will not be greatly affected by this model since the results are presented in a normalized way. The purpose of the comparison of Fig. F.3 is to provide information for code validation and is only indirectly related to the parameter study.

## F.3.1 RESULTS AND DISCUSSION

### F.3.1.1 Downcomer Fill Level

Results were found by lowering by 25, 50, and 100% the water level in the downcomer pipe (see Fig. F.1). The torus and downcomer water levels are identical only for the nominal case. The downcomer pressures are identical to that shown in Fig. F.3, except we corrected the initial downcomer pressure by the static head to be consistent with the water depression. Data are presented in Table F.2 for the nominal and three cases studied.

Table F.2 shows that vent clearing and peak pressure times, for the same driving pressure, are delayed as the fill level is increased. The nominal case (with the most fluid in the downcomer) gives the highest peak bottom pressure. An initial overpressure that lowers the downcomer fill level will decrease the peak bottom pressure. The data show a 13% decrease in peak download from filled to precleared downcomer. Experiments indicate a variation of about 45%. Lack of exact agreement is to be expected since the downcomer pressure histories used in these calculations are only approximations of experimental conditions. No attempt was made to simulate each experiment.

### F.3.1.2 Downcomer Submergence

Sensitivity to downcomer submergence is given in Table F.3. We considered three cases. For these cases the initial water level in the downcomer and torus was equal. In case A the downcomer was physically raised or lowered by plus or minus 25% using the conditions of the nominal case. Case B is for nominal downcomer geometry and pressure history (see Fig. F.3)

with the torus water level raised plus or minus 25%. For case C we used the downcomer levels of case A, but the downcomer pressure was increased at the constant slope of the nominal case from 20 kPa until vent clearing time and then held constant. It should be noted that for this case the downcomer pressure history differs from the two other cases which used the nominal pressure history of Fig. F.3. The peak downcomer pressures for case C were 57.1 kPa (-25%), 62.5 kPa (nominal submergence) and 68.0 kPa (+25%).

Cases A and B used the nominal dynamic pressure time history. Both of these studies suffer from the inconsistency between dynamic pressure history and vent clearing dynamics in that peak downcomer pressure time is not coincident, or roughly coincident, with vent clearing time. Case C was done with the dynamic downcomer pressure increased at the nominal pressurization rate until vent clearing and held constant thereafter. The code then predicts less peak pressure for less submergence. For this case the calculated percentage spread in response pressure between the plus or minus 25% downcomer extensions is 21%. By comparison the LLL experimental spread in peak pressure between the -38 and +42% downcomer extensions was 29%. Note again that we are not simulating actual experiments.

We found similar results for cases A and B where either the pipe or water in the torus were moved up or down by 25%. Both cases A and B used the nominal downcomer pressure history.

### F.3.1.3 Pressurization Rate

Results are given in Table F.4. We varied the nominal pressurization rate in the downcomer by plus or minus 25% and maintained this rate through vent clearing. Typical downcomer pressure time histories from the PSE experiments (see Fig. F.4) are similar to the pressure histories used in this parameter study.

### F.3.1.4 Change in Wetwell Pressure

Results are given in Table F.5. We varied the wetwell pressure plus or minus 25% and changed the downcomer pressure to maintain the same nominal

pressure difference. As expected, we found no change in vent clearing times and since the dynamic bottom pressure must remain unchanged, the total bottom pressure difference is simply due to the increase (or decrease) in the initial wetwell pressure.

### F.3.1.5 Discussion

The question of up-load sensitivity is considered in the main text. The upload calculations in PELE-IC were implemented after these parameter studies were completed.

This study shows that a 25% change in downcomer submergence, pressurization rate, and change in wetwell pressure result in about a 10% change in peak bottom pressure.

TABLE F.1. Nominal conditions and check calculation (Exp. 1.3.1).

| | PELE-IC | Exp ($90^{o}$sector) |
|---|---|---|
| Geometry | | |
| Torus radius, mm | 945.0 | 944.9 |
| Torus water level at center, mm | 90.67 | 90.67 |
| Downcomer pipe dimension, mm | 60. (width) | 60.96 (radius) |
| Spacing between downcomer pipe centers, mm | 480. | 487.7 |
| Downcomer submergence, mm | | |
| Torus wall thickness | 246.7 | 243.8 |
| Initial conditions | | |
| Initial wetwell pressure, kPa | 20.0 | 20.4 |
| Initial downcomer pressure, kPa | 20.0 | 20.4 |
| Drywell pressurization rate, kPa | 187.8 | 187.8 |
| Results | | |
| Peak bottom pressure, kPa | 56.8 | 49.0 |
| Time at start of pressurization, s | 0.0 | 2.9875 |
| Vent clearing time, s | 0.134 | 3.1875 |
| Time increment to clear vent, s | 0.134 | 0.104 to 0.120 |
| Peak pressure time, s | 0.143 | 3.1935 |

TABLE F.2. Downcomer fill level.

| Downcomer fill level | Identical downcomer pressures (water in static equilibrium at time zero) | | |
|---|---|---|---|
| | Normalized vent clearing time | Normalized peak bottom pressure time | Normalized peak bottom pressure |
| 0.0[a] | 0.00 | 1.01 | 0.870 |
| 0.50 | 0.724 | 0.853 | 0.933 |
| 0.75 | 0.866 | 0.874 | 0.982 |
| 1.00[b] | 1.00 | 1.00 | 1.00 |

[a]Precleared.

[b]Nominal.

TABLE F.3. Downcomer submergence (water level same in downcomer and torus).

| Downcomer submergence | Normalized vent clearing time | Normalized peak pressure time | Normalized peak pressure |
|---|---|---|---|
| | (Identical downcomer pressure histories) | | |
| 0.75 | 0.851 | 0.951 | 1.01 |
| 1.00[a] | 1.00 | 1.00 | 1.00 |
| 1.25 | 1.07 | 1.09 | 0.950 |
| | (Identical downcomer pressure histories with downcomer fixed and torus water level raised or lowered) | | |
| 0.75 | 0.851 | 0.944 | 1.01 |
| 1.00[a] | 1.00 | 1.00 | 1.00 |
| 1.25 | 1.13 | 1.09 | 0.954 |
| | (Pressure ramps upwards until vent clearing time and remains constant thereafter) | | |
| 0.75 | 0.873 | 0.979 | 0.913 |
| 1.00[b] | 1.00 | 1.00 | 1.00 |
| 1.25 | 1.11 | 1.09 | 1.12 |

[a]Nominal case.

[b]See text.

TABLE F.4. Downcomer pressurization rate.

| Pressurization rate | Normalized vent clearing time | Normalized peak pressure time | Normalized peak pressure |
|---|---|---|---|
| 0.75 | 1.10 | 1.10 | 0.901 |
| 1.00[a] | 1.00 | 1.00 | 1.00 |
| 1.25 | 0.918 | 0.928 | 1.100 |

[a]Nominal geometry.

TABLE F.5. Wetwell pressure.

| Initial wetwell pressure | (Downcomer pressure shifted at all times by change in wetwell pressure) | | |
|---|---|---|---|
| | Normalized vent clearing time | Normalized peak pressure time | Normalized peak pressure |
| 0.75 | 0.992 | 0.993 | 0.915 |
| 1.00[a] | 1.00 | 1.00 | 1.00 |
| 1.25 | 1.00 | 0.993 | 1.09 |

[a]Nominal geometry.

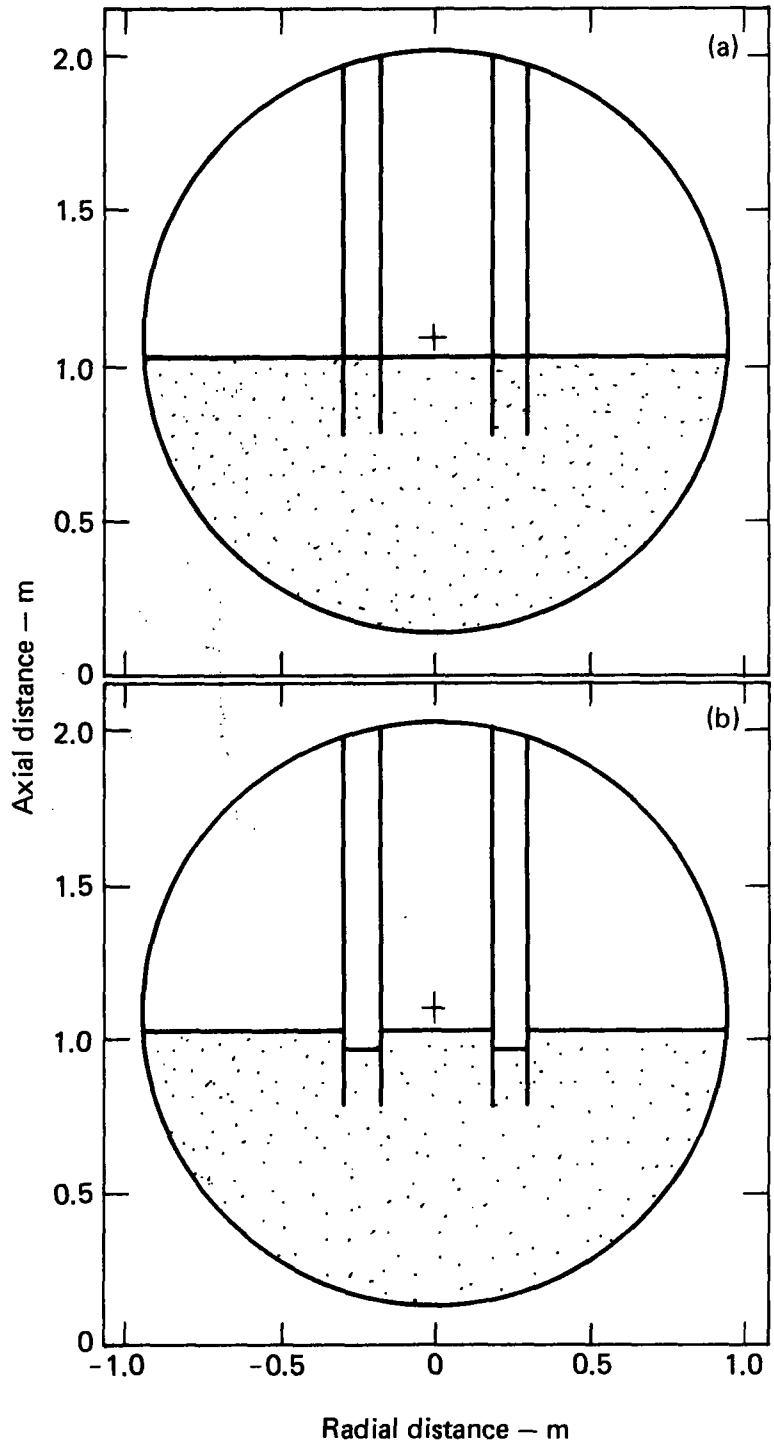


FIG. F-1. LLL 1/5-scale model. (a) Nominal geometry. (b) Typical initial conditions for downcomer fill level parameter study.

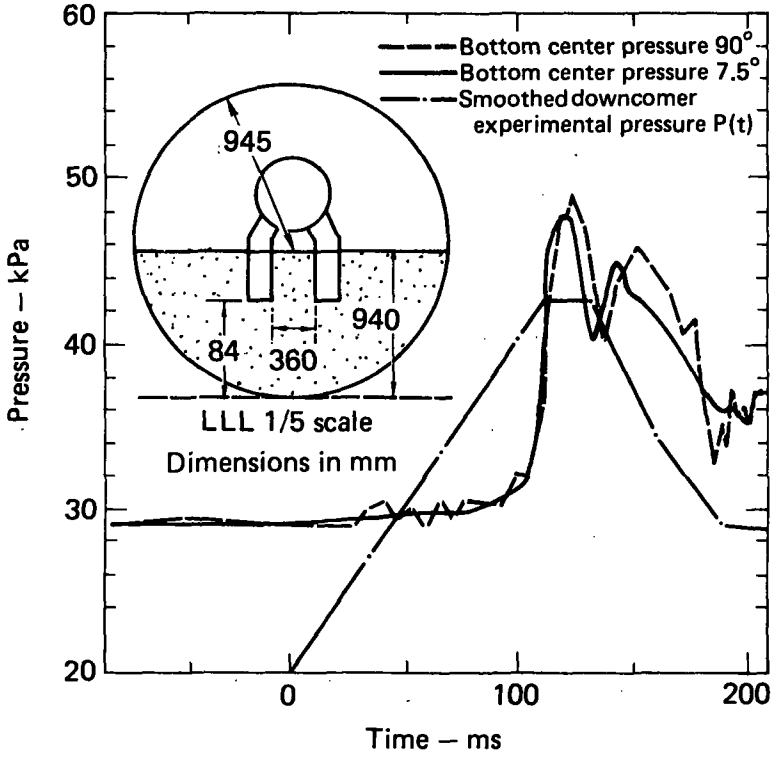


FIG. F.2. LLL 1/5-scale comparison of bottom pressure for 7.5- and 90°-torodial segments for experiment 1.3.1.

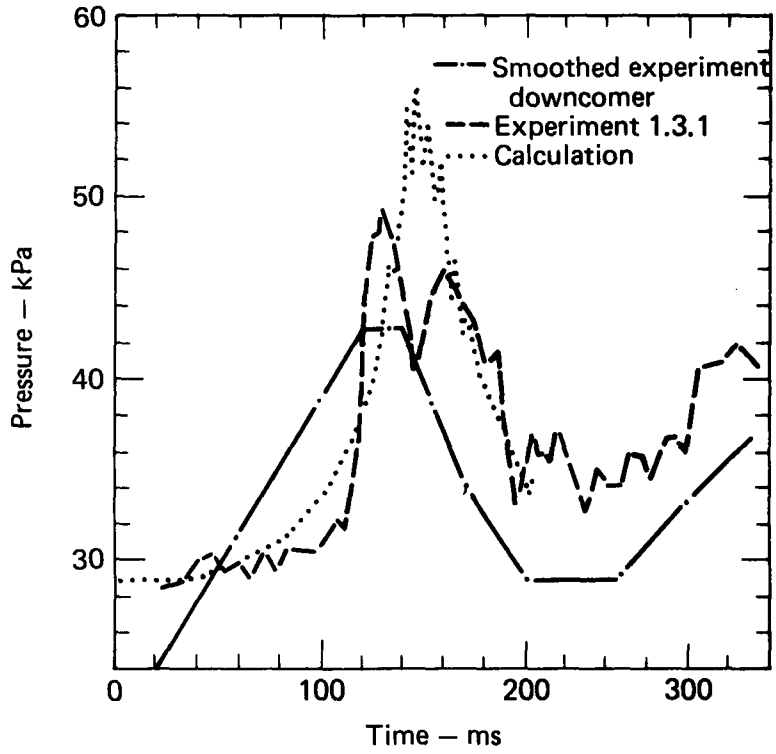


FIG. F.3. Pressure time history in downcomer pipe and at bottom center of torus. The zero time is 2.9875 s for experiment 1.3.1.

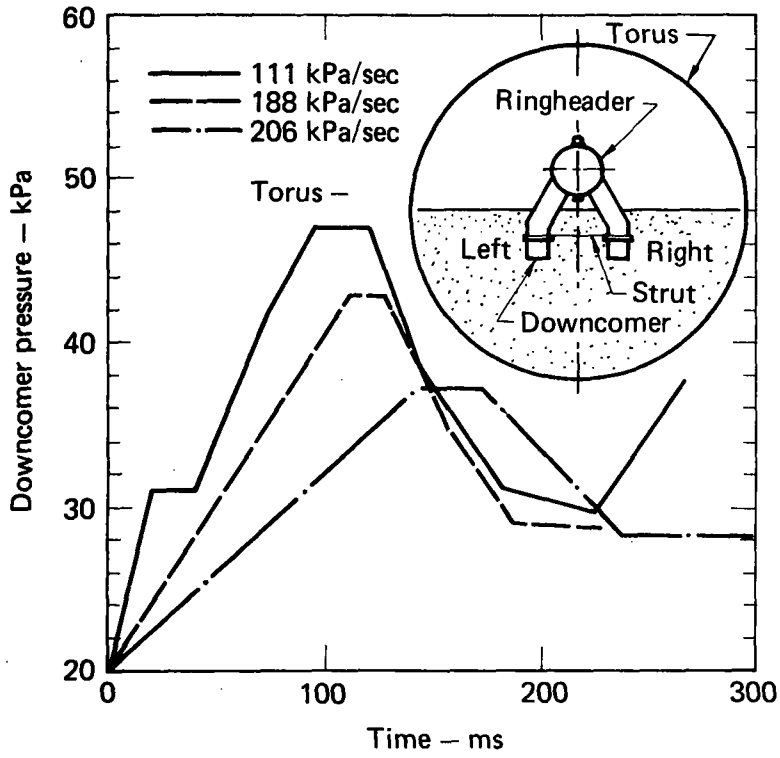


**FIG. F.4.** Smoothed downcomer pressure-time histories corresponding to various pressurization rates.

*U.S. GOVERNMENT PRINTING OFFICE : 1980 0-620-269/124

NRC FORM 335 (7-77) U.S. NUCLEAR REGULATORY COMMISSION

# BIBLIOGRAPHIC DATA SHEET

1. REPORT NUMBER *(Assigned by DDC)*
NUREG/CR-1179
UCRL-52733

4. TITLE AND SUBTITLE *(Add Volume No., if appropriate)*
Application of the Coupled Fluid-Structure Code PELE-IC to Pressure-Suppression Analysis—Annual Report to NRC for 1979

2. *(Leave blank)*

3. RECIPIENT'S ACCESSION NO.

7. AUTHOR(S)
W. H. McMaster, D. F. Quinones, C. S. Landram, D. M. Norris, E. Y. Gong, N. A. Macken, R. E. Nickell

5. DATE REPORT COMPLETED
MONTH: November | YEAR: 1979

9. PERFORMING ORGANIZATION NAME AND MAILING ADDRESS *(Include Zip Code)*
Lawrence Livermore Laboratory/NRC
P.O. Box 808
Livermore, California 94550

DATE REPORT ISSUED
MONTH | YEAR

6. *(Leave blank)*

8. *(Leave blank)*

12. SPONSORING ORGANIZATION NAME AND MAILING ADDRESS *(Include Zip Code)*
U.S. Nuclear Regulatory Commission
Division of Reactor Safety Research
Office of Nuclear Regulatory Research
Washington, D. C. 20555

10. PROJECT/TASK/WORK UNIT NO.

11. CONTRACT NO.
FIN A0116

13. TYPE OF REPORT
Technical Report

PERIOD COVERED *(Inclusive dates)*

15. SUPPLEMENTARY NOTES

14. *(Leave blank)*

16. ABSTRACT *(200 words or less)*

This report concludes a developmental effort to obtain a two-dimensional or axisymmetric computer code that calculates fluid-structure interaction problems in boiling-water-reactor (BWR) pressure-suppression systems. In this report several verification problems are concluded and applications to the Mark I and Mark II pressure-suppression systems are presented.

17. KEY WORDS AND DOCUMENT ANALYSIS

17a. DESCRIPTORS

17b. IDENTIFIERS/OPEN-ENDED TERMS

18. AVAILABILITY STATEMENT
Unlimited

19. SECURITY CLASS *(This report)*
Unclassified

21. NO. OF PAGES

20. SECURITY CLASS *(This page)*
Unclassified

22. PRICE
S

NRC FORM 335 (7-77)

UNITED STATES
NUCLEAR REGULATORY COMMISSION
WASHINGTON, D. C. 20555